Volume 2 | Issue 1 | 2020

Technical Journal

Engineering excellence around the globe

N LAVALIN

Foreword

Chris Hendy

Editor-in-Chief SNC-Lavalin
Technical Journal

Professional Head of Bridge
Engineering and Transportation
Technical Director, EDPM

Welcome to the third edition of our SNC-Lavalin Technical Journal, established to showcase the fantastic depth and breadth of our engineering expertise across a wide range of disciplines and domains and to demonstrate that technical excellence is at the heart of everything we do. This third edition highlights the impressive work we have been doing from the development of new concepts, to detailed design of new assets and the management and operation of existing assets across all of our Sectors.

In design, we have developed the world's first 15-cell caterpillar-shaped cofferdam design for the 43 m deep excavation and lateral support works required to construct a 630 m long and 33 m wide cut-and-cover tunnel and approach ramp at the southern landfall of the Tuen Mun - Chek Lap Kok Link Northern Connection Sub-Sea Tunnel Section. And we have led the way in establishing new design rules for structural steelwork, notably new simplified and more structurally efficient design rules for bridge plate girders with plan curvature which will be introduced into the next generation of Eurocode 3.

In the field of asset management, in nuclear engineering, SNC-Lavalin and the Vitreous State Laboratory of the Catholic University of America successfully conducted trials to evaluate the feasibility and implications of thermal treatment to process a variety of sludge and slurry radioactive wastes as an alternative to more traditional techniques such as grout encapsulation. And in the Highways domain, we have used complex non-linear finite element modelling to demonstrate that an existing major road bridge over the Manchester Ship Canal in the United Kingdom could withstand the likely ground movements associated with two proposed privately funded schemes and hence permit them to go ahead, contrary to the results of earlier simpler modelling.

And for operation of assets, SNC-Lavalin has demonstrated that a commercially-available collaborative robot arm can be safely deployed to handle hazardous substances, usually carried out by human operatives with some small residual risk, in sealed environments referred to as "gloveboxes."

The above examples provide only a small insight into the wealth of innovative papers presented in this journal and the far wider contribution that SNC-Lavalin makes day to day.

I hope you enjoy the selection of technical papers included in this edition as much as we have enjoyed compiling them.

Editor-in-Chief

Chris Hendy
Editor-in-Chief

FREng, MA (Cantab) CEng FICE Eur Ing
Technical Director, Atkins Fellow,
Professional Head of Bridge
Engineering
Engineering, Design and Project
Management
Epsom, UK

2020 Editorial Board Members

Ramy Azar
Ph.D, Ing.

Vice-President of Engineering and CTO
- Grid Solutions & Renewables
Power, Grid and Industrial Solutions
Infrastructure
Montreal, Canada

Vinod Batta
Ph.D., P.Eng.

Vice President & General Manager,
Power Solutions - Western Canada
Power, Grid & Industrial Solutions
Infrastructure
Vancouver, Canada

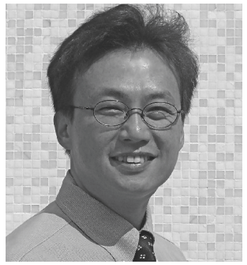

Eric Chui Hon Man
BEng CEng ACGI MHKIE MIMM MICE
MIStructE RPE(GEL, CVL, STL)

Divisional Director
Tunnel and Ground Engineering, EDPM
Hong Kong, China

Chad Gvozdenovic
P. Eng.

Vice President, Global Technical Lead
Oil & Gas
Calgary, Canada

Donna Huey
GISP

Atkins Fellow and Sr. Vice President,
Client Technology Director
Engineering, Design and Project
Management
Orlando, FL, USA

Matt Keys
PhD BEng CEng

Fellow, Technical Director, Global
Technical Authority – Offshore
Structures
Oil & Gas
Perth, Australia

Adrian Lindon
BA(Hons) Dip. Arch, ARB, RIBA

Senior Technical Director - Atkins
Fellow, Design and Engineering
(Middle East and Africa)
Engineering, Design and Project
Management
Dubai, UAE

Navil Shetty
PhD, DIC, FIAM

Atkins Fellow and Technical Chair for
Asset Management
Centre of Excellence for Digital Asset
Management & Operations
Bangalore, India

Patrick Sikka
P. Eng

Vice-President
Mining & Metallurgy – North America
Toronto, Canada

Richard Moura
P.Eng.

Director, Business Development Rail
& Transit
Global Business Development,
Transportation-Major Projects
Infrastructure
Toronto, Canada

Tim Milner
CSci CChem MRSC

Atkins Fellow and Chief Technology
Officer
Nuclear
Columbia, SC, USA

Samuel Fradd

Technology Manager
Engineering, Design and Project
Management
Epsom, UK

Akshaye Sikand
MS, P.Eng.

Manager, Knowledge Management
Project Oversight
Toronto, Canada

Production Team

Dorothy Gartner
MLIS

Librarian
Project Oversight
Montreal, Canada

Samantha Morley
CAPM

Operations Coordinator
Technical Professional Organization,
Atkins North America
Denver, CO, USA

Cheryl Law
MEng CEng MICE

Associate Engineer, Infrastructure
Engineering, Design and Project
Management
Epsom, UK

Graphic Design Team

Montreal, Canada

About the Cover

The cover photograph depicts the Muskrat Falls Hydroelectric Project (paper #07), looking upstream on the lower Churchill River with the reservoir at full supply level (EL 39 m). Centre of photo is the powerhouse, with the spillway and north dam to the right of it and south dam to the left. The photo was taken in the fall of 2019 by article author Greg Snyder.

Volume 2 | Issue 1 | 2020

Assessment of Barton High Level Bridge Approach Span Superstructures

David M. Day

Chief Engineer
Engineering, Design and Project Management
Warrington, UK

Abstract

Barton High Level Bridge (BHLB), one of the longest in the UK, carries the M60 motorway over the Manchester Ship Canal. Situated on the Manchester Outer Ring Road, it is of strategic importance in maintaining the smooth functioning of the North West of England's highway network. In 2013, proposals for two privately funded schemes in the vicinity of the bridge warranted a structural assessment of BHLB to demonstrate that any ground movement associated with the proposed construction would not affect its safe operation. As would be expected with a structure of this age, 1st stage assessment revealed that some elements did not meet current assessment standards and further, more complex analysis was adopted. This paper describes the approach to improve the assessment result in one key area - the half joint end frames to the approach spans. The additional analysis showed the bridge to be satisfactory when compared to its design criteria, not only in the steady state but also to allow construction of the two adjacent privately funded schemes.

Keywords

Bridges; Assessment; Approach Spans; End Frames

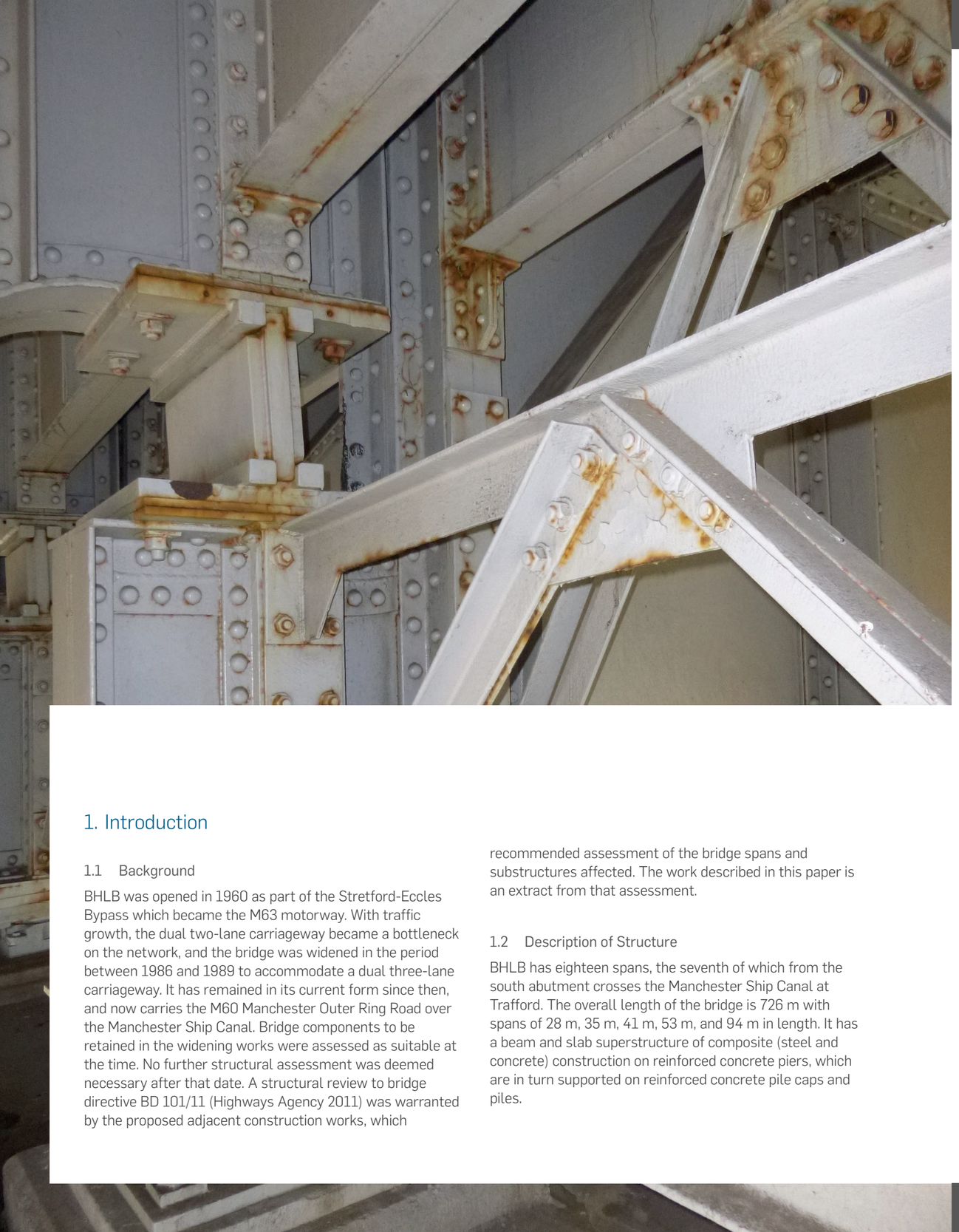

1. Introduction

1.1 Background

BHLB was opened in 1960 as part of the Stretford-Eccles Bypass which became the M63 motorway. With traffic growth, the dual two-lane carriageway became a bottleneck on the network, and the bridge was widened in the period between 1986 and 1989 to accommodate a dual three-lane carriageway. It has remained in its current form since then, and now carries the M60 Manchester Outer Ring Road over the Manchester Ship Canal. Bridge components to be retained in the widening works were assessed as suitable at the time. No further structural assessment was deemed necessary after that date. A structural review to bridge directive BD 101/11 (Highways Agency 2011) was warranted by the proposed adjacent construction works, which recommended assessment of the bridge spans and substructures affected. The work described in this paper is an extract from that assessment.

1.2 Description of Structure

BHLB has eighteen spans, the seventh of which from the south abutment crosses the Manchester Ship Canal at Trafford. The overall length of the bridge is 726 m with spans of 28 m, 35 m, 41 m, 53 m, and 94 m in length. It has a beam and slab superstructure of composite (steel and concrete) construction on reinforced concrete piers, which are in turn supported on reinforced concrete pile caps and piles.

Figure 1. Barton High Level Bridge looking north, viewed from the south bank of the Manchester Ship Canal

Prior to widening, the deck had eight longitudinal steel plate girder beams; four to each deck half, approximately 2.8 m in depth increasing to 5.5 m at the haunches in the canal and anchor spans. The original girders are of riveted plate construction and were retained in the widening works. The reinforced concrete deck slab had a longitudinal joint within the central reserve, which ensured that each half of the superstructure acted independently from the other (four beams per deck half). Each beam was simply supported with half jointed ends at the pier positions; the only exception being the main (canal) span, a suspended structure, half-jointed with the haunched cantilever girders. In turn, the canal span cantilevers were continuous with the adjacent anchor spans over the main “canal” piers. All spans had continuous transverse bracing at the ends and at regular centres in between, albeit all bracing runs were broken beneath the central reserve thus maintaining the separation of the two deck halves.

The intermediate piers are reinforced concrete hollow crossheads supported on twin hollow columns, originally providing access to the bearing shelf. The original pile caps are largely supported on 14” vertical and raked square precast concrete piles, driven to a depth of between 5.2 m and 11.9 m below the underside of the foundations, and understood to be toed into fluvio-glacial sands and gravels.

The 1989 widening works added a new line of girders on each side of the existing bridge, allowing an increased width of deck slab which was replaced in its entirety. The new steel plate girders were of welded construction. Additional bracing was provided on all existing transverse bracing lines between the widening and original edge beam (now first internal beam). Bracing was of the same form as the original, but with structural elements and connections commensurate with the period of construction. Some modifications (local strengthening) were carried out to the existing bracing and half end bearing stiffeners during the widening works.

Widening of the substructure proved to be more complicated. In 1985, concrete testing was undertaken to the original piers. Areas of map-cracking were discovered indicating the possibility of alkali aggregate reaction (AAR) and so cores were extracted from affected areas. Accelerated expansion tests, and petrographic and chemical analysis, confirmed that the concrete was slightly reactive, raising concerns that expansion of the original pier concrete could occur in the future.

By the time testing works were complete, the pier widenings had already been designed to act monolithically with the original piers. However, the potential for future expansion of the original concrete relative to the new concrete, raised concerns of an indeterminate redistribution of load between substructures, and so the original proposals were abandoned. The pier widenings were redesigned as independent structures, building in the potential for vertical

differential movement (VDM) between the bearings on the original piers and those on the new. It was thus accepted that monitoring of bearing levels would have to be carried out over the long term, and bearings may need to be adjusted to ensure that the deck structure would not become overstressed in the future. The widened piers were designed as hollow, free-standing columns on independent piled foundations. The design provided a connection between new and original piers at bearing shelf level by a link and pin assembly (referred to as the "Pin Bearing") permitting vertical, but not longitudinal or transverse movement. The final deck and pier arrangement is shown in Figure 2.

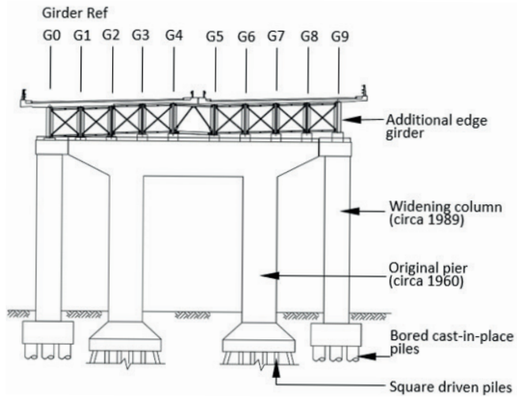

Figure 2. Section through BHLB approach spans showing the original piers and additional widening columns

1.3 Monitoring

The Bridge Maintenance Manual (BMM) requires monitoring of bearing levels to be at intervals of not greater than two years. The BMM states that re-levelling the bearings must be done before the vertical differential movement between inner and outer piers exceeds 3 mm. Monitoring was undertaken at each pier by measurement of the distance between permanent "DEMEC" points and applying basic trigonometry to determine the vertical and horizontal movements. Refer to Figure 3.

Negative (-ve) and positive (+ve) movement indicated growth and settlement respectively of the old pier relative to the new. It became apparent over time that the differential movements were:

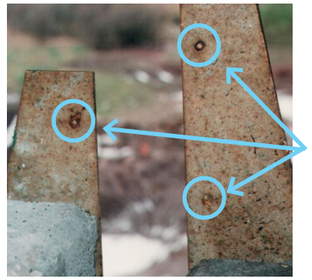

Equilateral triangle of DEMEC measuring points to measure VDM

Figure 3. Typical DEMEC monitoring points at joints between the original piers and pier widenings

- Subject to a settling down period in the first years after construction (Figure 4).
- Cyclical in nature on an annual basis (Figure 5).
- Temperature related; daily and seasonal.
- Following mainly a +ve trend contrary to the design movements anticipated due to AAR, albeit one pier (Pier M East) proved to have a propensity for long term differential movement in the -ve direction.

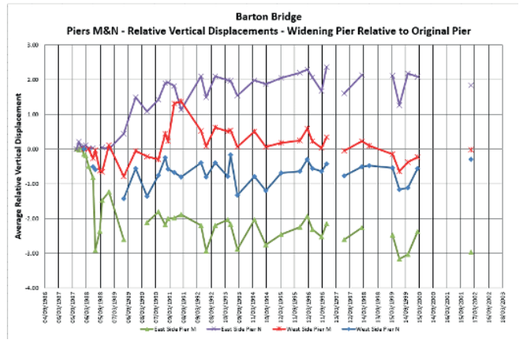

Figure 4. Piers M & N – VDMs between 1988 to 2002

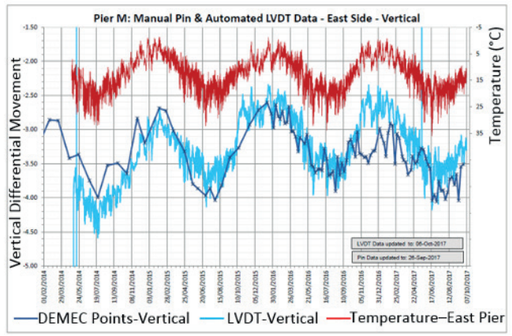

Figure 5. Pier M – Cyclical VDMs 2014 to 2016

1.4 Previous Attempts to Re-Level the Bearings

An attempt was undertaken to re-level the G0 bearing to the east side of Pier F in 1994. The re-levelling attempt took numerous visits and was ultimately unsuccessful:

Visit 1: During jacking, separation was observed at the sliding surface with paint securing the top bearing plate.

Visit 2: Solvents were applied to release the paint at the top bearing plate – the bearing still refused to separate during jacking.

Visit 3: Action was taken to strap the top bearing plate to the lower bearing plate - bolts sheared during jacking.

Visit 4: Additional securing bolts were added to the strap. Separation was finally achieved at top bearing plate but "spring" was noted in the bottom bearing plate offsetting the beam lift. Insufficient space was generated to allow insertion of shims.

Visit 5: Jacking to the adjacent girder (G1) to allow greater lift on edge girder (G0). Still insufficient space to allow insertion of shims. The re-levelling attempt was abandoned.

Given the problems experienced above and that the structure was showing no signs of distress, no further attempts were made to re-level any of the bearings until 2017.

2. Assessment

2.1 Methodology for the Assessment of BHLB Approach Spans

Assessment was carried out in accordance with standards BD 61/10, BD 56/10 and BD 44/95 (Highways Agency 2010, 2010 and 1995). The approach span structures were initially modelled using simple methods; grillage analysis for the deck structure and plane frames for the end restraints. [Circuitous modelling and repetitive analysis of the intermediate bracing led to a change in approach for the canal spans, for which the entire three span structure (canal and anchor spans) was modelled using 3D Finite Element methods]. Each element was assessed initially for dead and live load only to evaluate the basic usage. Subsequently, the allowable VDM between the original and widening substructures was determined. Allowable movements were compared with the actual movements at the corners bounding each span. Elements assessed as inadequate for the movements recorded through monitoring were highlighted and recommendations were made for improving the results.

2.2 Modelling of the Superstructure to the Approach Spans

The approach span structure was modelled using line beams or grillage (Figure 6) depending on the stage of construction. Properties of the continuous transverse bracing were determined using the single bay bracing frame shown below (Figure 7).

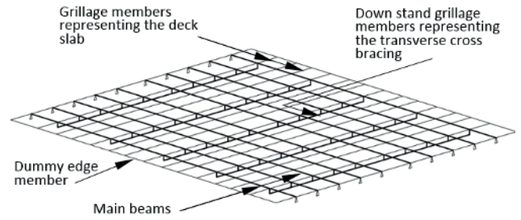

Figure 6. Grillage model – approach spans

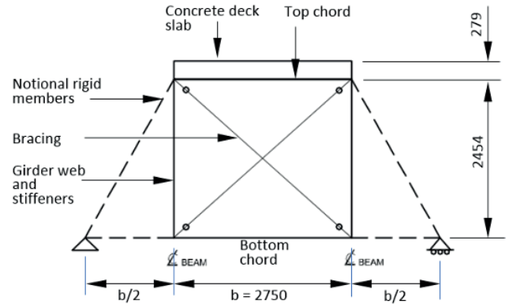

Figure 7. Single bay bracing frame – approach spans

The end frames were modelled separately as plane frames using stick elements as shown in Figure 8. The numerous end-plated connections between bracing and main beam bearing stiffeners were modelled as rigid.

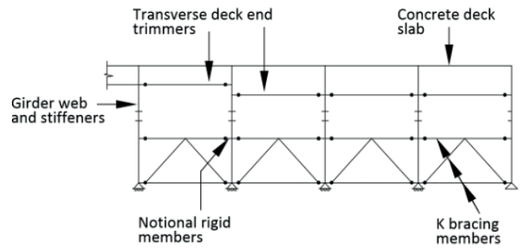

Figure 8. Half joint end bracing modelled as a plane frame stick model

2.3 General Approach to the Reporting of Assessment Results

Assessment results would normally be presented in terms of a Usage Factor (UF) or Adequacy Factor (AF), where AF = 1/UF. Reporting was made complicated because of the need to determine the allowable VDM for each calculation undertaken, which was dependent on:

- The contribution to "usage" from each of the movements at the four corners bounding a span.
- The historical maxima (+ve or -ve) of VDM at each of the four corners of a span bounding a particular structural detail to be checked.

For each in-span detail, the assessment determined the effect of 1 mm of VDM at each of the four corners bounding the span containing the detail. The four values were added to give the total effect for 1 mm of VDM. For members within the end-frames, the effect from 1 mm of VDM was determined from the movement at one corner only. The results were recorded typically as shown in Figure 9.

The allowable VDM could then be compared with any single movement value recorded through monitoring to give an initial conservative indication of the location of critical elements.

2.4 Results for the Assessment of the Approach Span Superstructures

The majority of elements within the superstructure passed the assessment with sufficient reserve to accommodate the historical maxima of VDM recorded through monitoring. Critical elements were found in the intermediate transverse cross bracing and the end plate connections in the deck end frames.

2.4.1 Intermediate Transverse Cross Bracing

Initial modelling of the bridge spans made use of all bracing members (no member limits). This analysis showed numerous bracing members theoretically failing under 40t Assessment Live Loading (ALL), particularly in buckling of the very slender compression diagonals between girders G2 & G4 and G5 & G7.

Re-analysis (with member limits) removing the diagonal members that were previously theoretically failing, assuming them to have buckled and able to carry tension only, demonstrated that there were still a small number of theoretical failures under 40t ALL. In the 35 m approach spans, the diagonal tension members in bracing bays toward the centre of the deck were 1% overstressed for dead + live loading with 1% additional usage per mm of VDM, resulting in a maximum usage factor of 1.07. This equates to 26t ALL for dead and live load only and 18t ALL including the current maxima of seasonal differential movement.

Hendy, Man, Mitchell and Takano (2018) examined the reduction of design partial factors for a defined reliability level over a given reference period. The paper recommends that a reduction to the overall assessment usage factor of 0.91 can be applied where remedial works would represent a medium cost of safety measure. This was deemed appropriate for the 35 m and 41 m approach spans of BHLB and Highways England approved a Departure from Standard to apply the 0.91 reduction factor. This reduced the maximum usage factor above to 0.98.

2.4.2 Deck End Frames

The end frame stick models proved to be stiff, ideal for resisting the transverse effects of wind loading and destabilizing forces. When the maxima of seasonal VDM were introduced, the majority of structural members were satisfactory but UFs in the end plated connections were generally significantly greater than 1.0 (up to 3.8). Yielding of the thin angle components of the original bearing stiffeners, which act as end plates to the deck end trimmers and K bracing, was calculated. It was thought that the real structure movements were being accommodated due to the inherent flexibility of the end-plate T-stub connections. Allowance for this flexibility would require a significantly more complex model. Improvements to the end frames were made through the re-modelling discussed in 3.1.

Assessment Results for Transverse Bracing Elements - 41 M Spans - 40 T All No Limits

Girder	Loading	Element		Effect	Location	Units	Strength at ULS	Load Effect Dead + Live	UF	1mm Diff ± 'x' kN (Nominal)	Allowable Additional Diff Movement (mm)	
											Nominal	ULS γ_{FL} = 1.2
G4-G5	40T ALL (no limits)	Top Chord –	Back to Back Angles	Compression	Bay 22	kN	424	352.2	0.83	12.6	+ve 5.8 -ve 5.8	+ve 4.8 -ve 4.8

Figure 9. Methodology for reporting calculated allowable differential vertical movement

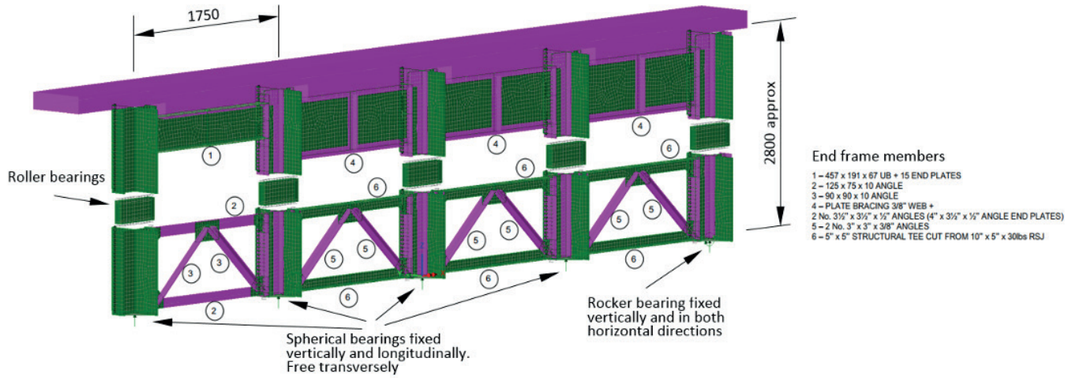

Figure 10. Stage 1 end frame finite element model

3. Improvement of Assessment Results

3.1 Re-Modelling the Approach Span End Frames – Re-Model Stage 1

Re-analysis of the end bracing at the half joints was undertaken by a static finite element (FE) method using LUSAS software.

Thick, quadrilateral, shell elements (LUSAS element type QTS4) were used to model main girder webs, upper bracing girder webs, transverse plates in bearing stiffeners, gussets, and original bracing chords. The concrete deck, lower bracing diagonals, bearing stiffener outstands, some end plates and angles connecting the bearing stiffener outstands to the main girder webs were modelled as thick, three-dimensional beam elements (LUSAS element types BMS3 and BTS3); refer to Figure 10. The deck slab was considered to be cracked over the width of the top flanges of girder G1, as pre-analysis revealed tensile stresses greater than 5 MPa, sufficient to cause cracking in the concrete. This decreased the slab stiffness and reduced the effects due to VDM in the components of the end frame and bearings.

Springs were used to connect the bracing to the main girders at a series of discrete nodes on both sides of the joint. These nodes were assigned a three dimensional "joints for beams" element (LUSAS element type JSH4). The spring stiffness was selected to allow separation of plates in tension (with a stiffness calculated as described below), but to prevent any relative movement in compression. The roller plates of the upper bearings at the half joints were modelled with the same shell elements (LUSAS element type QTS4). However, to allow free rotation at both bearing ends, a model joint (LUSAS element type JSH4) was introduced at these locations to fix the translations only. The final model is shown in Figure 10.

3.2 Linear Elastic Tensile Stiffness of the End-Plate Connections

According to BS EN 1993-1-8 (BSI 2010), the stiffness of the connections should be determined from the flexibilities of its basic components, each represented by an elastic coefficient (k_i).

Thereafter, the combined effect may be obtained with sufficient accuracy from:

$$K = \frac{1}{\sum\left(\frac{1}{k_i}\right)} \qquad (1)$$

Table 6.11 of BS EN 1993-1-8 defines the coefficients k_i, which should take into account the following effects:

- The column flange in bending (k_4);
- The end-plate in bending (k_5); and
- The bolts in tension (k_{10}).

In order to validate the use of the method above, local FE models were produced for most tensile joints. Some simplifying assumptions were made but special effort was put into modelling the correct geometry and the complex relationship between the bending stiffness of the flanges and the axial stiffness of the bolts. In doing this, the prying forces were also considered by providing joints between the outer edges of the respective plates where there is contact. The output of this work and its comparison against the code method is shown in Figure 11.

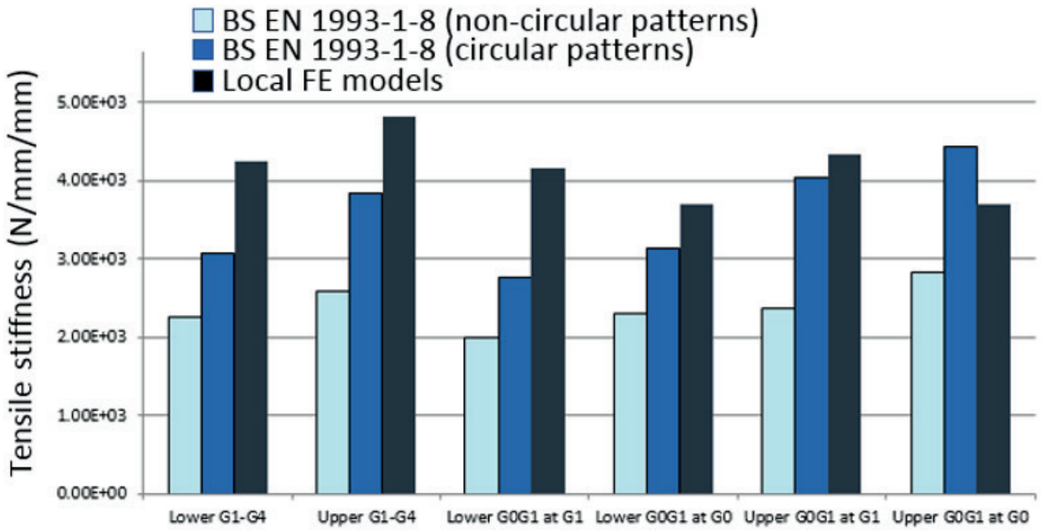

Figure 11. Tensile stiffness of the end plate (T-stub) connections

Comparing the results of the local FE models with the formulas set by BS EN 1993-1-8, it was seen that the behaviour of the models is close to the Eurocode predictions but are generally stiffer, which may suggest that some conservative assumptions have been made.

3.3 Non-Linearity of the End Plate Connection

The response of all the connections analysed is inherently non-linear. In compression, the contact between members prevents any significant deformation. In tension, the joints start to pry apart as soon as the load is applied. To take this into account, the response of the joints was modelled as shown in Figure 12.

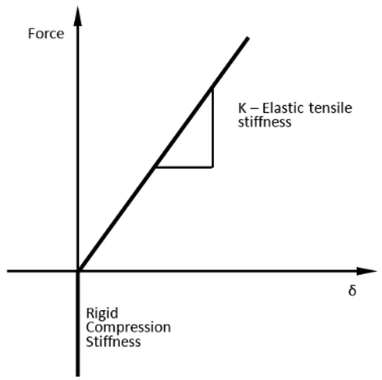

Figure 12. Model of the spring stiffness of end plate connections (2 Phase)

3.4 Influence of Bolt Preload on Stiffness of the End Plate (T-Stub) Connections

The preload effect on stiffness is not used in the BS EN 1993-1-8 methodology which can be applied to both preloaded and non-preloaded joints. However, the notion that the preload must be overcome to separate the plates suggests that the level of preload introduced may have an important influence on the results. To address this concern, a single, localised FE model was produced to evaluate this effect alone (Figure 13) and the results extrapolated to all connections. To quantify the preload effect, the relationship between the stiffness of a preloaded and non-preloaded connection was plotted against the quotient between the load and the preload. The result is shown in Figure 14.

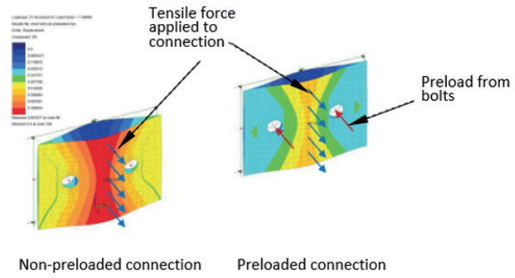

Figure 13. FE model of a general bolt row

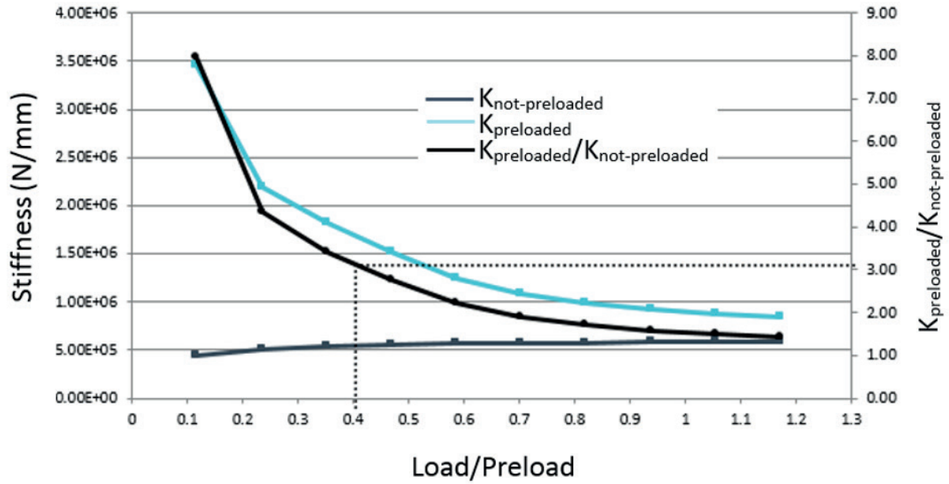

Figure 14. Influence of preload on connection stiffness

For simplicity, the function above, which accounts for the preload effect, was converted into a single factor. Typically, in the end frame analyses the value of load/preload was found to be around 0.4. Therefore, using 0.4 as a typical value, it was concluded that the preload increased the stiffness of the joints by a factor of approximately 3.

3.5 Increased Flexibility of the End Plate Connections Approaching Plasticity

Once yield has been reached, but before reaching its ultimate capacity, the joint passes through different plastic stages reducing the overall stiffness as the load increases, e.g. the formation of the first plastic hinge on opposite plates of the same joint. To allow for this, BS EN 1993-1-8 prescribes a reduction factor (μ) that can be determined as follows:

$$\mu = \left(\frac{1.5 M_{i,Ed}}{M_{i,Rd}} \right)^{2.7} \qquad (2)$$

The factor tends to 3 as the design bending moment ($M_{j,Ed}$) tends toward the bending resistance ($M_{j,Rd}$).

The final value for elastic tensile stiffness of each joint was determined from the stiffness coefficients calculated in accordance with BS EN 1993-1-8 (for non-circular patterns), modified by the relevant preload factor (Figure 14) and further modified by the μ factor (Equation 2) as appropriate.

3.6 Assessment Results Allowing for the Springs in the End Plate Connections

An initial elastic analysis of the end frame (Figure 10) taking into consideration the joint stiffness model described above, showed that a number of connections still exceeded their theoretical capacity (calculated to BD 56/10 methodology) when subject to the maximum recorded seasonal VDMs. The analysis was further refined as described in 3.7 below.

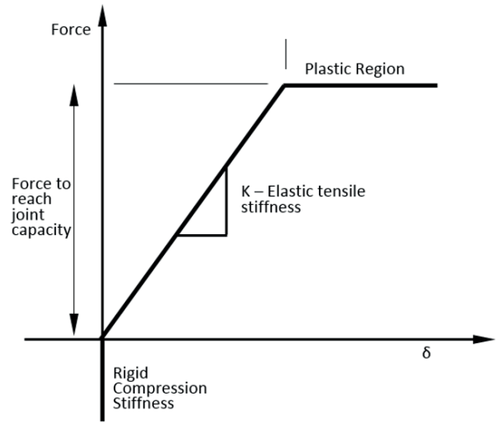

Figure 15. Model of the spring stiffness of end plate connections including plasticity (3 Phase)

3.7 Introduction of Plasticity into the End Plate Joint Spring Model – Re-Model Stage 2

Once the joint capacity is exceeded, the connection enters into a plastic mode of behaviour with plastic hinges forming in the end plates of the T-stub allowing further deformation with no increase of load. Therefore, the plastic strength limit of all connections was directly introduced in the FE model by amending the joint spring properties as shown in the load/deflection curve in Figure 15. In doing so, the capacity of the bracing bays is automatically fulfilled provided that the model converges, the bracing members themselves do not become overstressed, and all connections have enough ductility to redistribute the forces to other less used elements.

Since a plastic limit was imposed on all tensile connections, the usage factor was limited to 1.00 and the failure criterion had to be expressed in terms of limiting plastic strain, which was conservatively assumed as 10%. As there was no model output to compare with this value, the assessment check was made in terms of deformation capacity (not discussed further here).

The flexibility of the end plates increased the VDM that could be tolerated and changed the overall theoretical failure mechanism away from the connections and to the other components in the frame. The only end plate connections where full plasticity could not be achieved were those to the steel deck end trimmer in the G0/G1 bay. The trimmer beam is a 457x191x67 UB with a connection detail shown in Figure 16. In these connections, the end plate local to the second and fourth bolt row is stiffened by both the web and the flange of the deck end trimmer and will not yield before the bolt fails in tension. Ultimately, the overall capacity of the end frame was limited by buckling of the top brace in the lower K bracing frame (-4.8mm VDM) and potential bolt failure at the end trimmer G0 connection (+6.0mmVDM). The deformed shape of the end frame under -ve VDM is shown in Figure 17.

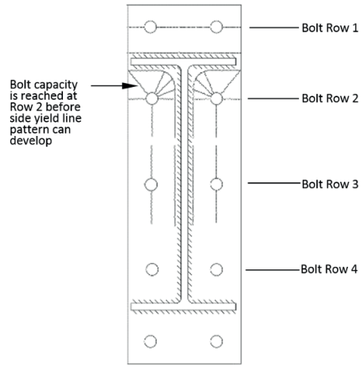

Figure 16. Deck end trimmer connection with the G0 bearing stiffener

4. Conclusions

Barton High Level Bridge is a major structure that has strategic importance for the safe and continual operation of the motorway network in the North West of England. From the assessment work undertaken to the approach span end frames, the following can be concluded:

- Re-modelling of the deck end frames using FE methods provided a more realistic approach for assessing the effects of substructure differential movements.
- Considerably more time and cost was expended to build, test and verify the FE model than the simple stick model, justifiable in this case due to the improvement in the assessment result.
- Allowing for the preload in the connections with thin end plates, the connection stiffness was increased by a factor of approximately 3. However, the increase in stiffness made little difference to the assessment result when compared with a similar analysis with no allowance for preload, due to the plasticity in the connections between girders G0 and G1.
- Allowing for the flexibility of the end plate connections, the assessment result was improved from virtually zero allowable VDM (original stick model) to values of -4.8 mm and +6.0 mm, exceeding the design maximum allowable (-3.0 mm).
- The improvement in the results of the original assessment allowed Highways England to give permission for the two private schemes to proceed.
- Moving forward over the future life of the bridge, the assessment result has provided Highways England with greater flexibility and time to manage re-levelling of the bearings, as and when required by on-going monitoring.

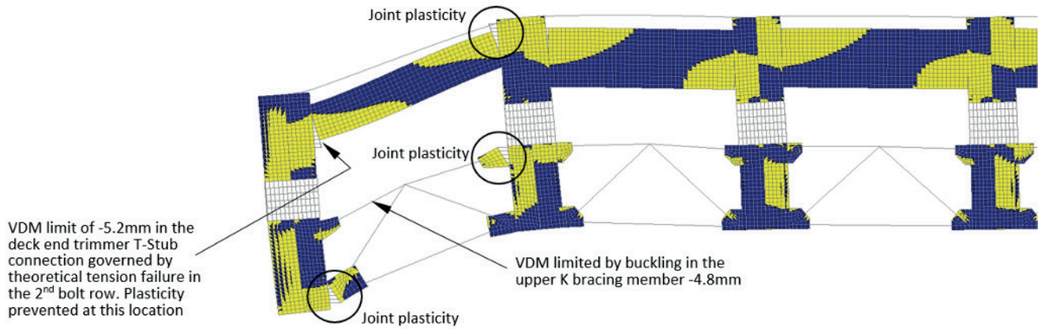

Figure 17. Deformed shape of end frame for -ve VDM

Acknowledgements

Originally published as Day DM. Assessment of Barton High Level Bridge approach span superstructures. In: Caspeele R, Taerwe L, Frangopol DM. Life Cycle Analysis and Assessment in Civil Engineering: Towards an Integrated Vision. Proceedings of the Sixth International Symposium on Life-Cycle Civil Engineering (IALCCE 2018), 28-31 October 2018, Ghent, Belgium. London: CRC Press; 2018. p. 2889-2896. Reprinted with permission © Taylor & Francis. Ltd

References

BSI 2010. BS EN 1993-1-8:2005 Eurocode 3: Design of Steel Structures – Part 1-8: Design of Joints. London: British Standards Institution.

HA 2008. BD 44/95 The Assessment of Concrete Highway Bridges and Structures. London: Highways Agency.

HA 2010. BD 56/10 The Assessment of Steel Highway Bridges and Structures. London: Highways Agency.

HA 2010. BD 61/10 The Assessment of Composite Highway Bridges and Structures. London: Highways Agency.

HA 2011. BD 101/11 Structural Review and Assessment of Highway Structures. London: Highways Agency.

Hendy CR, Man LS, Mitchell RP, Takano H. 2018. Reduced Partial Factors in UK Assessment Standards for Assessment of Bridges and Structures. Proceedings of the Institution of Civil Engineers – Bridge Engineering Volume 171 Issue BE1: 3-12.

New Design Rules for Plate Girders Curved in Plan

Chris R Hendy

FREng MA(Cantab) CEng FICE Eur Ing
Technical Director, Atkins
Fellow, Head of Bridge Engineering
Engineering, Design, and Project Management
Epsom, UK

Minjie Cai

PhD BEng MIStructE
Principal Engineer
Engineering, Design, and Project Management
Glasgow, UK

João Pedro Martins

ISISE, Civil Engineering Department, Universidade de Coimbra
Portugal

Filip Ljubinković

ISISE, Civil Engineering Department, Universidade de Coimbra
Portugal

Abstract

Many steel plate girder bridges today are curved in plan. This is because it is now relatively inexpensive to construct bridges with continuous plan curvature, which is more aesthetic than the traditional series of straight spans kinked at supports, and because many bridges are now built in congested urban areas where complex curved plan alignments are required to thread new infrastructure past existing. However, design rules have not caught up with this fabrication trend. The design of continuously curved steel plate girder bridges is typically more complex than that for equivalent straight ones. The plan curvature both induces additional stresses in the webs and flanges, reducing overall bending strength, and changes the shear behaviour and resistance of the webs.

This paper considers typical steel concrete composite multi-girder decks with plan curvature, and uses the results of an extensive finite element parametric study to propose new design rules based on modifications to the existing Eurocode rules for straight girders, so there is a consistent approach provided for the design of plated girders for all curvatures, including none.

Keywords

Curved in Plan; Steel Plate Girder; Bending Capacity; Shear Capacity; Shear-Moment Interaction

1. Introduction

Many steel plate girder bridges today are curved in plan. This is because it is now relatively inexpensive to construct bridges with continuous plan curvature and because many bridges are now built in congested urban areas where complex curved plan alignments are required to thread new infrastructure past existing. The use of near true plan curvature is also more aesthetic than a series of straight spans kinked at supports, which were favoured for practical reasons in the past.

But the design of continuously curved steel plate girder bridges is typically more complex than that for equivalent straight ones and codified design rules have not caught up with this fabrication trend. The plan curvature both induces additional stresses in the webs and flanges, reducing overall bending strength, and changes the shear behaviour and resistance of the webs. Bracing provides transverse restraints to the bottom flanges and is generally spaced at closer centres for a curved in plan bridge than for an equivalent straight bridge to ensure that warping stresses in the flanges are minimised.

The current Eurocodes do not address plate girders with plan curvature, whilst ASSHTO does so in a simplified and empirical way, placing limitations on the spacing of bracing. The free design of bridges curved in plan therefore currently requires designers to establish their own approaches beyond the codified rules for straight girders, and this has typically both introduced a lack of consistency in design and also some conservatism, potentially wasting material and increasing carbon footprint. Carrying out a geometrically and materially non-linear analysis is a potential option for computing an efficient structural solution, but it is impractical in most design scenarios because of the time and cost of the analysis.

It may be observed that an alternative and more structurally efficient solution for curved bridges is to use box girders, which are better equipped to take the torsional effects induced by the curvature and are themselves inherently stable against lateral torsional buckling. However, the cost per tonne of fabricating a box girder is considerably higher than the equivalent cost per tonne of a plate girder so is not always the inevitable choice of structural form, particularly at modest plan curvatures.

This paper considers typical steel concrete composite multi-girder decks with plan curvature, such as that in Figure 1, and uses the results of an extensive finite element parametric study to propose new design rules based on modifications to the existing Eurocode rules for straight girders so there is a consistent approach provided for the design of plated girders for all curvatures, including straight girders with zero curvature. The work was funded through the European Research Fund for Coal and Steel (RFCS) project "Outburst."

Figure 1: Typical curved in plan multi-girder bridge

2. Effects of Curvature in Plan and Treatment in Design

Straight plate girders are typically verified by checking the adequacy under moment, M_{Ed}, and shear, V_{Ed}, and the interaction between these. A typical interaction curve, representing the requirements of EN 1993-1-5:2006, is shown in Figure 2. But the resistance to moment, M_{Rd}, and shear, V_{Rd}, for girders curved in plan are affected by the curvature and a torque T_{Ed} is also introduced. A simple beam model does not itself give information on how the torque is carried within the cross-section and this tends to encourage modelling and design approaches that use stresses rather than stress-resultants. Whilst this is valid, it creates a discontinuity with the codified rules for straight girders, which use stress-resultants and the economy of which has benefitted from extensive physical and parametric testing over the years (Hendy CR and Murphy CJ (2007)). Methods based on stress checks are typically based on elastic stress analysis and elastic stress limits and are inherently conservative.

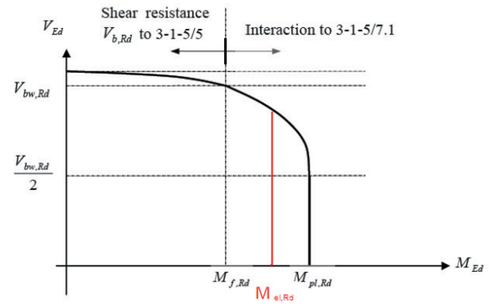

Figure 2: Typical interaction curve between moment and shear for straight girders according to EN 1993-1-5

Plan curvature in plate girders creates some additional effects that must be evaluated and the provision of additional torsional bracing between main beams, together with additional web stiffeners, is likely to be necessary to limit the adverse effects and produce an efficient design. There is, however, a balance to be held between the provision of additional bracing and stiffeners to minimise flange and web dimensions, and simply increasing the web and flange sizes to accommodate the additional effects as both will increase the tonnage but additional bracings and stiffeners may increase fabrication complexity and the cost per tonne of steel for these elements.

The plan curvature leads to the development of the following stresses in the webs and flanges as shown in Figure 3.

Flanges

- Axial stress σ_{Ed} from the major axis bending moment in the main beam
- Shear stress $t_{f,Ed}$ arising from the main beam vertical shear force
- Warping stress $\sigma_{w,Ed}$ arising from the transverse bending moment in the flange produced by the plan

curvature and the resulting torsional moment on the main beam

- Shear stress $\tau_{w,Ed}$ arising from the warping force in the flange caused by the plan curvature
- Saint Venant torsional shear stress $\tau_{ft,Ed}$ resulting from the torsional moment acting on the main beam

Web

- Shear stress τ_{Ed} arising from the main beam vertical shear force
- Saint Venant torsional shear stress $\tau_{t,Ed}$ resulting from the torsional moment acting on the main beam (which are usually small in magnitude)
- Transverse bending stresses associated with cross section distortion as the flanges warp (not shown)

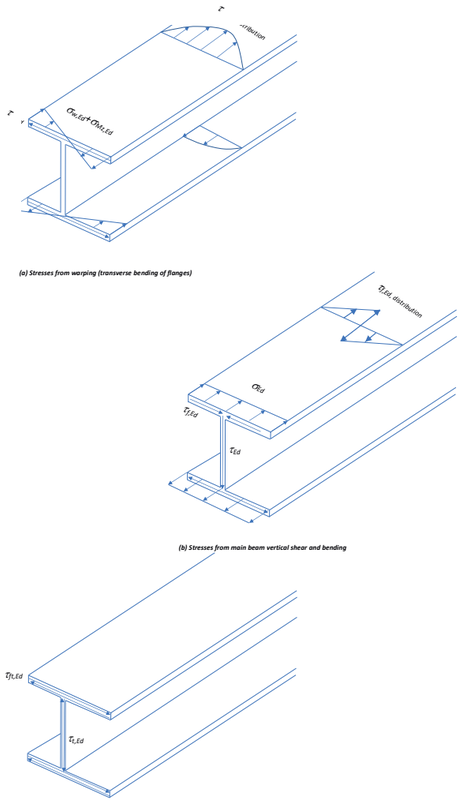

Figure 3: Stresses arising in plate girders curved in plan

The above stresses can be obtained directly from a global finite element analysis, albeit combined rather than separated into the above component, and can be used to carry out checks of the main girders. However suitable amplifications to the stresses need to be made to allow for buckling deformations, either by hand or through a geometrically and materially non-linear analysis. The use of stresses directly in design is not considered further. Instead, simpler design rules are proposed which eliminate a discontinuity with the rules for straight plate girders which are more economic by allowing for the plastic redistribution that occurs at the ultimate limit state.

3. Parametric Study Methodology

3.1 Modelling Geometry and Material Properties

In order to better understand the ultimate behaviour of plate girders with curvature in plan, a series of finite element models were set up using the software package LUSAS. The basic model shown in Figure 4 is a simply supported beam of span 30 m with regularly-spaced transverse stiffeners creating twelve panels each of length equal to 2.5 m. Lateral and torsional restraints can be attached to the transverse stiffeners. The lateral buckling behaviour of the flange was investigated by varying the spacing of the restraints, which was always a multiple of the stiffener spacing and set to 2.5 m, 5 m or 7.5 m. The restraints are all rigid in accordance with the requirements for rigid restraints in EN 1993-2. The radius of the beam in plan was varied as show in Figure 5, but the developed length of the span was always maintained at 30 m. The steel beam had a height of 1.5m in the majority of cases, giving a span to depth ratio of 20, but other cases were considered with span to depth ratio up to 30. A range of cross-section properties were considered such that different section classifications in accordance with EN 1993-1-1: 2005 were obtained, but most cross-sections were generally within Class 3 and 4. The beam has short cantilevers at each end of the span for the purposes of applying end moments.

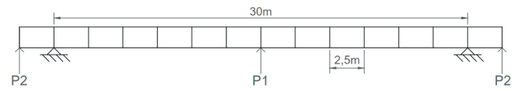

Figure 4: Geometry of beam in parametric study

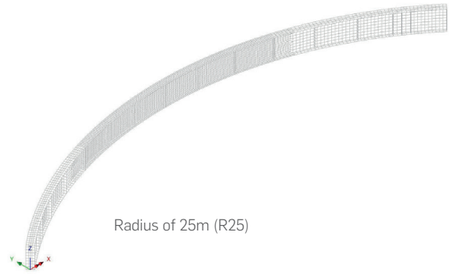

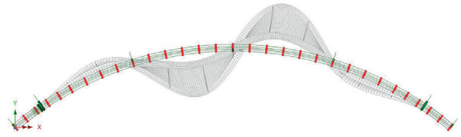

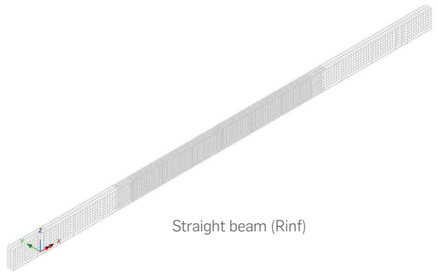

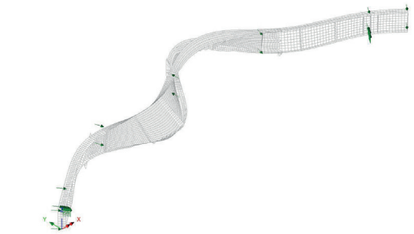

Figure 5: Range of radii considered for parametric study

Different initial geometrical imperfections were considered in investigating the buckling behaviour of the web panels and compression flange.

The overall flange imperfections were based on the lowest global elastic critical buckling mode of the compression flange with magnitude taken in accordance with EN 1993-1-1 clause 5.3.4 (3) and Table 5.1 curve 'd' such that the compression flange typically had a transverse initial imperfection equal to $0.5e_0$=0.5 L/150=0.5 7500/150=25 mm where L was taken as the half wavelength of buckling. See Figure 6. The lowest buckling modes were kept as an asymmetric regardless of the curvature increase.

Web panel imperfections were scaled in accordance with EN 1993-1-5 Table C.2 such that the web had a transverse initial imperfection equal e_0=b/200=1500/200=7.5 mm.

A sensitivity study was carried out with these imperfections and it was concluded that the ultimate resistance was not very sensitive to geometrical imperfections (either shape or magnitude) once the girders became sufficiently curved such that the deliberate curvature itself caused a reduction in bending strength compared to that of a straight girder.

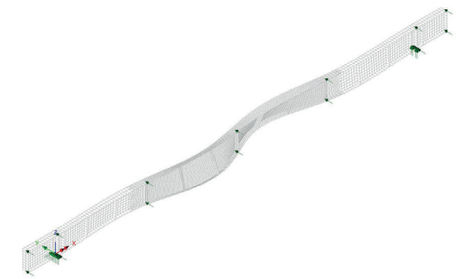

Figure 6: Critical buckling modes for the compression flange

This therefore allowed a high degree of automation using the first global elastic critical buckling model as the initial imperfection.

The steel yield strength was set at 355 MPa for all analyses and the material factor was taken as 1.0 to enable characteristic resistances to be determined. Strain hardening was represented conservatively by a post-yield stress-strain gradient of 1% only and 5% strain was set as the maximum strain in accordance with Annex C of EN 1993-1-5:2006 (Figure 7).

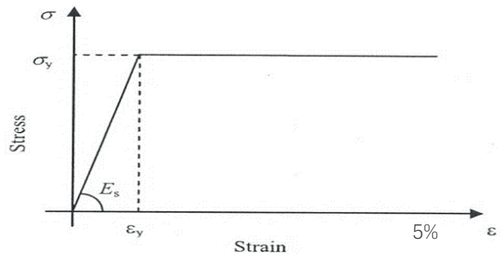

Figure 7: Stress-strain behaviour modelled

All analyses were geometrically and materially non-linear using arc-length control. Internal forces were obtained by integrating the cross-section stress distribution over the girder height.

3.2 Model Loading

Vertical point loading was applied at mid-span and at the end of the beam with each factored separately to produce different ratios of bending moment to shear force at the centre of the span. This simulates the moment and shear forces developed in a continuous bridge girder over an internal support. Case “M” produces pure moment at the centre of the span, case “F3” produces approximately zero moment at midspan and the other cases produce intermediate ratios of bending to shear. The various cases are shown in Figure 8.

3.3 Extent of Parametric Study

The variables considered are presented in Table 1. All combinations of these variables were carried out to model different cases. The number of combinations was 252 per loading, making the total number of analyses equal to 1260.

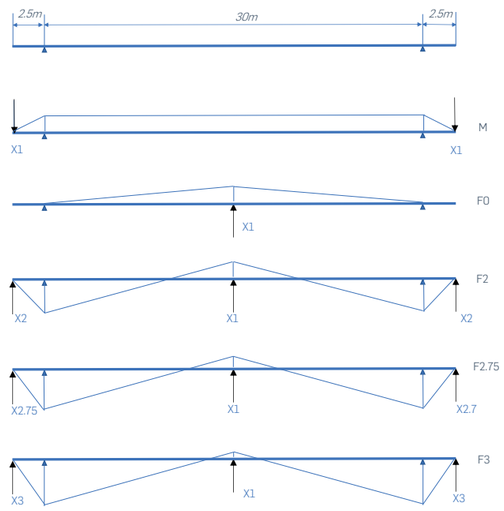

Figure 8: Stress-strain behaviour modelled

3.4 Curvature Parameters

Two important non-dimensional curvature parameters were defined to compare results across different geometries and to ensure a wide and representative range of situations was considered. These were:

(i) The compression flange curvature parameter Z_f defined as follows:

$$Z_f = L^2/Rb \qquad \text{(Equation 1)}$$

where:

L is the spacing of the centres of rigid lateral restraints to the compression flange

R is the radius of the beam in plan
b is the width of compression flange

The studied range of this parameter was from 0.0 to 9.0.

(ii) The web curvature parameter Z_a defined as follows:

$$Z_a = a^2/Rt \qquad \text{(Equation 2)}$$

Table 1: Extent of Parametric Study

Parameter	Symbol	Unit	Values						
Radius	R	m	Straight	500	200	100	50	32	25
Web depth	hw	mm	1500						
Web thickness	t	mm	9	12	15				
Flange width	b	mm	250	320	500	640			
Flange thickness	T	mm	11	14	22	28			
Lateral bracing spacing	L	m	2.5	5	7.5				
Stiffener spacing	a	m	2.5						

where:

R is the radius of the beam in plan
t is the web thickness
a is the spacing of the transverse stiffeners

The studied range of this parameter was from 0 to 30.

4. Results and Conclusions from Parametric Study

4.1 Presentation of Results

The results for all cross-sections in the parameter ranges obtained from Table 1 have been presented in a variety of ways to enable conclusions to be drawn and new design rules proposed. Those in this paper include:

- moment resistance for all cross-sections, bracing spacing and plan radii plotted against the curvature parameter Z_f
- moment resistance for all cross-sections, bracing spacing and plan radii plotted against the slenderness for lateral torsional buckling
- moment resistance for one particular cross-section and bracing spacing with a variable plan radius, plotted against the curvature parameter Z_f
- shear-moment diagrams for a particular cross-section, bracing spacing and plan radius
- shear resistance for one particular cross-section and stiffener spacing with a variable plan radius, plotted against the curvature parameter Z_a

These are discussed in the following sections.

4.2 Moment Resistance With Curvature Parameter Z_f

The moment resistance for all cross-sections, bracing spacing and plan radii, normalised against the moment resistance of the corresponding straight girder, is shown plotted against the curvature parameter Zf in Figure 9, which is based on the F0 loading case shown in Figure 8. The general reduction of moment resistance with increasing flange curvature parameter is apparent. The scatter of points is caused by the different slenderness values of the compression flange considered in the study.

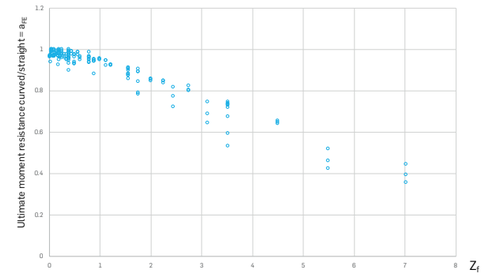

Figure 9: Moment resistance with curvature parameter Z_f

Figure 10 shows the variation of moment resistance with flange curvature parameter Zf for one particular flange width and bracing spacing, but varying web thicknesses. The bending resistances are again plotted normalised against the moment resistance of the corresponding straight girder, represented by α_{FE} which is the ultimate bending resistance for a curved girder divided by that for the

corresponding straight girder. The approximately coincident points at each curvature reflect different web thicknesses, but the reduction of moment resistance with an increasing flange curvature parameter for the same girder is apparent.

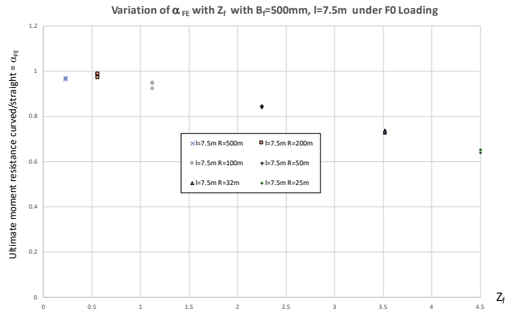

Figure 10: Moment resistance with curvature parameter Zf for one particular flange size and bracing spacing

4.3 Moment Resistance with Slenderness for Lateral Torsional Buckling

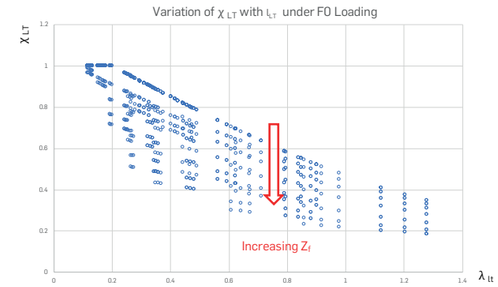

Figure 11: Moment resistance with slenderness for lateral torsional buckling λ_{AT}

The reduction factor χ_{LT}, for moment buckling resistance compared to the cross-section moment resistance for all cross-sections, bracings spacings and plan radii is shown plotted against the slenderness for lateral torsional buckling, λ_{LT}, in Figure 11, which is based on the F0 loading case shown in Figure 8. The general reduction of moment resistance with increasing slenderness is apparent. The scatter of points is caused by the different curvature parameter values of the compression flange considered in the study and it is further apparent that the plan curvature can cause a very significant reduction in the bending resistance compared to the strength of the equivalent straight girder.

4.4 Shear-Moment Interaction

The shear-moment interaction behaviour is illustrated here by comparing the resistance of a straight girder cross-section with 500 mm x 22 mm flanges and a 1500 mm x 12 mm web against the same girder with a plan radius of 25 m.

Figure 12 shows the results for the straight girder alone with a bracing spacing of 2.5 m. Figure 13 shows the same case as Figure 12, together with the curved girder and bracing spacings of 2.5 m, 5.0 m and 7.5 m. All points have been plotted against the interaction diagram for the cross-section resistance of a straight girder to EN 1993-1-5:2006 section 7.1. The points are labelled so that the relevant flange and web curvature parameters, together with the loading-type, can be identified. The labelling convention is as follows Z_f - Z_a – Load configuration" so, for example, the resulting point for a girder with flange curvature of 0.5, web curvature of 20.83 and loading case M would be described by 0.5-20.83-M.

The results indicate the large influence of both the bracing spacing (as is expected) and flange curvature parameter on strength. Figure 12 for the straight girder shows that the girder's actual resistance mostly lies on the safe side (the outside) of the EN 1993-1-5 interaction curve. The points for low shear and high moment (M and F0) lie slightly inside the curve because the bracing spacing of 2.5 m used leads to a slight reduction in moment resistance due to lateral torsional buckling which has to be checked separately from the interaction curve. The points for high shear (F3 and F2.75) show that the EN 1993-1-5 interaction curve is safe-sided.

Figure 13 shows the reduction in bending strength from both flange curvature and bracing spacing, the two being linked. The point labelled 0.5-20.83-M on the moment axis shows the reduction in strength from the 0-0-M case caused by reducing the radius to 25 m whilst maintaining the bracing spacing at 2.5m. The other cases on the moment axis, 4.5-20.83-M and 2.0-20.83-M, illustrate the reduction caused by reducing the radius to 25 m whilst also increasing the bracing spacing to 7.5 m and 5.0 m respectively. It should be noted that, for the curved girder, increasing the bracing spacing has two effects on resistance – it increases the slenderness of the compression flange (which would reduce the strength also of the equivalent straight girder also) and it also increases the curvature parameter for the flange (thus introducing more transverse bending into the flange).

In Figure 13, the points for high shear cases (e.g. F3 and F2.75) are inside the interaction curve of EN 1993-1-5 when the girder has a plan radius of 25 m hence EN 1993-1-5 no longer provides a safe estimate of shear strength in this situation.

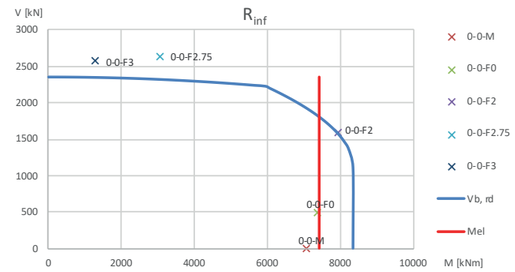

Figure 12: Shear-moment interaction for straight girder

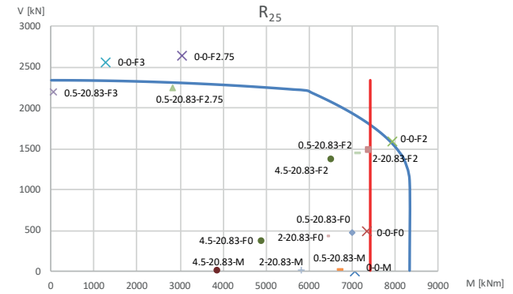

Figure 13: Shear-moment interaction for straight girder and girder with radius in plan of 25 m

4.5 Conclusions From Parametric Study

It can be observed from the above discussions that:

- The resistance to both moment and shear is reduced by in-plan curvature
- The curvature parameters Zf and Za for flange and web respectively are important parameters influencing the resistance
- The lateral bracing spacing is an important parameter irrespective of Zf in determining ultimate moment (slenderness) but Zf reduces the bending strength further at any given slenderness.

New design rules are required to incorporate these curvature effects. These are discussed in the next section.

5. New Proposed Design Rules

5.1 Overview

In the following sections, design rules have been developed to adapt those existing rules for straight girders. Rules are developed for bending resistance, shear resistance and the interaction between them for horizontally curved girders by introducing the curvature parameters for the compression flange and web.

5.2 Bending Resistance

It is observed that the curvature of the girder in plan creates an additional out-of-plane geometrical imperfection in the flange. Even nominally straight girders are considered to have a practical out-of-straightness caused by fabrication tolerances which leads to an initial bow in compression flanges which is included in the buckling curves of EN 1993-1-1:2005 via the imperfection parameter $\eta=\alpha_{LT}\ (\lambda\text{-}0.2)$ from clause 6.3.2.2.

The background to this imperfection parameter can be found in many sources including Hendy CR and Murphy CJ (2007). The Perry-Robertson theory described therein describes an imperfection parameter for geometric imperfections equal to $(y\ e_0)/i^2$ where y is half the flange width, i is the radius of gyration and e_0 is the offset from a straight line due to fabrication tolerances plus an additional allowance for residual stresses in welded girders.

If deliberate curvature from a curved girder is considered, the additional imperfection from this curvature, based on the offset from a straight line caused by the plan radius R acting over a rigid bracing spacing of L, gives an additional term in the imperfection parameter which is dependent on the strut end boundary conditions (Equations 3 & 4) and as illustrated in Figure 14:

$$\frac{y\,e_0}{i^2} = \frac{3L^2}{4Rb} = 0.75Z_f \quad \text{pin-ended strut} \quad \text{(Equation 3)}$$

$$\frac{y\,e_0}{i^2} = \frac{3L^2}{8Rb} = 0.375Z_f \quad \text{built-in continuous strut} \quad \text{(Equation 4)}$$

Unlike for a straight beam, where both buckling mode and initial imperfection can be in opposite directions in adjacent braced bays, in a curved beam the systematic imperfection from the plan curvature will always promote buckling in one bay but oppose it in the adjacent bays. Hence the built-in continuous strut treatment of the imperfection from deliberate curvature is more appropriate in most geometries.

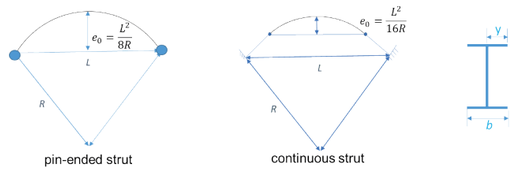

Figure 14: Offsets to consider in flange design based on boundary conditions

In reality, the actual contribution of this systematic imperfection from deliberate curvature is best determined from the parametric study. The proposal for adapting the bending resistance was thus to consider the effect of the horizontal beam curvature by enhancing the imperfection on the straight girder via the curvature parameter Z_f as follows:

$$\eta = \alpha(\bar{\lambda} - 0.2) + XZ_f \qquad \text{(Equation 5)}$$

with the parameter X chosen to fit the experimental results.

The bending resistance $M_{b,Rd}$ for beams with uniform curvature in plan can then be determined following the same approach as used in EN 1993-1-1:2005 for straight girders. The design buckling resistance moment should then be taken as:

$$M_{b,Rd} = \chi_{LT} W_y \frac{f_y}{\gamma_{M1}} \qquad \text{(Equation 6)}$$

where Wy is the appropriate section modulus as follows:

$W_y = W_{pl,y}$ for Class 1 or 2 cross-sections

$W_y = W_{el,y}$ for Class 3 cross-sections

$W_y = W_{eff,y}$ for Class 4 cross-sections

χ_{LT} is the reduction factor for lateral-torsional buckling.

$$\chi_{LT} = \frac{1}{\Phi_{LT} + \sqrt{\Phi_{LT}^2 - \bar{\lambda}_{LT}^2}} \text{ but } \chi_{LT} \leq 1 \qquad \text{(Equation 7)}$$

where Φ_{LT} is modified compared to the definition in EN 1993-1-1 to include a term "XZ_f " as follows:

$$0.5\left[1 + \alpha_{LT}(\bar{\lambda}_{LT} - 0.2) + X\,Z_f + \bar{\lambda}_{LT}^2\right] \qquad \text{(Equation 8)}$$

α_{LT} is the imperfection factor as defined in EN 1993-1-1 for the particular cross-section being considered;

$\bar{\lambda}_{LT} = \sqrt{((W_{yfy})/M_{cr})}$ is the slenderness as defined in EN 1993-1-1 and Mcr is the elastic critical moment for lateral-torsional buckling.

For a beam curved in plan, Mcr may be determined for either the actual curved geometry and restraints or for an equivalent straight girder; the latter will typically lead to a slightly smaller value of Mcr which is conservative for design, but it ensures that the slenderness can be determined based on hand-calculation methods without the need for a computer elastic critical buckling analysis.

X takes into account the contribution of the plan curvature in increasing the effective imperfection in the compression flange. The study found that the values of X below provide the best fit to the test results:

X = 0.0 for Zf ≤ 0.2
X = 0.2 for 0.2 < Zf ≤ 4
X = 0.25 for 4 < Zf < 9

Figure 15 shows the test results for the actual reduction factor to the cross-section bending strength, X_{FE}, obtained from the non-linear parametric study for various curvatures, Z_f, against the bounding proposed curves, X_{LT}, for zero curvature and an extreme curvature $Z_f = 9$.

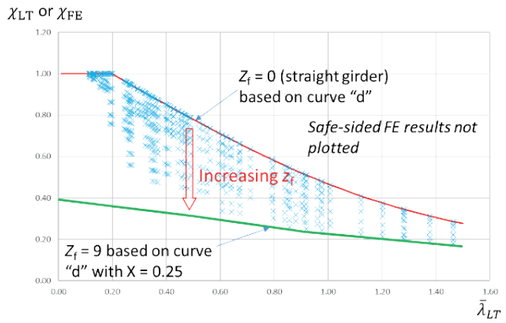

Figure 15: Reduction factor X_{FE} for various curvatures Z_f against the bounding proposed curves X_{LT}

The proposed curves X_{LT} for different flange curvatures, which are based on EN 1993-1-1 buckling curve 'd' are typically used for welded bridge girders, shown in Figure 16. The figure also shows EN 1993-1-1 buckling curve 'a', which is very significantly different to curve 'd'. The study has shown that where $Z_f \leq 0.2$, a beam may be treated as straight for the purposes of determining lateral torsional buckling resistance. This cut-off is permitted because of the use of curve 'd' for straight girders appears to be fundamentally conservative. It is therefore very important to note that the calibration of X and the values specified for use in Φ_{LT} assume that curve 'd' will continue to be used for welded bridge girders. If the specified curve were to change, X needs to be recalibrated.

The proposed values of X also assume a uniform radius in plan. If the bridge has a significantly larger radius adjacent to the length of girder being checked for buckling then a larger value of X may be required to be used as the benefit to the effective buckling end restraint conditions is reduced.

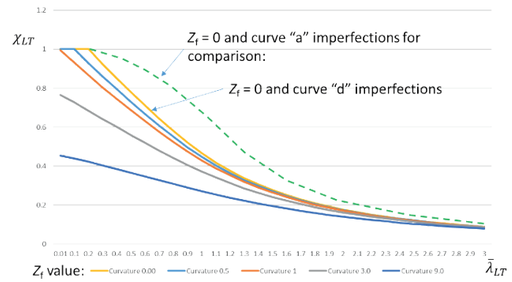

Figure 16: Proposed curves X_{LT} based on EN 1993-1-1 curve 'd'

Figure 17 shows an example of how predicted bending resistance for a girder with a 500 mm wide flange and bracing spacing of 7.5 m compares with the non-linear results and also the codified resistance of the equivalent straight girder. It can be seen that the predictions follow the trend of the non-linear results but are conservative at low curvature because the existing EN 1993-1-1 curve 'd' results for straight girders are themselves conservative.

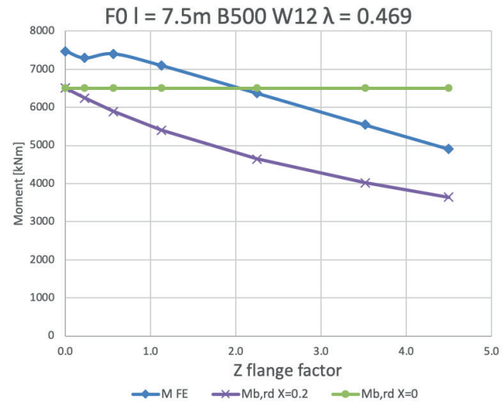

Figure 17: Proposed moment resistance of curve flange, parametric study and resistance of flat flange.

5.3 Shear Resistance

The results for shear were also reviewed with a view to producing rules for the design of bridges with beams curved in plan, as increasing web curvature was clearly shown to reduce the ultimate shear strength of webs. Although it increased the elastic critical buckling resistance as other researchers have found, however, the relatively few results obtained for girders with high shear made it difficult to derive the new rules directly, but it did facilitate the checking of proposals of one of the other project partners, Universidade de Coimbra. A critical parameter for adjusting the reduction factor for shear for beams with curvature in plan is the curvature parameter Z_a as quoted in 3.4.

The following rules were proposed by Universidade de Coimbra and published in two journal papers (Filip Ljubinković et al. (2019a) and Filip Ljubinković et al. (2019b)) and validated by this parametric study.

Where $Z_\alpha \leq 1.0$, the design shear buckling resistance may be determined in accordance with the rules in EN 1993-1-5 clause 5.1(1) for flat plates.

Where $1.0 < Z_\alpha < 50$, the design shear buckling resistance may be taken as:

$$V_{b,Rd} = V_{bw,Rd} = \chi_w h_w t \frac{f_{yw}}{\sqrt{3}\gamma_{M1}} \qquad \text{(Equation 9)}$$

where χ_w is determined as follows:

$\chi_w = 1.0$ for $\bar{\lambda}_w \leq \bar{\lambda}_{w,0}$

$\chi_w = A_\chi \bar{\lambda}_w^2 + B_\chi \bar{\lambda}_w + C_\chi$ for $\bar{\lambda}_{w,0} < \bar{\lambda}_w < 1.1$

$\chi_w = \frac{A_\chi}{B_\chi + \bar{\lambda}_w}$ for $1.1 \leq \bar{\lambda}_w \leq 3.0$

And $\bar{\lambda}_{w,0} = \begin{cases} 0.4, & Z_a \leq 30 \\ 0.3, & Z_a > 30 \end{cases}$

and A_χ, B_χ and C_χ should be taken from Table 2.

Table 2: A_X, B_X and C_X parameters

$\bar{\lambda}_{w,0} < \bar{\lambda}_w < 1.1$	$A_\chi = -\frac{Z_a}{57.7} - 0.48$	$B_\chi = \frac{Z_a}{86} + 0.25$	$C_\chi = -\frac{Z_a}{367} + 1.0$
$1.1 \leq \bar{\lambda}_w \leq 3.0$	$A_\chi = \frac{335.5 - Z_a}{380}$		$B_\chi = \frac{3.7 + Z_a}{47.5}$

The slenderness $\bar{\lambda}_w = \frac{a/t}{37.4\varepsilon\sqrt{k_{\tau,Z_a}}}$ with $k_{\tau,Z_a} = A_k + B_k\left(\frac{1}{\alpha}\right)^2$ and A_k and B_k taken from Table 3 where $\alpha = \frac{h_w}{a}$.

Table 3: A_k and B_k parameters

$\alpha \leq 1$	$A_k = 0.214Z_a + 2.88$	$B_k = 5.343 - \frac{Z_a}{175.6}$
$\alpha > 1$	$A_k = 0.096Z_a + 5.15$	$B_k = 0.135Z_a + 3.18$

Bridge girder webs will usually have their longitudinal edges flexibly restrained by the flanges against movement into the plane of the web, and their vertical edges similarly restrained against in-plane movement by either rigid end posts or by the adjacent web where the panel considered is remote from a free edge. The former restraint mechanism gives rise to the additional shear resistance contribution from the flange and the latter generates the rigid end post case for webs in straight girders. It will be noted that the rules above for shear strength of curved webs consider neither of these beneficial membrane restraints and so the shear resistances derived will typically be conservative.

Figure 18 below shows a comparison of the predicted shear strength of a 12 mm thick web with different curvatures against the results from the non-linear parametric study and also the equivalent straight web resistance calculated using the rigid and non-rigid end post cases. It can be seen that

the prediction follows the results from the parametric study in terms of trend with increasing web curvature, but it is slightly conservative. The case shown also indicates that the rules for flat webs safely predict the strength of a curved web until the curvature reaches quite a high level.

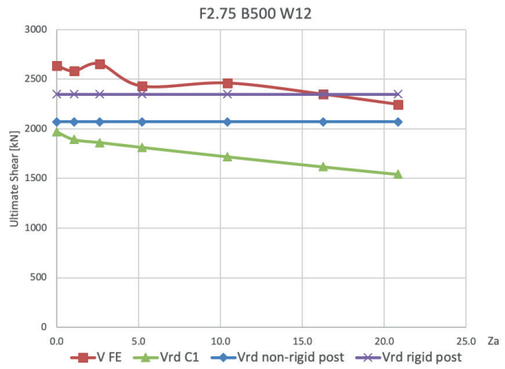

Figure 18: Proposed shear resistance of curved webs, parametric study results and resistance of flat webs

5.4 Shear-Moment Interaction

Provided that the shear resistance is calculated as per section 5.3 above and the bending resistance is truncated by the buckling resistance in section 5.2 then the interaction between bending and shear in BS EN 1993-1-5 : 2006 clause 7.1 may be used. The buckling resistance in section 5.2 above itself contains an interaction with shear because, for a given bending moment, an increase in shear reduces the slenderness for bending hence it increases the bending resistance. This can be seen indicatively in Figure 19.

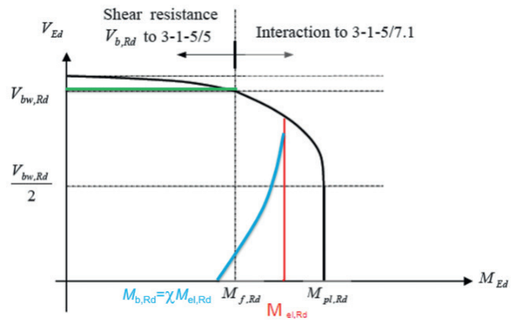

Figure 19: Shear-moment interaction diagram according to EN 1993-1-5

5.5 Limitations of Applicability

All of the parametric study results assume that no torsional load is applied between points of transverse restraints so any design rules derived on this basis must also only be applied to situations where zero or insignificant torsional moment is applied between restraints. This restriction allows rules to be derived which consider only the moment and shear at each end of the girder between restraints and the plan curvature in between without a direct inclusion of the torsion. This criterion will be satisfied for normal steel-concrete composite bridges with the deck slab on top of the beams since the torsional moment transmitted from deck slab to girder is usually small. Where significant torsional moments can be applied between torsional restraints, such as during construction with cantilevering forms being used to construct the deck slab cantilevers, an alternative method will need to be used for that condition.

Girders with longitudinally stiffened webs cannot be assessed by the proposed rules. Longitudinally stiffened webs were not considered in the study so, whilst web sub-panels could be checked for shear, overall shear buckling cannot.

6. Conclusion and Further Work Required

The rules presented here provide a simple method of verifying the adequacy of curved plate girders using moment and shear stress resultants without the need to consider the detailed stresses developed within the cross-section. The rules avoid a discontinuity with the approach taken for straight girders and provide an economical design that takes full benefit of a non-linear parametric study.

Further work is required to provide design rules for plate girders with longitudinal stiffeners and girders with concentrated applied torque between bracings, but this is not a major limitation for the design of typical steel-concrete composite construction.

Acknowledgements

The authors would like to thank Kevin Aznar Santiago for his contribution to the project whilst working at Atkins.

References

AASHTO (2007). LRFD bridge design specifications, American Association of State Highway and Transportation Office, Inc., Washington DC, USA.

BS EN 1993-1-1 (2005), Eurocode 3: Design of Steel Structures – Part 1-1. General rules and rules for buildings. BSI, London, UK.

BS EN 1993-1-5 (2006), Eurocode 3: Design of Steel Structures – Part 1-5. Plated structural elements. BSI, London, UK.

Ljubinkovic, F., Martins, J.P., Gervásio, H., Simões da Silva, L. (2019a) Eigenvalue analysis of cylindrically curved steel panels under pure shear stresses. Thin-Walled Struct. 141 (2019) 447–459.

Ljubinkovic, F., Martins, J.P., Gervásio, H., Simões da Silva, L. (2019b) Ultimate load of cylindrically curved steel panels under pure shear. Thin-Walled Structures 142 (2019) 171–188.

Hendy CR and Murphy CJ (2007) Designers' Guide to EN 1993-2, Steel Bridges, Thomas Telford, London, UK.

Hendy CR and Johnson RP (2006) Designers' Guide to EN 1994-2, Composite Bridges, Thomas Telford, London, UK.

Jung, S. K., and D. W. White (2005) Shear Strength Of Horizontally Curves Steel I-Girders - Finite Element Analysis Studies. Journal of Construction Steel Research, Vol. 62, pp. 329-342.

Linzell, D., Hall, D., White, D. (2004) Historical Perspective on Horizontally Curved I Girder Bridge Design in the United States. Journal of Bridge Engineering, American Society of Civil Engineers (ASCE), 208-229.

LUSAS Finite Element Analysis (2017), LUSAS, Kingston upon Thames, UK.

Presta, F., Hendy, C.R., Turco, E. (2008) Numerical validation of simplified theories for design rules of transversely stiffeed plate girders. The Structural Engineer (Institution of Structural Engineers), pp. 37-46.

Flexural Strengthening of Historic Timber Beams Using Prestressed Steel Cables

Dr. Dermot O'Dwyer

Civil, Structural and Environmental Engineering Department, Trinity College Dublin
Dublin, Ireland

Anthony J. Browne

MSc Eng CEng MIEI
Senior Engineer, Infrastructure Division Engineering, Design and Project Management
Dublin, Ireland

Abstract

In this paper, results of flexural tests aimed at improving the structural behaviour of softwood timber beams by using steel cables fixed to the bottom section of beams through steel spigots as an alternative to current strengthening techniques are presented. The motivation behind this paper is to develop an alternative method of strengthening softwood timber beams in lieu of the current methods which heavily depend on resins and do not abide by conservation guidelines. In the system proposed, the tensile forces are restrained by the spigots and, therefore, there is an increase in strength, an increase in stiffness and a reduction in the probability of tension failure occurring. The key advantages of this system are that it is relatively easy to retrofit into existing structures compared to other strengthening techniques; it is fully reversible; and there is no need for expensive resins, which can be difficult to apply and have poor performance at high temperatures. The analysis of the behaviour and failure modes of the reinforced beams is the focus of this paper. A 3D finite element model is presented for simulating the linear behaviour of the timber beams reinforced with the steel cables and spigots. Additionally, presented is an experimental analysis where a modest number of unreinforced and reinforced beams are tested and compared with the theoretical results.

Keywords

Softwood; Timber beam reinforcement; Steel cables; Bending tests; FE analysis

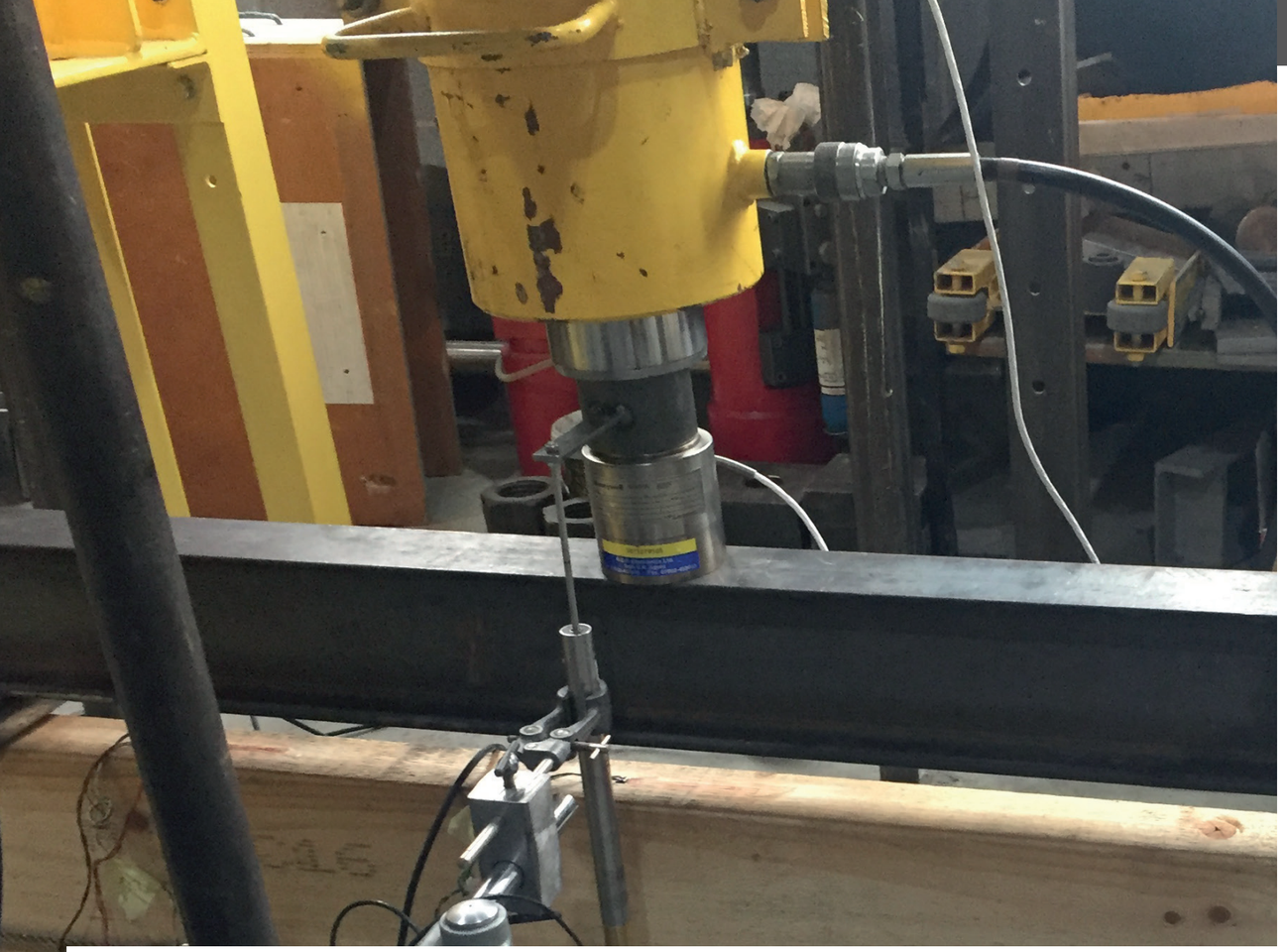

1. Introduction

Softwood timber beams as a traditional building material has been extensively used from antiquity to the present day. This is mainly due to their excellent workability, low weight density, and strength. However, splits caused during seasoning, natural defects, and degradation may affect mechanical properties and result in a decrease of capacity. The reduction in tensile strength over time can be up to 90% (Thelandersson et al, 2003). In addition, existing timber beams may need to be strengthened due to change of building use and negligent human interaction. The type of softwood chosen for this study is Sikta spruce (Picea sitchensis), as this type of softwood is relatively inexpensive and frequently used in Ireland and the UK (Arya, C., 2009).

In the past century, there has been a focus on conservation of historic structures (Miele, 2005). This paper presents a proposal to facilitate conservation works where the strengthening of softwood beams is required. Softwood timber beams that require strengthening are usually replaced or reinforced with traditional methods involving the use of standard building materials such as steel or aluminium plates. However, other options have recently been developed. Examples of other options include bonded carbon fibre or basalt fibre composites (de la Rosa Garcia et al, 2013), bonded steel plates (Jasieńko et al, 2014), bonded carbon fibre reinforced polymer (Brunner and Schnueriger, 2004) (Nowak, 2013) (Khelifa and Celzard, 2014), unbonded fibre-reinforced polymer composites (Corradi et al, 2016), bonded high strength steel cords (Borri, and Corradi, 2011) and bonded prestressed fibre-reinforced polymer (Brunner and Schnueriger, 2004) (Brunner and Schnueriger, 2005). However, issues remain to be solved. For example, most of these techniques require the use of oil-based adhesives (e.g. epoxy resins) which present problems such as limited durability, low reversibility, and poor performance at high temperatures. In addition, these techniques can be difficult to retrofit into existing structures and do not abide by the legislative and ethical conservation requirements in many countries (Feilden, 2007). Therefore, the motivation behind this study is to develop a reinforcement system for softwood timber beams that can eliminate these issues.

2. Proposal

Timber has a high tensile strength compared to its compressive strength. However, in real-world structures, its tensile strength can be lower due to the presence of defects, such as knots. For this reason, and the fact that timber exhibits ductile behaviour in compression and brittle behaviour in tension, when softwood timber beams fail they typically fail on the tension side of the beam. When timber experiences brittle failure the failure is sudden, which is always undesirable in real structures. Therefore, in an effort to reduce the tensile stresses in the beam, it was proposed to reinforce the bottom section of timber beams using steel cables fixed to each side of the timber beam, shown in Fig. 1. This system is solely dependent on mechanical fixings and is therefore fully reversible.

This proposal was developed further by the introduction of a compressive force via a tensioning system. The development of this system is discussed further below.

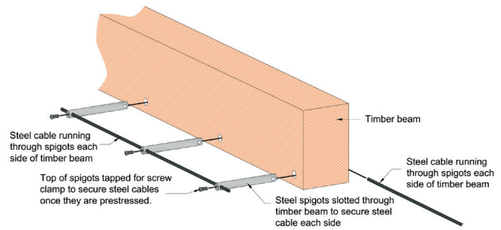

Figure 1: Illustration of reinforcement system.

3. Mechanical Properties of the Materials

3.1 Material Characterisation

To accurately model the behaviour of the unreinforced and reinforced beams using numerical analysis, material characterisation tests were performed on timber samples. A series of characterisation tests on timber samples were performed in accordance with BS EN 384:2016. The results are given in Table 1.

Table 1: Properties of the Timber Tested in Accordance With BS EN 384:2016

Timber species	**Sitka spruce (Picea sitchensis)**
Structural grade	C16
Beam type	Solid
Weight density (kg/m^3)	390
Moisture Content (%)	14
Tensile strength (N/mm^2)	22
Compressive strength (N/mm^2)	17
Modulus of elasticity (N/mm^2)	7828

3.2 Testing of Spigots

As the interaction between the timber and the steel cable is dependent on the interaction between the timber and the spigot, an investigation into the effects of the spigot diameter was performed to establish the maximum force and resultant stress and strain that can be applied to each spigot prior to rupture and to determine if a linear correlation existed between the maximum stress and maximum strain to the diameter of the spigot.

To establish the response of the timber when the spigots were loaded, a rig, as shown in Fig. 2, was assembled. A force was then applied to the spigot to establish the force required to push the spigot through the timber sample.

Figure 2: Spigot testing

The spigots were loaded symmetrically and asymmetrically and no discernible difference in response was observed between the symmetrically and asymmetrically loaded specimens. The stress experienced around the spigot and the strain response were recorded and can be seen in the graph shown in Fig. 3.

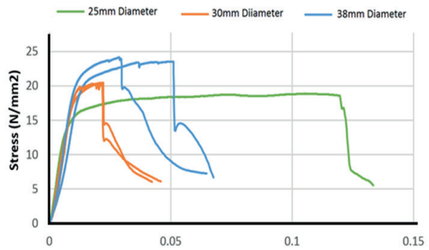

Figure 3: Strain vs Stress for spigot push through test.

From the characterisation tests performed, it was established that the maximum yield strength in compression was approximately 17 N/mm^2. From the graph shown in Fig. 3, the larger diameter spigots can apply greater stress to the timber before rupture. When using the smaller diameter spigots, the timber can undergo a greater degree of strain before rupture. Further analysis is required to fully understand the behaviour of the timber around the spigot. As there is a dramatic difference in the response of the 25 mm diameter and 38 mm diameter spigots, it was decided to test the reinforcement system using both of these sized spigots and record if a major difference in performance occurred.

Further study using finite element software indicated that, from the elastic analysis of the reinforced beams in bending, large stresses and strains are generated around the spigots, as shown in Fig. 4. Later in this study it can be seen from the experimental tests that the locations where these high stresses and strains are shown to be generated are the locations where failure occurred.

These large stresses can be dissipated by plastic deformation occurring around the spigot. The plastic deformation is facilitated through ductility of the material.

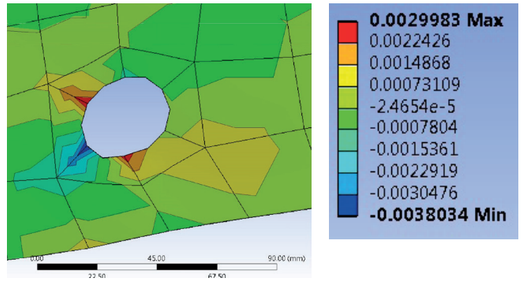

Figure 4: Ansys image showing stress at spigot location

3.3 Steel Cables

As the restraint provided by the spigots depended on the strength of the cable and the capacity of the clamps, tests were performed to establish these parameters. A test was performed in order to establish the ultimate capacity of the cable with the clamps and if any slippage of the clamps would occur. The test consisted of two clamps fastened to the cable. The clamps were placed behind two steel plates which were then pulled apart. This layout is shown in Fig. 5.

Figure 5: Image of cable and D clamp testing rig

From the spigot testing it was calculated that 10 mm ø cables would be adequate. The cables were secured to the spigots using D clamps initially manufactured from stainless steel and tightened to a recommended torque of 19 Nm (Fastenal, 2017). The results of this test can be seen in Fig. 5. From the literature, the ultimate strength of the cable is approximately 60 kN (Tripyramid, 2017). However, the ultimate strength reached for this test was determined to be approximately 7.8 kN. When the load was reduced, there was marginal displacement recovery recorded and therefore it can be assumed that the displacement and ultimate strength reduction was due to slippage of the clamps. To reduce the slippage and increase the ultimate capacity of the clamps, the stainless steel D clamps were replaced with mild steel D clamps where the recommended torque is 25 Nm (Integrated Publishing, 2017). As seen in Fig. 6, using the mild steel clamps, the slippage was not reduced but the ultimate strength was increased. However, is was decided to use the mild steel clamps for the experiential bending tests for the reinforced beams, due to the increase in ultimate capacity.

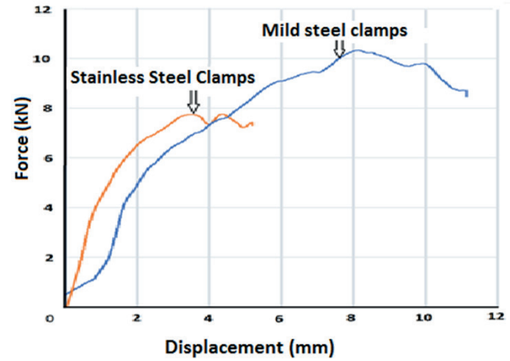

Figure 6: Force vs Displacement for cables with clamps

4. Numerical Analysis

In order to understand the mechanics of the reinforced system, the mechanics of an unreinforced beam we first studied. As an unreinforced timber beam is subjected to a load, it starts to bend. As it bends, the top section of the beam compresses and the bottom section of the beam expands. For a reinforced beam, as the bottom section begins to expand, it is restrained by the spigots and the cable.

Therefore, the expected behaviour of the beam subjected to load is expected as follows:

1. Compression stresses are generated in the top section of the beam.
2. Tensile stresses are generated in the bottom section of the beam.
3. As these stresses develop, compression forces are generated in front of the spigots.

These forces are illustrated in Fig. 7.

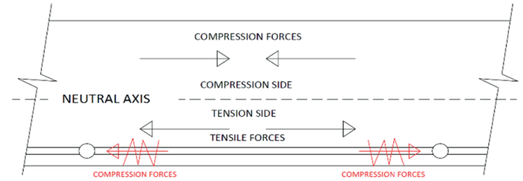

Figure 7: Diagram of forces induced during bending

In theory, the distance between the spigots does not change as they are fixed with the cable. Therefore, the sum of the elastic strains between the spigots should equal zero. It is expected that the stress distributions of the reinforced beam are complex. The reinforced beam experiences different stress distributions in different parts of the beam. Compressive stresses are generated in the area immediately in front of a spigot and tension stresses are generated behind the spigot. Therefore, it is expected that a shear plane would be generated between the tension and compression strains.

For the analysis, three different reinforcement arrangements were used: (a) 4 no. 38 mm ø spigots at 800 mm centres, (b) 4 no. 25 mm ø spigots at 800 mm centres, and (c) 8 no. 25 mm ø spigots at 400 mm centres.

To develop a greater understanding of the stress distributions, a linear static analysis was carried out on a complete three-dimensional finite element (FE) model of both unreinforced and reinforced softwood beams. Simulation was made using academic software Ansys®, version R17.2. The numerical model was built to accurately reproduce the geometry of the specimens, the presence of imperfections was disregarded. The geometry of the timber beams was firstly reconstructed by means of CAD tools. Next, the volumes were imported and modelled using Solid45 elements (3D eight-node cubic isoperimetric elements), which are defined by eight nodes with three degrees of freedom at each node and orthotropic material properties. The mesh size applied across the specimen cross section was 30 mm × 30 mm. This is the minimum cell size available for the academic software. The FE model onsisted of 13,984 nodes and 7,208 elements, with 41,952 degrees of freedom. Values concerning the physical properties of timber were established on statistical analysis of test data from the mechanical characterisation tests.

The numerical analysis was carried out for a load dependant bending test in accordance with EN 408 using a four-point bending test as shown in Fig. 8. This was also the arrangement used for the experimental analysis. The of results of the tests are presented in Fig. 13 and summarised in Table 2.

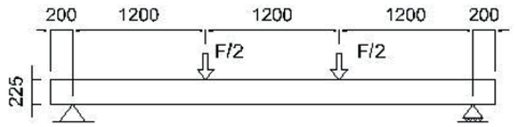

Figure 8: Four-point bending test according to European Standard EN408

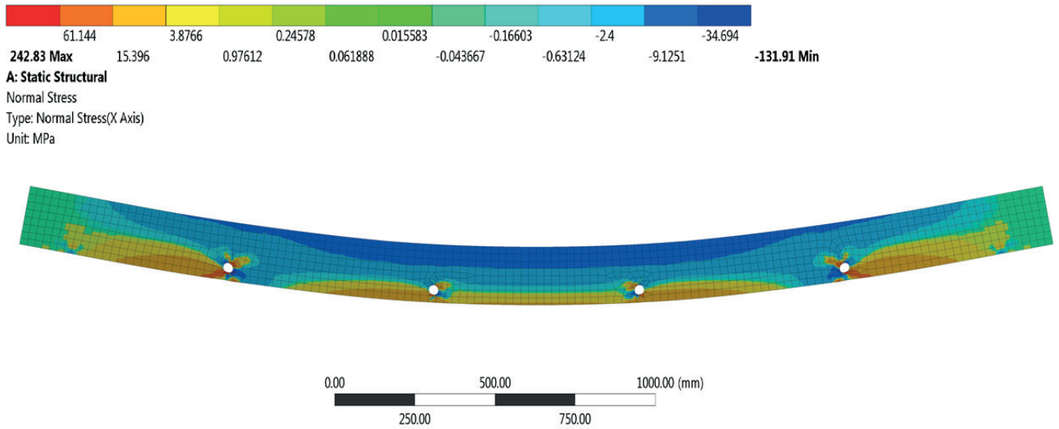

Figure 9: Ansys model of reinforced beams with 4 no. 38 mm ø spigots

From the models, it can be seen that there is less stress generated at the top surface of the reinforced beams compared to the unreinforced beams. This is due to a reorientation of the neutral axis and there is now a greater area for the compressive forces to act. However, the bottom surfaces do experience peaks of stress at the spigot locations. The reduced compression at the top surface and the varying stress in the bottom surface correlates with the recordings from the strain gauges applied in the experimental analysis.

Although, for the analysis, it was assumed that the spigots were fully restrained by the cables. However, in reality, the cables will stretch, and slippage of the clamps will occur resulting in movement of the spigots. The amount of restraint provided by the cables and clamps can be calculated from Newton's Third Law. The force exerted by the timber on the spigot equals the force exerted by the spigot on the timber. The force experienced by the spigot is transferred into the cables. Therefore, from the diagram in Fig. 10, it can be assumed that $F_c = 2_{Ft}$. Using the fact that force equals stress divided by area and that stress equals strain multiplied by elastic modulus the following equation can be derived:

$$\varepsilon_c = \frac{A_1 \times \varepsilon_t \times E_t}{A_2 \times 2E_c}$$

Where:

ε_c = *Strain in the cable between the spigots*

ε_t = *Strain in the timber between the spigots*

A_1 = *Area of the spigot exerting force on the timber*

A_2 = *Total cross sectional area of the steel cables*

E_c = *Apparent elastic modulus of the cables incorporating clamps*

E_t = *Elastic modulus of the timber*

To find the actual stress field at maximum load, the FE model was subjected to both self-weight and two-point load pressure under different load stages. Fig. 9 shows the theoretical stress fields for each reinforcement system for a fully elastic response. In practise, the large stresses around the spigots will be dissipated through plastic deformation. The approximate failure of the beam was predicted to occur when the strain around the spigot reached the ultimate values observed when testing the spigots.

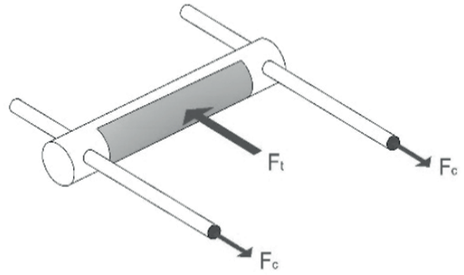

Figure 10: Force vs displacement for cables with clamps

The E_c value can be calculated as approximately 8200 N/mm^2 from the graph shown in Fig. 6. From the timber characterisation test, the value of E_t was established as 7828 N/mm^2. Therefore, it can be calculated that the sum of the stain in timber is equal to 0.17 of the strains in the cable:

$$\varepsilon_t = 0.17\ \varepsilon_c$$

The strain in the timber between the spigots is the sum of compression and tension strains.

If the resistance of the clamps to slippage is increased the strain in the cables can be reduced.

5. Test Results

To confirm the results of the numerical analysis, real timber beams were reinforced with the application of steel cables and subjected to bending tests. To establish the effectiveness of the reinforcement, as described above, three different geometrical arrangements were assessed. Fig. 11 shows images of one of these arrangements.

Figure 11: Reinforced timber beams with 4 no. 38 mm ø spigots

The beams were then subjected to bending tests in accordance with the numerical analysis using the rig shown in Fig. 12.

Figure 12: Testing for four-point bending tests.

In addition to these assemblies, a prestressed timber beam with 8 no. 25 mm diameter spigots was also tested. A camber was formed in a beam using the hydraulic jack. The steel cable was then fixed.

As predicted in the numerical analysis, the tests carried out on the reinforced beams in this study showed an increase in performance in terms of stiffness and ultimate strength. The FE model for unreinforced timber showed a good correlation with the experimental results. However, the FE modelling used to understand the behaviour of the reinforced beams predicted a much stiffer beam than what was achieved. The graph in Fig. 13 was created using the results of the FE models and the experimental results. From the graph, it is seen that there is a wide range of experimental results and there is also a large gap between the experimental results and the Ansys model. This is discussed further below. The corresponding reinforcement arrangement for each beam reference is listed in Table 2.

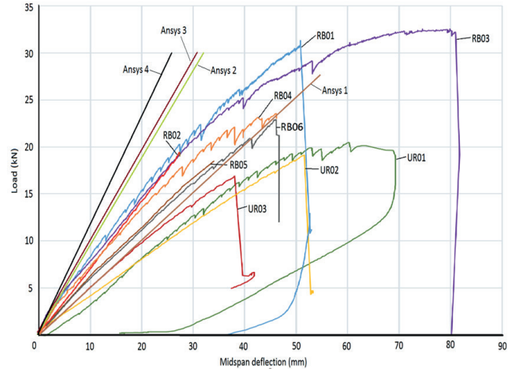

Figure 13: Ultimate static load-deflection plots for unreinforced and reinforced sitka spruce softwood beams.

Table 2: Test Results for Unreinforced and Reinforced Sitka Spruce Softwood Beams.

Beam Ref.	Strengthening	Failure Mode	Max Load Pmax (kN)	Deflection δmax (mm)	δ 15kN	k15Kn(kN/mm)
UR01	Unreinforced	Tensile	20.46	60.37	36.01	0.42
UR02	Unreinforced	Tensile	19.16	51.57	38.51	0.39
UR03	Unreinforced	Tensile	16.89	38.08	33.25	0.45
RB01	4 no. 38 mm ø spigots	Tension Crack	31.31	50.85	19.80	0.77
RB02	8 no. 25 mm ø spigots	Lateral Buckle	>20.11	46.38	21.06	0.71
RB03	4 no. 25 mm ø spigots	Tension Crack	32.55	77.21	20.98	0.57
RB04	8 no. 25 mm ø spigots	Lateral Buckle	>26.05	49.36	23.14	0.65
RB05	4 no. 38 mm ø spigots	Lateral Buckle	>20.11	46.38	26.77	0.60
RB06	8 no. 25 mm ø spigots*	Tension Crack	22.93	46.07	28.08	0.53
Ansys 1**	Unreinforced	Failure at spigot	30	55	30	0.50
Ansys 2**	4 no. 25 mm ø spigots	Failure at spigot	30	32	16	0.93
Ansys 3**	4 no. 38 mm ø spigots	Failure at spigot	30	31	15	1.00
Ansys 4**	8 no. 25 mm ø spigots	Failure at spigot	30	25	13	1.15

*Prestressed **Approximate Values

As predicted in the numerical analysis, the tests carried out on the reinforced beams in this study showed an increase in performance in terms of stiffness and ultimate strength. However, the FE model shows much greater performance for the reinforced beam due to the fact that slippage of the clamps was not taken into account. All of the reinforced beams failed either by lateral buckling or rupture around a spigot. As demonstrated above, compression forces are generated in front of the spigot and tension forces are behind the spigot. Therefore, there is a plane generated between these stress and a rupture generally occurs in the form of a tension crack between the forces (see Fig. 14 and Fig. 15). In Fig. 14, the failure that occurred used a 38 mm ø spigot is shown. Fig. 15 shows the failure around a 25 mm ø spigot. In both instances the crack formed in the zone between the compression and tension stresses. However, the rupture was more destructive for the 25 mm ø spigot. The other type of failure that occurred was due to lateral buckling. There were no restraints positioned along the sides of the beam to resist lateral buckling and several the beams failed under this condition (see Table 2 for further details).

Figure 14: Tension crack around 38 mm ø spigot

Figure 15: Tension crack around 25 mm ø spigot

To confirm the mechanics of the reinforced beam, strain gauges were fixed to the centre of the beams on the top and bottom edges. The graph in Fig. 16 shows strains for two reinforced beams and one unreinforced beam. It can be seen from the graph that failure of the reinforced beams occurs at a similar strain in tension as the strain in the unreinforced beam. However, the apparent value of the elastic modulus is higher in the reinforced beams and a higher ultimate strength is reached. It can be also seen that one of the reinforced beams underwent large plastic deformations in compression before failure.

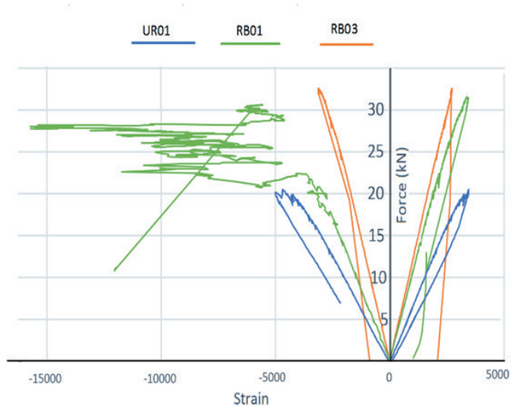

Figure 16: Compression and tension strains in the reinforced beam

Strain gauges were also positioned in front and behind the spigots. Fig. 17 shows these strains for two spigots from beam RB01. These gauges show that high strains were generated at the spigot locations. The strains generated at the centre spigot were much larger than the strain generated at the spigot towards the end of the beam.

As predicted, plastic deformation at the spigot occurs when the beam is loaded just above 15 kN. The spigot towards the centre experienced the greatest strain and this was where failure occurred. Post failure, the sections that where in compression reverted into tension.

From the FE model, it is predicted that by increasing the number of spigots the stress at each spigot is reduced. However, in the experimental tests, no increase in stiffness or ultimate strength was recorded by increasing the number of spigots. Further research is required to establish the effect of increasing the number of spigots. The reinforcement system was further developed by inducing a pre-stress into the timber prior to loading. However, it showed to be ineffective for this type of system.

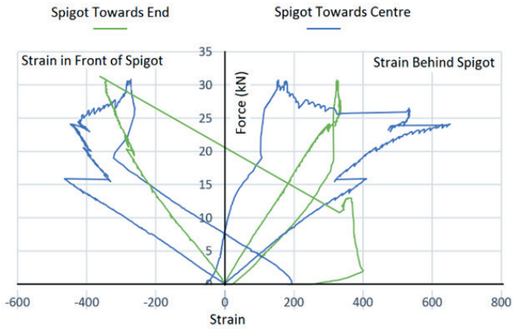

Figure 17: Compression and tension strains around spigots

6. Conclusions

From the various investigations and considerations carried out in this study, an alternative strengthening technique has been developed for use in historic structures. The reinforcement system proposed is of particular interest for conservation works as there is no requirement for adhesives and it is also fully reversible. The other main advantage is that continuous contact with the beam is not required and, therefore, if there are any fixtures or obstacles along the length of the beam the reinforcement system can still be easily installed. In addition, this reinforcement system would be aesthetically pleasing compared to other reinforcement systems currently used.

From the numerical and experimental analysis, it was found that the performance of the reinforcing system was comparable to other strengthening techniques currently used but, as highlighted above, it has its own advantages. Using the reinforcement system, the load bearing capacity of a softwood timber beam could be increased or the deflection could be reduced.

However, it was found during the investigation that inducing a prestress was not beneficial but the method of inducing the prestress could be used for jacking timber beams that have sagged over time. The steel cables can hold the beams in the jacked position once the steel cables are tightened and clamped to the spigots.

Although an increase in performance was observed, it was found in the research that creep effects can occur where large stresses are present in timber (Davies and Fraigiacomo, 2008). Therefore, the effects of creep regarding the long-term use of this reinforcement would need further investigation.

Different spigot configurations were investigated in order to reduce the stress concentration at the spigot locations. The size and number of spigots had an impact on the numerical model regarding the stiffness and strength. However, no discernible difference was noted in the experimental analysis. One possible reason for this could be due to slippage of the clamps. Accurately measuring the force at the clamps and the tension in the cables during loading should allow for greater understanding of the mechanics of the system. Further investigation in this area is recommended. Additionally, it is recommended to use a stronger clamping method for the cables to the spigots.

The typical failure mode of the reinforced beams where the ultimate strength was reached occurred at the spigot locations. A tension crack occurred between the compression and tension stresses generated around the spigot. Therefore, reinforcing around the spigot may further increase the load capacity.

From this study, the proposed reinforcement has proven to be effective.

Acknowledgements

The authors gratefully acknowledge the support of the Department of Civil, Structural and Environmental Engineering at Trinity College Dublin and the support of the Infrastructure Division of Atkins Consulting Engineers.

References

Arya, C., 2009. Design of structural elements: Concrete, steelwork, masonry and timber designs to British standards and Eurocodes. CRC Press.

Borri, A. and M. Corradi (2011). “Strengthening of timber beams with high strength steel cords.” Composites Part B: Engineering 42(6): 1480-1491.

Brunner, M. and M. Schnueriger (2004). Timber beams strengthened with prestressed fibres: Delamination. Proceedings of the 8th world conference on timber engineering, Citeseer.

Brunner, M. and M. Schnueriger (2005). Timber beams strengthened by attaching prestressed carbon FRP laminates with a gradiented anchoring device. Proceedings of the international symposium on bond behaviour of FRP in structures (BBFS 2005).

Corradi, M., et al. (2016). “Fully reversible reinforcement of softwood beams with unbonded composite plates.” Composite Structures 149: 54-68.

Davies, M. and M. Fragiacomo (2008). “Long term behaviour of Laminated Veneer Lumber members prestressed with unbonded tendons.”

de la Rosa Garcia, P., et al. (2013). “Bending reinforcement of timber beams with composite carbon fibre and basalt fibre materials.” Composites Part B: Engineering 55: 528-536.

Fastenal. 2017. Torque Values for A2 or A4 Metric Stainless Steel Fasteners. [ONLINE] Available at: https://www.fastenal.com/content/feds/pdf/Torque%20of%20Metric%20Stainless%20Steel.pdf. [Accessed 14 June 2017].

Feilden, B. (2007). Conservation of historic buildings, Routledge.

Jasieńko, J. and T. P. Nowak (2014). “Solid timber beams strengthened with steel plates–Experimental studies.” Construction and Building Materials 63: 81-88.

John, H.P., John H Pless and John H Stubber, 1963. Seasoning timber. U.S. Patent 3,083,470.

Khelifa, M. and A. Celzard (2014). “Numerical analysis of flexural strengthening of timber beams reinforced with CFRP strips.” Composite Structures 111: 393-400.

Miele, C. ed., 2005. From William Morris: Building Conservation and the Arts and Crafts Cult of Authenticity, 1877-1939 (p. 354). New Haven, CT: Yale University Press.

Nowak, T. P., et al. (2013). “Experimental tests and numerical analysis of historic bent timber elements reinforced with CFRP strips.” Construction and Building Materials 40: 197-206.

Thelandersson, S. and H. J. Larsen (2003). Timber engineering, John Wiley & Sons.

Excavation and Lateral Support - “Caterpillar” Scheme for South Cut-and-Cover Tunnel in Tuen Mun - Chek Lap Kok Link Northern Connection Sub-Sea Tunnel Section

Tiffany Chan

Associate Director
Engineering, Design and Project Management
Hong Kong, China

Thomas Choi

Technical Director
Engineering, Design and Project Management
Hong Kong, China

Abstract

This paper presents the innovative design of the world’s first 15-cell caterpillar-shaped cofferdam developed for the deep excavation and lateral support works in a reclaimed site. The design and construction of which has successfully overcome the challenges of adverse geology and tight programs, whilst also reducing construction risks and costs.

The key scope of this project is to construct a 630 m long and maximum 33 m wide cut-and-cover Tunnel (SCC) and Approach Ramp (SAR) at the southern landfall of the Tuen Mun - Chek Lap Kok Link Northern Connection Sub-Sea Tunnel Section (TM-CLKL) site, which is a newly reclaimed land with more than 20 m thick marine deposit/alluvium. The maximum excavation depth is around 43 m. Instead of the conventional excavation and lateral support scheme with straight diaphragm walls and steel struts, an innovative idea was developed to utilize the 500 m long caterpillar-shaped cofferdam with 15 cells, each of which formed by perimeter diaphragm wall panels installed in an arc shape and laterally supported by reinforced concrete struts at the locations of specially designed Y-panels.

This paper is prepared to discuss the technical considerations and challenges in both design and construction associated with the Caterpillar scheme and its benefits as compared with the conventional scheme with straight diaphragm walls.

Keywords

Caterpillar Cofferdam; Deep Excavation and Lateral Support; Soft Ground

Winner of the International Tunneling and Underground Space Association (ITA)- Major Project of the Year with a budget of more than €500 million.
Recipient of the Innovation in Design & Delivery category award at the New Civil Engineer Tunneling Festival 2019.

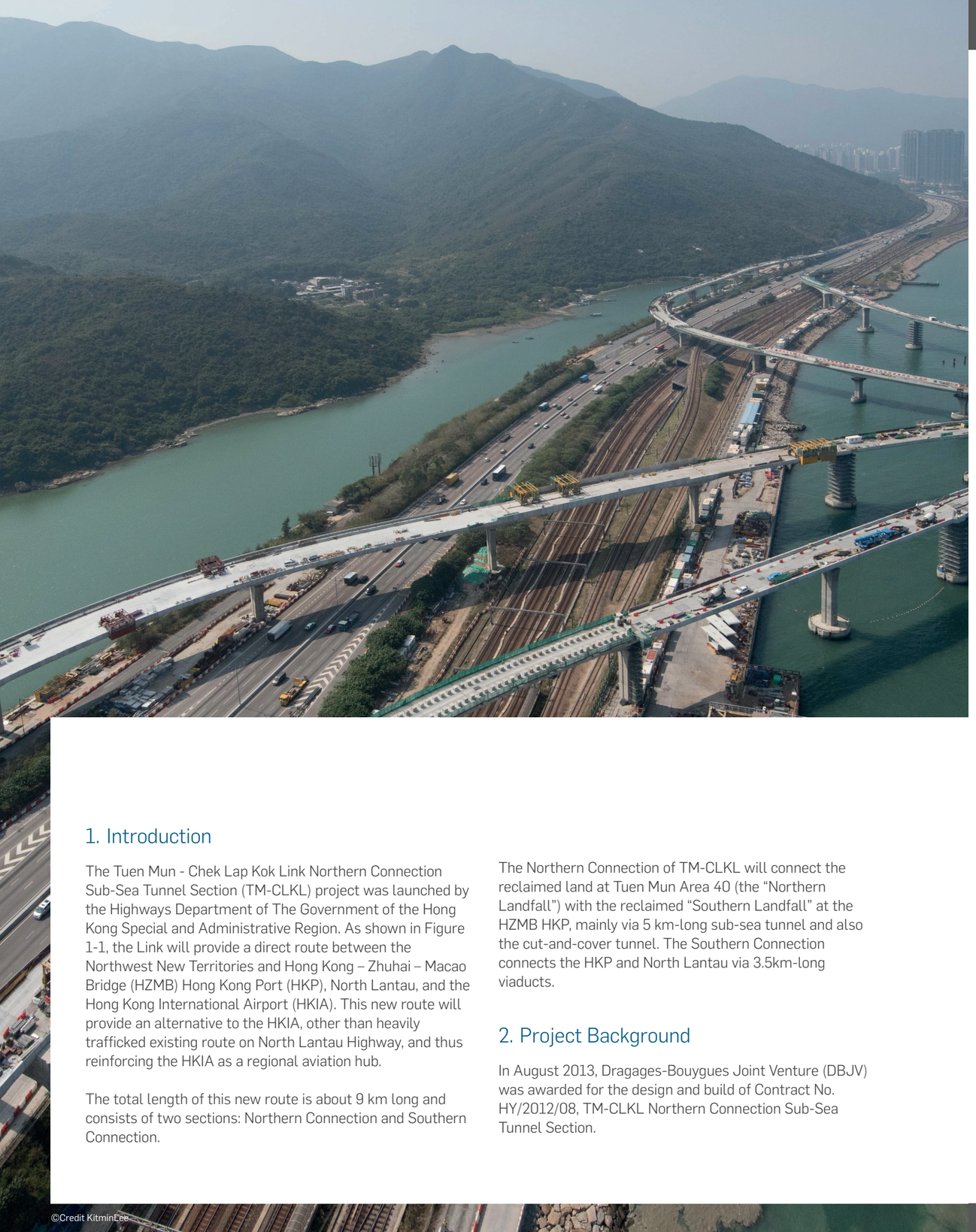

©Credit KitminLee

1. Introduction

The Tuen Mun - Chek Lap Kok Link Northern Connection Sub-Sea Tunnel Section (TM-CLKL) project was launched by the Highways Department of The Government of the Hong Kong Special and Administrative Region. As shown in Figure 1-1, the Link will provide a direct route between the Northwest New Territories and Hong Kong – Zhuhai – Macao Bridge (HZMB) Hong Kong Port (HKP), North Lantau, and the Hong Kong International Airport (HKIA). This new route will provide an alternative to the HKIA, other than heavily trafficked existing route on North Lantau Highway, and thus reinforcing the HKIA as a regional aviation hub.

The total length of this new route is about 9 km long and consists of two sections: Northern Connection and Southern Connection.

The Northern Connection of TM-CLKL will connect the reclaimed land at Tuen Mun Area 40 (the "Northern Landfall") with the reclaimed "Southern Landfall" at the HZMB HKP, mainly via 5 km-long sub-sea tunnel and also the cut-and-cover tunnel. The Southern Connection connects the HKP and North Lantau via 3.5km-long viaducts.

2. Project Background

In August 2013, Dragages-Bouygues Joint Venture (DBJV) was awarded for the design and build of Contract No. HY/2012/08, TM-CLKL Northern Connection Sub-Sea Tunnel Section.

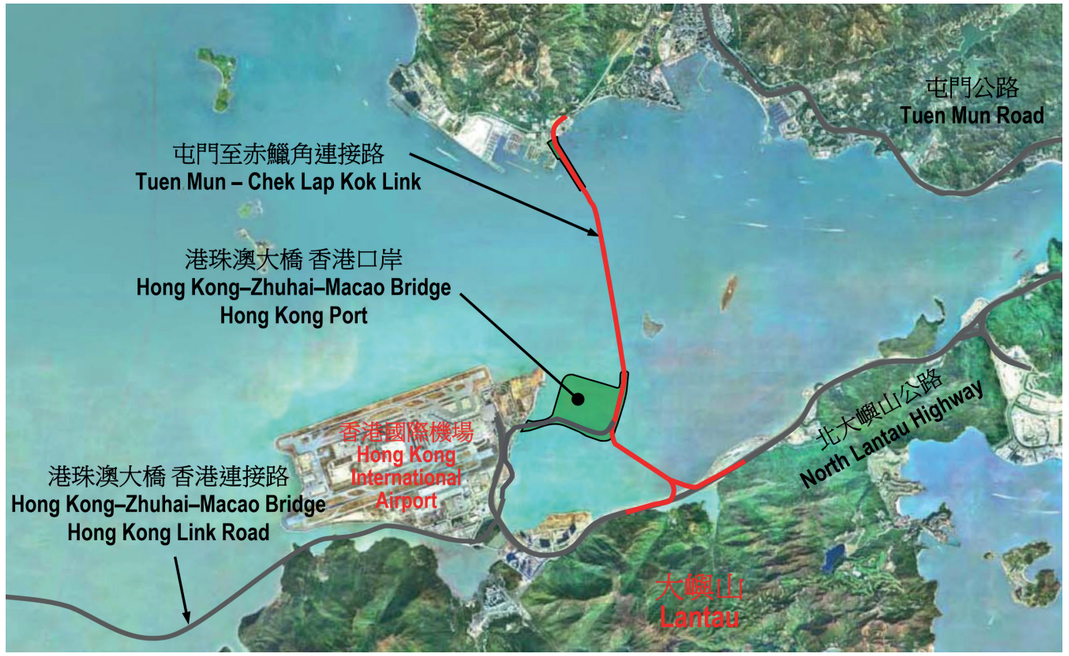

Figure 1-1: Tuen Mun – Chek Lap Kok Link project plan

The major works under this contract, which is valued at approximately HKD18.2 billion, include:

- Reclamation of approximately 16.5 hectares at Tuen Mun Area 40 as the Northern Landfall of the sub-sea tunnel;
- Dual two-lane sub-sea tunnel (two tubes) of approximately 5 km long between the Northern Landfall and Southern Landfall, excavated using three slurry-shield Tunnel Boring Machines (TBMs). One of which is the world's largest with 17.63 m excavation diameter, and the other two are identical with an excavation diameter of 14.00 m; and
- Ventilation shafts and buildings, cut-and-cover tunnels, and approach ramps at both the Northern Landfall and the Southern Landfall.

Atkins was appointed by DBJV for the following roles and scopes:

- Contractor's Designer for the Permanent (including tunnel structures and its space-proofing, roadworks and drainage) and Temporary (mainly the excavation and lateral support) Works for the Southern Landfall Approach Ramp (SAR) and Cut-&-Cover (SCC) Tunnel, with a total length of about 630 m. The permanent two-cell tunnel box (refer to Figure 2-1) is maximum 33 m wide and generally 14 m high and requires maximum 43 m deep excavation within the newly reclaimed land; and

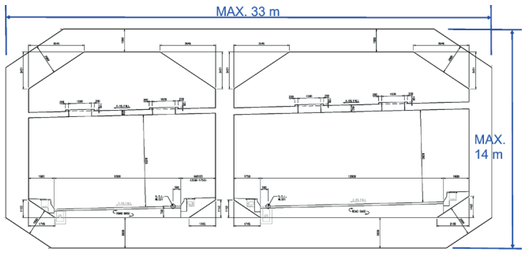

Figure 2-1: South cut-and-cover tunnel box structure

- Independent Design Checker (IDC) for the other major works (TBMs, ventilation shafts, and buildings, etc).

This paper will focus on the Temporary Works for the excavation and construction of SCC Tunnel.

3. High Demand for Innovative Scheme

3.1 Difficulty in Site Geology

The proposed SCC Tunnel is located at the newly reclaimed area at the HZMB HKP. The geological sequence comprises reclamation fill (~15 m thick), marine deposit (~10 m to 15 m thick), then alluvium (~20 m to 30 m thick), and in turn completely to highly decomposed granite, meta-siltstone or meta-sandstone (with varying thickness) before reaching engineering rockhead. The excavation is a maximum of 43 m deep and, based on the geotechnical interpretation, it will encounter soft clay layers (marine clay and alluvial clay) of around 30 m thick. Figure 3-1 shows the geological profile along the SCC Tunnel.

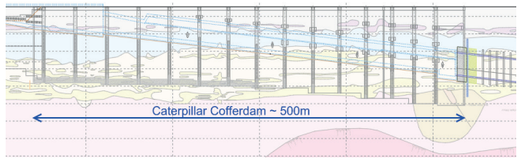

Figure 3-1: Geological profile along south cut-and-cover tunnel

The site's geology, which is particularly variable in nature for the Alluvium regarding the continuity of alluvial sand layers, together with the due consideration of the potential impacts on the nearby sensitive receivers, impose more difficulties and risks for the conventional scheme with straight diaphragm wall (D-wall) and steel struts to work within the project time frame and budget.

3.2 Caterpillar Scheme vs Conventional Scheme

An initial scheme utilizing the conventional straight D-wall was studied (Figure 3-2).

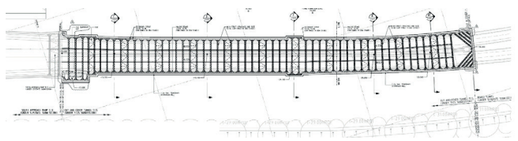

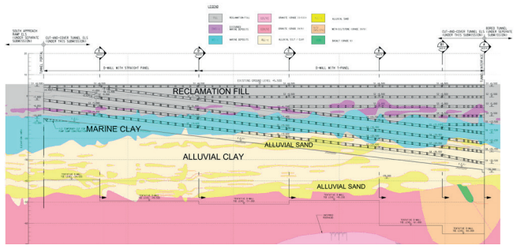

Figure 3-2: Conventional ELS scheme (plan and longitudinal section) with straight D-wall and steel struts

Up to 9 layers closely-spaced (approximately 4 m vertically and minimum 6 m horizontally) strutting with large steel members are required. Moreover, it would need extensive ground strengthening works below/near the excavation level to strut the D-wall since the untreated soft ground layers could not provide sufficient lateral stiffness for the D-wall.

In addition, two TBMs of 14 m diameter have to breakthrough at the northern end of the cofferdam. The space would be extremely tight for the cofferdam with such close strut spacings.

Also, the risk level of the conventional scheme for deep excavation in soft clay must not be overlooked. Taking into account some past failure incidents, the designer has seriously considered the risk particularly for the uncertainty on the strut design. For instance, strut/waler connection is designed as "pinned" but is rigidly connected on site. The rigidity could induce additional bending on the strut when the wall bends.

The idea of 15-cell Caterpillar cofferdam (Figure 3-3) counts on the D-wall panels in an arc shape and eliminates the closely spaced steel struts. Instead, reinforced concrete struts with average vertical spacing of 8 m and minimum horizontal spacing of 25.5 m were used (refer to Section 4 for more detail). The idea was developed and finally implemented with the following proven advantages over the conventional scheme:

- Site safety was greatly enhanced with no propping works at height and no heavy strut liftings for installation and removal. Risk of site congestion due to strutting was eliminated and excavation plants were able to work in an unrestricted condition.
- The elimination of congested steel struts allows fast-track of all related activities, including excavation, TBMs retrieval and construction of the tunnel box structures (Figure 3-4). The RC struts for the Caterpillar are arranged to provide clear headroom of 16.5 m above the formation level which allows using travelling formworks for the permanent structures. Re-propping, during the permanent tunnel structures construction if using steel struts, was not required. 6 to 10 months savings were forecasted compared to the conventional scheme.
- Due to the geometric nature of the perimeter arc, destabilizing pressure at the D-wall toe from the retained side shall be resisted by using a hoop action among the arc D-walls. The pressure will then be eventually transferred to the Y-panels and cross walls. Hence, toe stability against kick-out failure shall not be a concern. The Caterpillar D-wall embedment depth could then be reduced as compared with the conventional scheme, although the perimeter arc D-wall shall also be sufficiently embedded into the ground to ensure stability against other failures like base heave, piping and hydraulic uplift.

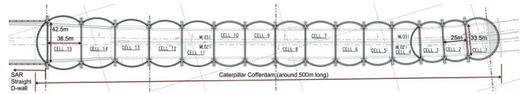

Figure 3-3: Caterpillar scheme cofferdam

Figure 3-4: Clear space below the lowest strut for tunnel box construction

4. General Arrangement of the Caterpillar

4.1 Key Elements and Load Path

The typical arrangement of the Caterpillar cofferdam and the load transfer are shown in Figure 4-1. The Caterpillar consists of 15 cells, each of which is formed by perimeter D-wall (1.2 m or 1.5 m thick) panels arranged in an arc shape, which will resist lateral pressures mainly by means of hoop force. The longitudinal span of the cells varies from 25 m to 36.5 m and the radius of curvature of the arc D-wall varies from 22 m to 28.5 m.

At the interface between cells, the hoop forces induced on the perimeter arc D-walls will be transferred to the Y-panels (refer to Figure 4-2 for its geometry) which are hammer-shaped with overall 6.5 m length and maximum 3.6 m width. These are constructed by 5-bite D-wall trench excavation (more details in Section 5.3).

The Y-panels are laterally supported by the reinforced concrete struts vertically spaced at around 8 m to 11 m centre-to-centre, with a maximum of 3 layers at the deepest excavation and a single layer at the shallower section. The RC struts are typically 2 m wide by 2 m deep but some lower struts are 3.2 m wide by 2.8 m deep. The bottom corners of the lower struts are chamfered to reduce the Y-panel bending moment. At the strut connection with Y-panel, "wing corbel" (Figure 4-3) is proposed for strengthening.

Cross walls, in the form of continuous D-wall panels (1.2 m or 1.5 m thick), laterally support the Y-panels below the final excavation level. Above the cross wall panels cut-off level, the excavated trenches were backfilled with lean concrete to provide pre-support to the Y-panels before the RC strut installation so that the Y-panels bending moment could be reduced.

A capping beam, which is generally 2 m wide by 2 m deep and widened at the location of Y-panel, is provided on top of the perimeter arc D-walls and Y-panels to enhance the cofferdam integrity. Figure 4-4 shows the typical ELS section at the Y-panel location.

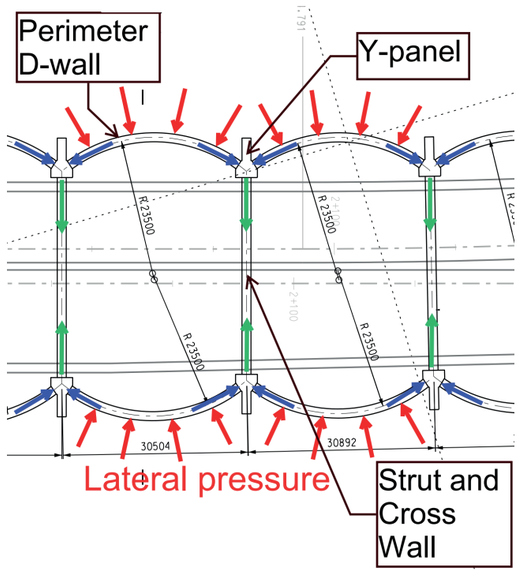

Figure 4-1: Typical arrangement of Caterpillar cells and load transfer

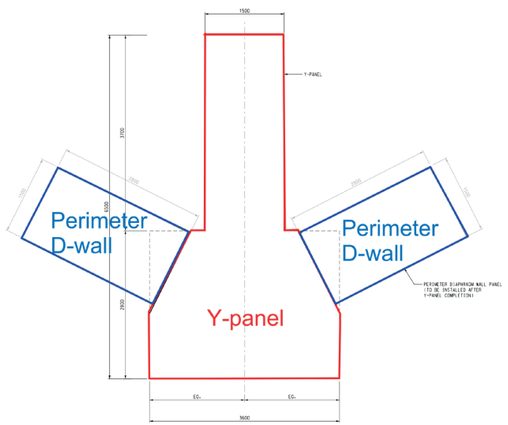

Figure 4-2: Y-panel geometry

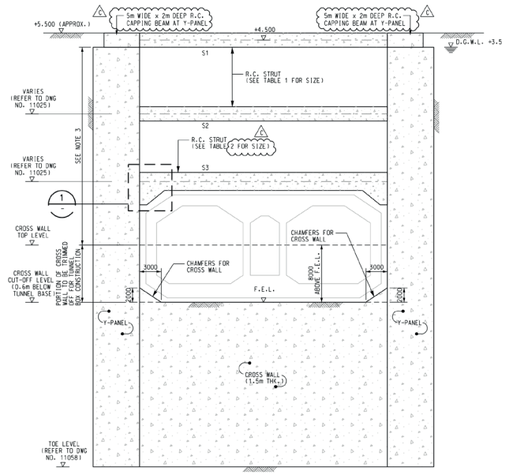

Figure 4-4: Typical ELS cross section showing lateral support

Figure 4-3: Wing corbel for strut

5. Technical Considerations and Challenges

Axisymmetric analyses using the computer programme PLAXIS 2D (Figure 5-1), which takes into account the soil-structure interaction, are performed to evaluate the lateral earth pressures, water pressures and ground spring stiffness, which are then input to the structural analysis models. Seepage analyses and staged excavations are considered in PLAXIS' axisymmetric analyses to calculate the lateral earth pressures and pore water distribution inside and outside the excavation as a result of pumping dewatering below the excavation. The PLAXIS analyses are conducted for each Caterpillar cell with different excavation depths and geological profiles.

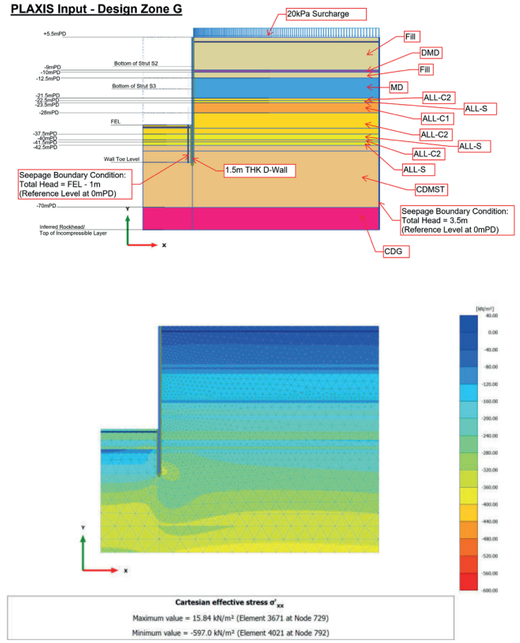

Figure 5-1: PLAXIS axisymmetric analyses

3-dimensional analyses are then performed using the computer programme SAP2000 for the structural analyses of the Caterpillar cofferdam. The SAP2000 analyses account for the 3-dimensional geometry of the Caterpillar cells, including the D-wall openings at the TBM breakthrough and the strengthening tympanum. The perimeter arc D-wall, cross walls, struts and Y-panels are represented by a series of thin-shell elements. The ground medium surrounding the perimeter D-wall is represented by a series of area springs perpendicular to the shells. In case of tension, the ground springs are ignored and no reaction is given to the D-wall.

Considering the total length of around 500 m for the 15-cell Caterpillar cofferdam, its structural analyses were split into three models, each of which were assigned with the appropriate boundary restraints. Figure 5-2 shows one of the structural models.

Whilst the above paragraphs outline the general design and analytical approach, the following sub-sections highlight some specific considerations and challenges in terms of both design and construction of the Caterpillar.

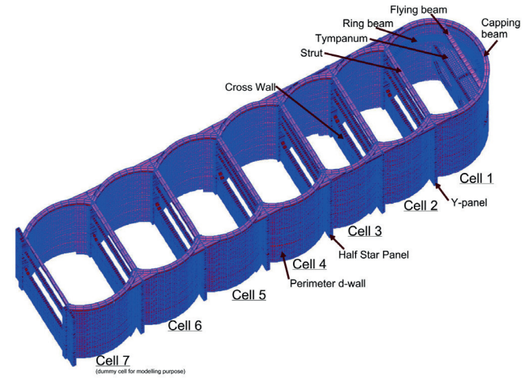

Figure 5-2: SAP2000 structural model

5.1 Longitudinal Stability

An arch structure primarily counts on the lateral restraint at its support. Hence, at the early design development stage, it was realized that longitudinal stability would be crucial for the Caterpillar cofferdam as its principle counts on the arching effect to resist the lateral loads. To achieve this objective, the arc radius and longitudinal span of each cell had to be calculated in relation with its adjacent cells. From the Contractor's point of view, it would be preferable to have a larger radius and span. In principle, the shallower the excavation, the larger cell radius and span could be so that there would be less excavation volume and fewer cross walls/Y-panels. However, as the Designer, we had to optimize these geometric parameters in parallel with the consideration of the structural capacities of Y-panels and cross walls, as well as minimize the unbalanced load in the longitudinal direction between adjacent cells (Figure 5-3).

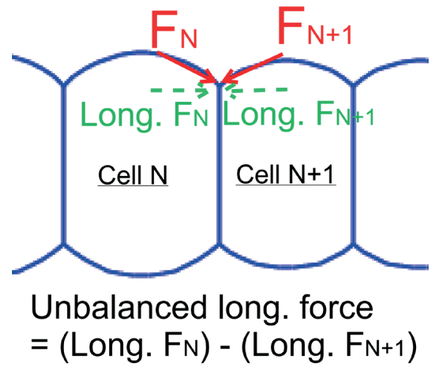

Figure 5-3: Unbalanced longitudinal load

With the principles outlined above, the radius and span were initially worked out using preliminary calculations that aimed to minimize the unbalanced longitudinal load between adjacent cells. The longitudinal movement/ behavior of the schematic layout was then checked using a 2-dimensional SAP2000 analysis. Several iterations were conducted before the final scheme could be frozen for proceeding to the 3-dimensional SAP2000 analysis for the detailed design.

Other than the geometry of the cell radius and span, the differential excavation level between adjacent cells was limited to a maximum of 3 m to minimize the unbalanced load. This imposed a key constraint for the construction program and led to the need and implementation of phased excavation elaborated in Section 5.4 below.

Another key issue concerning the longitudinal stability is the interface with the SAR straight D-wall cofferdam. Cell 15 at the southern end of the Caterpillar cofferdam was connected to the SAR cofferdam (Figure 5-4) which is supported by straight D-walls and steel struts. To evaluate the longitudinal restraint given to the Caterpillar by the SAR cofferdam, a 3-dimensional PLAXIS analysis (Figure 5-4) was performed and the corresponding lateral stiffness was input to the structural SAP2000 analysis.

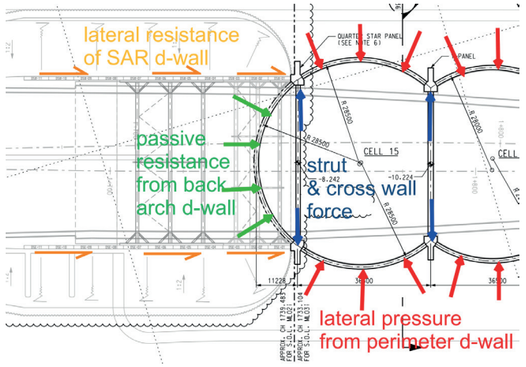

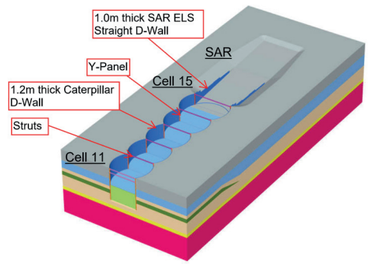

Figure 5-4: PLAXIS analysis for Caterpillar / SAR cofferdam interaction

The quarter-star panels (Figure 5-5), function similar to the Y-panel and were designed with specific geometry to allow a connection with the Cell 15 perimeter and back-arch D-walls, cross walls and SAR straight -walls. Due considerations have been made when developing its geometry, particularly in relation to the cell radius and allowance for construction tolerance (D-wall panel offset and verticality). Design-wise, the torsion induced on the quarter-star panels was one of the major concern.

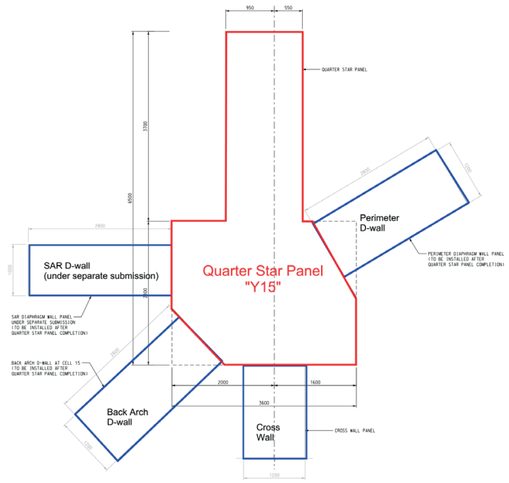

Figure 5-5: Quarter-star panel

5.2 D-Wall Panel Joint in Structural Modelling and Design

The Caterpillar cofferdam primarily consists of D-wall panels. Therefore, it is not possible to have rebar continuity across the panel joints. When subject to the combined effects of hoop (i.e. horizontal) axial force and bending moment, these joints could only action in compression but not tension. Tension cut-off (i.e. no tensile stress) was assigned to the D-wall elements in the SAP2000 structural analysis to mimic this behavior.

The perimeter D-wall structural capacity subject to the hoop forces is checked using the moment-axial force (M-N) interaction diagram with the assumption that plain concrete accounts for the rebar discontinuity at the panel joints. In the M-N interaction diagram, the governing parameters for the structural capacity are the D-wall concrete grade and thickness. For the latter, reduced contact thickness at the D-wall panel joints that resulted from the verticality tolerance was duly considered.

In view of the above design considerations, the verticality control on site is more stringent as compared with a conventional straight D-wall. Generally, maximum 1:200 verticality is specified, whilst for some other panels with less design margin, maximum 100 mm relative dislocation between adjacent panels is required. And for Y-panels, which are the key structural elements of the Caterpillar scheme, the maximum verticality is 1:400.

5.3 Y-Panels

The Y-panels are key structural elements in the Caterpillar scheme as all the perimeter D-walls transfer the loadings to them.

For the ease of permanent tunnel structure construction, the levels of the lowest struts were arranged to provide the required clear headroom (around 16.5 m) without any obstacles. The Y-panel cross-section had to be sufficiently large to limit the ultimate shear stress (corresponding to maximum factored shear force of around 73,000 kN) in accordance with the design standard. The wide front end (3.6 m) provided much more space for the main bars on the excavation face and allowed for sufficient rebar to take the extreme bending moments (maximum factored 310,000 kNm). Other than the concern on the structural capacity, the Y-panel geometry had to suit different various cell radii and spans, as well as the trench excavation methodology.

Subject to the point of action from the perimeter D-walls (similar to a bottom-loaded beam), tension tie bars were required, which made the Y-panels more congested with the rebars already required for bending and shear (refer to Figure 5-6 for the heavily reinforced Y-panel cross section). The extremely heavy rebar cage (maximum 135 tons) imposed difficulty for the steel fixing as well as lifting operation on site. Combination of prefabricated rebar cages and in-situ fixed cages were used for one single Y-panel. Large cranes up to 400-ton capacity and up to triple lifts were utilized for cage lifting (Figure 5-7). In terms of rebar detailing, the reinforcement arrangement had to allow for other D-wall installation provisions like grout tubes, sonic tubes and D-wall stop-ends. Therefore, there was high demand for the rebar optimization.

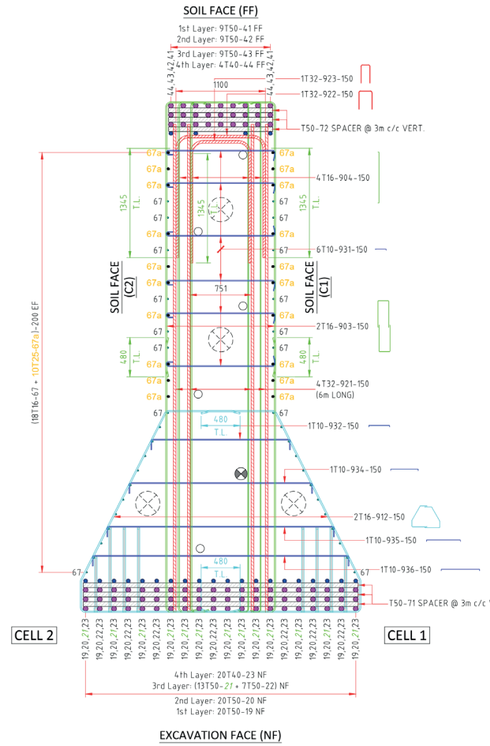

Figure 5-6: Y-panel cross section

Figure 5-7: Y-panel rebar cage lifting operation

In order to excavate a trench that is 6.5 m long, 3.6 m wide at its base, and 55.5 m deep for the deepest Y-panel, a 5-bite excavation solution (Figure 5-8) was implemented. There was no previous experience in the world for such a trench (15.6 m^2 cross sectional area and 860 m^3 volume). Cement-soil mixing (CSM) was adopted around the excavation perimeter as ground strengthening works (Figure 5-8), in addition to the bentonite slurry within the trench excavation. A 3-dimensional PLAXIS analysis (Figure 5-9) was performed to evaluate the trench stability. Trial panels were conducted on site, together with instrumentation (ground settlement markers and inclinometers) and monitoring, to verify the trench stability for Y-panel excavation with CSM before full implementation of the ground strengthening works.

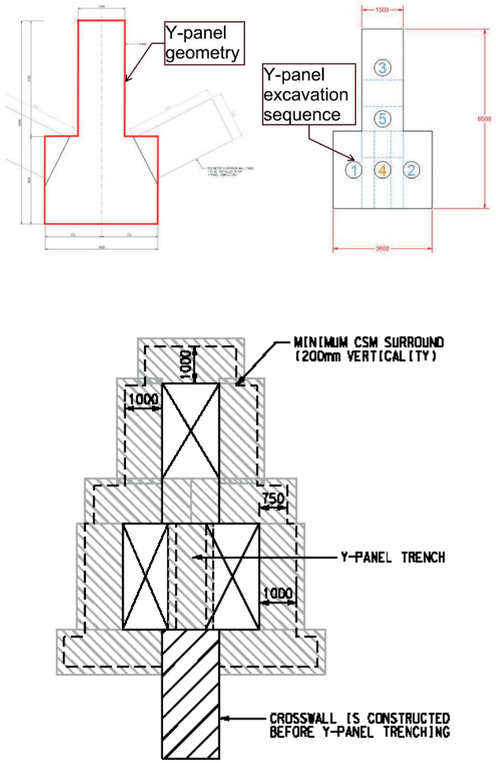

Figure 5-8: 5-bite trench excavation for Y-panel

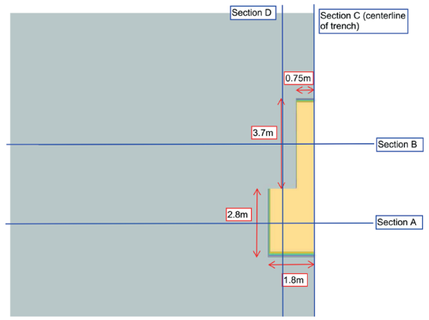

Sections of Y-Panel Trench (Plan View)

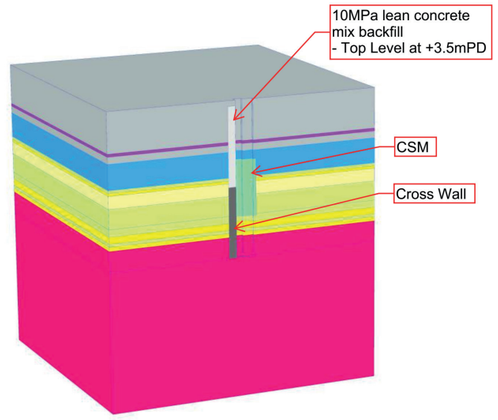

Figure 5-9: 3-D PLAXIS analysis for Y-panel trench stability

5.4 Construction Program

TBM breakthrough at Cell 1 was in the critical path and this cell had to reach the final excavation level as soon as possible. However, as mentioned in Section 5.1, the maximum differential excavation between adjacent cells should be a maximum of 3 m. Given the average excavation depth at Cell 1 is about 41 m, Cell 14 excavation had to start for Cell 1 before it reached the bottom. To delink this constraint, a phased excavation sequence was implemented.

To achieve this, back-arch D-walls were introduced at Cell 3 so a closed shaft in peanut shape was formed with Cells 1 to 3. This is referred to as Phase 1 excavation (Figure 5-10), which could start even the advance works (e.g. D-wall installation, construction of capping beam and first layer of RC strut, pumping test) for Phase 2 excavation in Cells 4 to 15 were not completed. During the Phase 2 excavation (Figure 5-11), the back-arch D-walls at Cell 3 were trimmed off following the excavation within Cell 4 until it reached the final excavation level.

Figure 5-10: Caterpillar Phase 1 excavation

Figure 5-11: Caterpillar Phase 2 excavation

To allow for the two-phased excavation, half-star panels with specific geometry (which is modified from the typical Y-panel and function similarly as Y-panel; refer to Figure 5-12) were developed and adopted in Cell 3. The half-star panel geometry allowed its connection with Cells 3 and 4 perimeter D-walls, Cell 3 back-arch D-walls and cross walls. And similar to the quarter-star panel in Cell 15, due consideration has been allowed for the construction tolerance and the cell radius when developing the half-star panel geometry.

5.5 TBM Breakthrough

Two TBM breakthrough were located at Cell 1. The D-wall panels within the breakthrough zone were reinforced with glass fibre reinforced polymer (GFRP). The maximum breakthrough load is around 81,000 kN. A massive reinforced concrete structure, called tympanum (Figure 5-13), was designed for strengthening the Cofferdam. The tympanum is 21.5 m high and reinforced with steel rebars except within the breakthrough zone. The front faces of the breakthrough zone were reinforced by GFRP before the complete breakthrough.

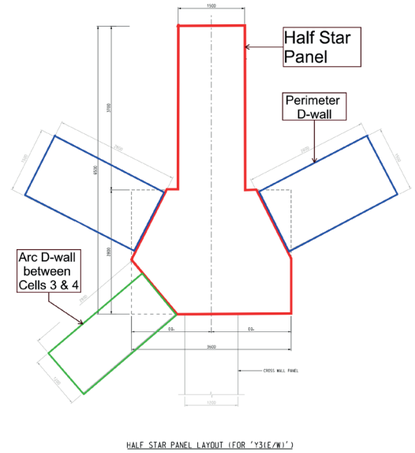

Figure 5-12: Half-star panel

Figure 5-13a: Tympanum (before breakthrough)

Figure 5-13b: Tympanum (after breakthrough)

References

- Kjell Karlsrud and Lars Andresen. “Design and Performance of Deep Excavations in Soft Clays.”
- J. N. Shirlaw, T. S. Tan, K. S. Wong. ‘Deep Excavations in Singapore Marine Clay’.
- ACI 440.1R-06 – Guide for the Design and Construction of Concrete Reinforced with FRP Bars.
- Hong Kong Building (Construction) Regulations (1990).
- Buildings Department, HKSAR. Code of Practice for Foundations 2004.
- Buildings Department, HKSAR. Code of Practice for Structural Use of Concrete 2013.
- Buildings Department, HKSAR. Code of Practice for Dead and Imposed Load 2011.
- Buildings Department, HKSAR. Code of Practice for Precast Concrete Construction 2003.
- Geotechnical Engineering Office, Civil Engineering and Development Department, HKSAR. GCO Publication No. 1/90 - Review of Design Methods for Excavations.
- CIRIA Report 113 ‘Control of Groundwater for Temporary Works’
- CIRIA Report 515 ‘Groundwater Control Design and Practice’
- Civil Engineering and Development Department, HKSAR. GEOGUIDE 1, Edition 2 (1993) - Guide to Retaining Wall Design.
- Geotechnical Engineering Office, Civil Engineering and Development Department, HKSAR. GEO Publication No. 1/2006 - Foundation Design and Construction.
- Highways Department, The Government of the Hong Kong Special Administrative Region. Layout Plan of Tuen Mun – Chek Lap Kok Link (TM-CLKL). 2013.

Road Tunnel Safety Levels and Minimum Operating Requirements

Gary Clark

Chief Engineer, Tunnel Ventilation and Fire Life Safety
Engineering, Design and Project Management
Epsom, UK

Christian Perez

Senior Tunnel Ventilation Engineer, Tunnel Ventilation and Fire Life Safety
Engineering, Design and Project Management
Epsom, UK

Yenny Gomez

Senior Mechanical Engineer, Tunnel Ventilation and Fire Life Safety
Engineering, Design and Project Management
Epsom, UK

Abstract

A concept and process for the definition of minimum operating requirements (MORs) is presented, following the key principles that the MOR is applied to the Safety Functions, rather than to specific items of equipment or systems, and the MOR is considered to reflect the minimum level of safety accepted by tunnel users so if the tunnel is below its MOR then it should not normally be open to traffic, without mitigations.

Little guidance exists for the derivation of MORs. The process is complex because of the scale of systems and procedures required for the safe operation of road tunnels and the inter-dependency between those systems and procedures. When a piece of equipment, a system, procedure or other element of the tunnel operating condition fails or degrades, the impact on safety is not always clear and judgement is often required, resulting in the potential for uncertain or inconsistent outcomes.

Discussion is presented on the current tunnel safety landscape to provide context for the discussion of the benefits and principles of MORs. A practical example of MOR application is presented, showing how compensatory measures may be deployed to enable continued safe operation of a tunnel with degraded systems.

Keywords

Minimum Operating Requirements; Road Tunnel Safety; ALARP; Safety Functions

1. Introduction

The focus of this paper is on tunnel safety with regards emergency incidents. In particular, considering major incidents such as fire, where the enclosed nature of a tunnel can lead to greater consequences than incidents on the open road, and where there is a focus for tunnel designers, operators and owners. A severe vehicle fire in a road tunnel has the potential to cause significant human impact, including loss of life.

1.1 Factors Affecting Occurrence of Incidents

Most vehicle fires are caused by vehicle defects, rather than road traffic collisions (UK statistics (1)). Management of the likelihood of such defects are, mostly, not within the control of the tunnel designer or operator. The focus of the designer and operator is therefore on the control they can have on the factors that influence the development of an incident, and its consequences: the 'Technical Factors'.

At the design stage, safety objectives typically include the management of major fire incidents to control the effects and ensure the safety of tunnel users. A major vehicle fire that results in injuries and/or fatalities may therefore represent a failure in these objectives, for whatever reason. It is incumbent on those responsible for tunnel safety to scrutinise the potential for such failures. This in turn requires an understanding of the mechanisms of failures, where the tunnel is not simply a collection of technological assets, it is a reflection of the overseeing organisation's definition of purpose, goals and decision criteria – and, by extension, those of the wider society. Scrutiny of potential failures must therefore be applied to the technical aspects and the non-technical aspects. Figure 1 illustrates a three-level model of incidents.

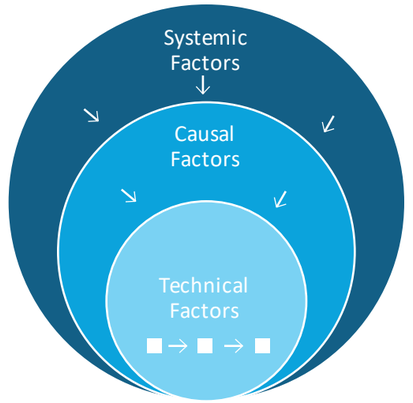

Figure 1: Factors that influence occurrence of incidents - adapted from Johnson

- The 'Technical Factors' represents the chain of events that might occur because of a failure of a technological component, a combination of such failures, or an operational/organisational action. For example, an alarm not being registered as significant in the control room leading to non-deployment of ventilation.
- The 'Causal Factors' are those that allow the events to occur. For example, a high level of false alarms during normal operations de-sensitising operations staff, a design flaw in the detection system or an unclear operating procedure.
- The 'Systemic Factors' may not be directly related to the events but are nevertheless critical in understanding the overall failure. These may be, for example, an inadequacy in design standards, pressure to keep the tunnel open under all circumstances, or pressures on maintenance budgets.

1.2 Safety Levels

Safety in road tunnels should be at a level deemed acceptable by society. There may be different means of establishing what is an acceptable design level of user safety between different jurisdictions, but all will follow similar principles. Acceptable levels of safety may be demonstrated through compliance with prescriptive standards and legislation, through risk analysis and performance-based design, or through a combination of these.

1.3 Design and Operational Intent Versus Reality

The level of operational safety in the tunnel is provided by the operation and management of the systems, equipment and facilities in the tunnel. Achieving the design intent, and therefore the associated safety levels, on a continual basis, will depend on the success of this operational management (including maintenance and renewals). This in turn is contingent on the success of:

- The implementation of the design
- The appropriateness of the design, in reality
- The operator's understanding of the design intent
- The management of change (in the tunnel situation)

Figure 2 illustrates the relationship between three models of safety.

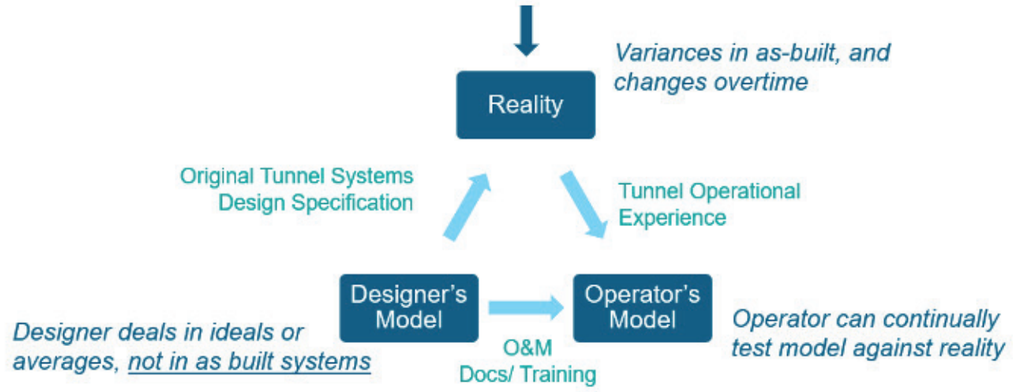

Figure 2: Relationship between models - adapted from Leveson (3)

Figure 3: Illustration of safety communication process

The design intent in most cases may be clear, as communicated through the operation and maintenance (O&M) documentation and training. In reality, the tunnel operational experience may not reflect the design intent, because of changes with time, or differences between design and as-built. In operation, the operator is able to continually test the operational model against reality. Experience may be fed back to design, to support the communication of safety, risk and the continual improvement process, as illustrated in Figure 3.

It is often the case that the communication represented by the arrows in Figure 3, in both directions, is inadequate. Limited design expertise and input may be sought at the operations stage, for managing change and ensuring safety levels are maintained. Similarly, information passed from design to operations on commissioning and handover may be inadequate for the effective and safe operation of the tunnel. This is particularly true with regards action required on degradation of systems performance in order that safety levels are maintained.

1.4 Benefits of the MOR Model

Knowledge of the impact of system, facility or operational degradation beyond the normal redundancy levels on tunnel safety, enables the management of safety both in the design stage, and in the operations stage. For example, in the early stages of design, if it is clear that system degradation beyond a certain point, in operation, will lead to tunnel closure or traffic restrictions, for overall safety reasons, then the drive for the design will be to avoid such situations by designing appropriate resilience and redundancy. In operation, clarity for the operator on actions required to offset systems degradation, will influence maintenance strategy, and operating procedures.

Appropriately designed MORs provide a means of achieving this clarity in:

- the design level of safety (i.e. the level of safety deemed acceptable by the authorities and stakeholders in the development and approval of the design), and the systems and equipment performance requirements to maintain that level of safety,
- the individual and cumulative effects of degrading systems and equipment on the level of safety, relative to the design level of safety, and
- how to offset degrading safety levels, the measures that may be deployed for this purpose, their design, and performance monitoring.

2. Design for Safety

2.1 The ‘Standards’ Approach

In many cases, the demonstration of adequate safety levels in design is achieved through the demonstration of compliance with standards. Those standards, where set by the authority having jurisdiction, may be deemed to represent an acceptable level of safety to the travelling public, and to society as a whole. Safety risk in such cases, may be deemed to be as low as reasonably practicable (ALARP). Such standards may be prescriptive, in which case, no further assessment of risk or performance may be required, but, as is often the case, standards may incorporate an element of risk-based design in the setting of design criteria and/or in the demonstration of compliance.

2.2 The ‘Risk’ Approach

In some jurisdictions, in addition to (or instead of) compliance with prescriptive requirements, the process in design for safety requires the explicit estimation of safety risk, and the evaluation of that risk against acceptance criteria. Good practice in risk assessment for road tunnels is well documented (e.g. in PIARC (4)) and typically requires scenario definition, risk estimation and risk evaluation (tolerability).

The value in explicit risk estimation is subject to the quality and the consistency in the data used in that estimation, such as traffic data, incident frequency data, probability data for incident escalation etc. Such data have been the subject of various studies in recent years (e.g. DARTS (5) and PIARC (4)).

As well as the quality of the data, risk estimation is subject to variability depending on the type of model or calculation used which can range from simple linear analyses to detailed, coupled 3D CFD simulation, evacuation modelling and incapacity dose assessment; and the experience and technical assurance processes used by the modelling team.

2.2.1 Tolerability of Risk

In many cases, the risk evaluation process of assessing the tolerability of the estimated risk, the acceptance criteria are linked to specific risk estimation tools. For example, in many European countries (e.g. The Netherlands, Austria, Italy and Switzerland) there are specific risk tolerability criteria expressed by the FN graph that are specifically linked to the national risk analysis models (e.g. the RWSQRA-model in NL and the Austrian Tunnel Risk Model-TuRisMo in Austria).

In the UK, the BD78/99 (6) standard for tunnel design contains no specific, national safety level targets. The overall requirement is to demonstrate that risk is reduced to as low as reasonably practicable (ALARP) – see GG104 Requirements for safety risk assessment (7) and Regulatory Reform (Fire Safety) Order. The ALARP principles are reasonably well established with regard to UK health and safety but the application of risk acceptability criteria for road tunnels specifically is not so well established in the UK. Demonstration that risk is ALARP, or that measures are implemented as far as is ‘reasonably required’ is therefore not often a straightforward task.

UK standard GG104 (for safety risk assessment – not specifically applicable to tunnels but provides a general framework applicable to the highway network) states that where the costs of safety mitigation measures is weighed against their benefits to show a benefit-cost ratio (BCR) of >2, then they ‘can be promoted on safety grounds’. No guidance is given on specific application to safety systems design in highway tunnels, so this criterion is subject to interpretation.

2.3 Key Challenges

2.3.1 Design Fire Criteria

The design fire criteria (considered here to comprise the peak heat release rate- HRR, and the fire growth characteristics – the fire curve) are key considerations in the design for safety in road tunnels. The decision on fire design criteria for the tunnel and systems, will have a direct influence on design decisions for tunnel ventilation, fire suppression systems, evacuation facilities, and communications systems. As noted in US Standard NFPA 502 (8), and widely accepted in the industry, the design fire is not necessarily the worst fire that is possible, engineering judgement is required to be used to establish the probability of occurrence and the ability to achieve practical solutions. As such, the decision on the design fire criteria is one for the designer to determine and agree with relevant stakeholders (including the fire services and other relevant authorities). Under these circumstances, the chosen criteria may be different in different facilities for reasons of differences in traffic volumes and types, different tunnel requirements, or simply different opinions and requirements of stakeholders. Further work is needed in the industry to limit subjectivity and drive more consistency into selection of design fire criteria and consequent safety levels for road tunnels.

2.3.2 Equality

Legislation and standards across the world (e.g. EU Dir, UK Equality Act), require that designers consider the needs of those with reduced mobility in the design of safety and evacuation facilities for tunnels. The UN Convention on the Rights of Persons with Disabilities (A/RES/61/106 (9)) requires that appropriate measures are provided to ensure access, for persons with disabilities, on an equal basis with others, to the physical environment, and to transportation. In the UK, the Equality Act (10) requires that designers do not discriminate against those with ‘protected characteristics’ which include reduced mobility characteristics. The EU Directive (11) requires that special consideration be given to those with reduced mobility.

Disabilities, or reduced mobility may include such conditions as visual impairments, hearing impairments or intellectual and psychological impairments. Other physical factors may include those of short stature, pregnant women, elderly persons, persons with young children and obese persons.

Interpretation of the requirements during design for new tunnels and in the upgrade of existing tunnels is not so straightforward. For example, where existing infrastructure presents difficulties for the self-rescue of those with disabilities or impairments (due to steep gradients, narrow lanes, trapped occupants etc.), it may be arguable that the requirement of non-discrimination requires that the environment be maintained tenable for those persons in the tunnel, at least until they can be provided with assistance. This in turn raises questions about providing steady-state tenability, rather than a traditional approach of providing tenability for a fixed duration deemed sufficient for self-rescue. Further work (such as that in progress but not

published yet by PIARC) is needed in the industry to support designers in their determination of appropriate levels of attention to the needs of those with reduced mobility.

2.3.3 Temporary Safety Reduction

A question that often arises in the design of tunnel safety systems, and in the consideration of acceptable levels of safety, is the tolerability or not of periods of operation during which safety levels are sub-optimal (or lower than the design level of safety). This might occur for example if systems or facilities are temporarily degraded due to failure or incident, or if maintenance/refurbishment operations are underway.

There may be an argument for sub-optimal safety levels to be acceptable for short periods. But then the question arises as to how long such conditions may prevail before their duration is deemed unacceptable. This may be the subject of analysis of overall average safety levels over a defined period to show that a short period of enhanced risk is deemed acceptable on the basis that it is shown to be only a small impact on the overall, long-term safety risk. This may be seen as reasonable, given that tunnel safety risk often deals with low-frequency, high-consequence scenarios where overall risk decisions are based on judgements over the long-term.

However, if an incident were to occur in a tunnel during a period of sub-optimal safety levels, the argument that the longer-term safety risk is not significantly higher may not provide sufficient justification. The public may (rightly, in the view of the authors of this paper) expect that the safety levels in the tunnel are maintained at or above the minimum at all times – this means at or above the design level of safety.

A strategy of maintaining safety levels at all times requires more detailed consideration of the requirements of the operational stage, at an early stage in design. In this way, the design of tunnel systems, equipment and facilities will be driven by the knowledge that degradation in safety levels (due to degradation in equipment for example) can and should lead to the tunnel being made unavailable to traffic on safety grounds. This will drive the design for appropriate redundancy and/or systems resilience so that degradation, failure, incidents and renewals can be managed with minimum interruption to normal traffic operation, without safety level degradation. This is the subject of the subsequent sections of this paper.

3. MOR Principles

Minimum Operating Requirements (MORs) have been the subject of much debate in road tunnel safety systems design. In recent years, progress has been made in the characterisation of MORs in terms of Safety Functions - e.g. see CETU (12) - of the tunnel, rather than in terms of minimum requirements for individual elements of tunnel systems or equipment.

3.1 Safety Functions

Safety Functions (and their sub-functions) may be defined as the functions of the tunnel in meeting the key safety objectives. With the minimum requirements applied to these Safety Functions, rather than to specific items of equipment or systems, a system or item of equipment may degrade or fail but if the relevant Safety Function is being achieved by other equipment or systems, then the MOR may not necessarily be breached.

Key, top-level Safety Functions may comprise the following:

1. Manage incident likelihood
2. Detect incident
3. Manage incident consequences

Within each top-level Safety Function, a range of safety sub-functions may be defined as illustrated in Figure 4. Under each safety sub-function there may be different items of equipment, systems, facilities and/or procedures that support that sub-function (and perhaps other sub-functions), and therefore its top-level Safety Function.

3.2 Degrading Conditions

The MOR is considered to reflect the minimum level of safety accepted by tunnel users so if the tunnel is below its MOR then it should not normally be open to traffic. If a system failure or unavailability results in a Safety Function not being fully met, then measures are required to offset that degradation and provide equivalence in order to remain above MOR for that Safety Function.

The availability of some tunnel systems will compensate for other tunnel system failures, either fully or in part where Safety Functions are performed by several systems. Compensatory systems may enable the tunnel to stay above the MOR. Where insufficient compensatory systems are in place, additional mitigation may be required to provide the equivalent level of safety to stay above MOR.

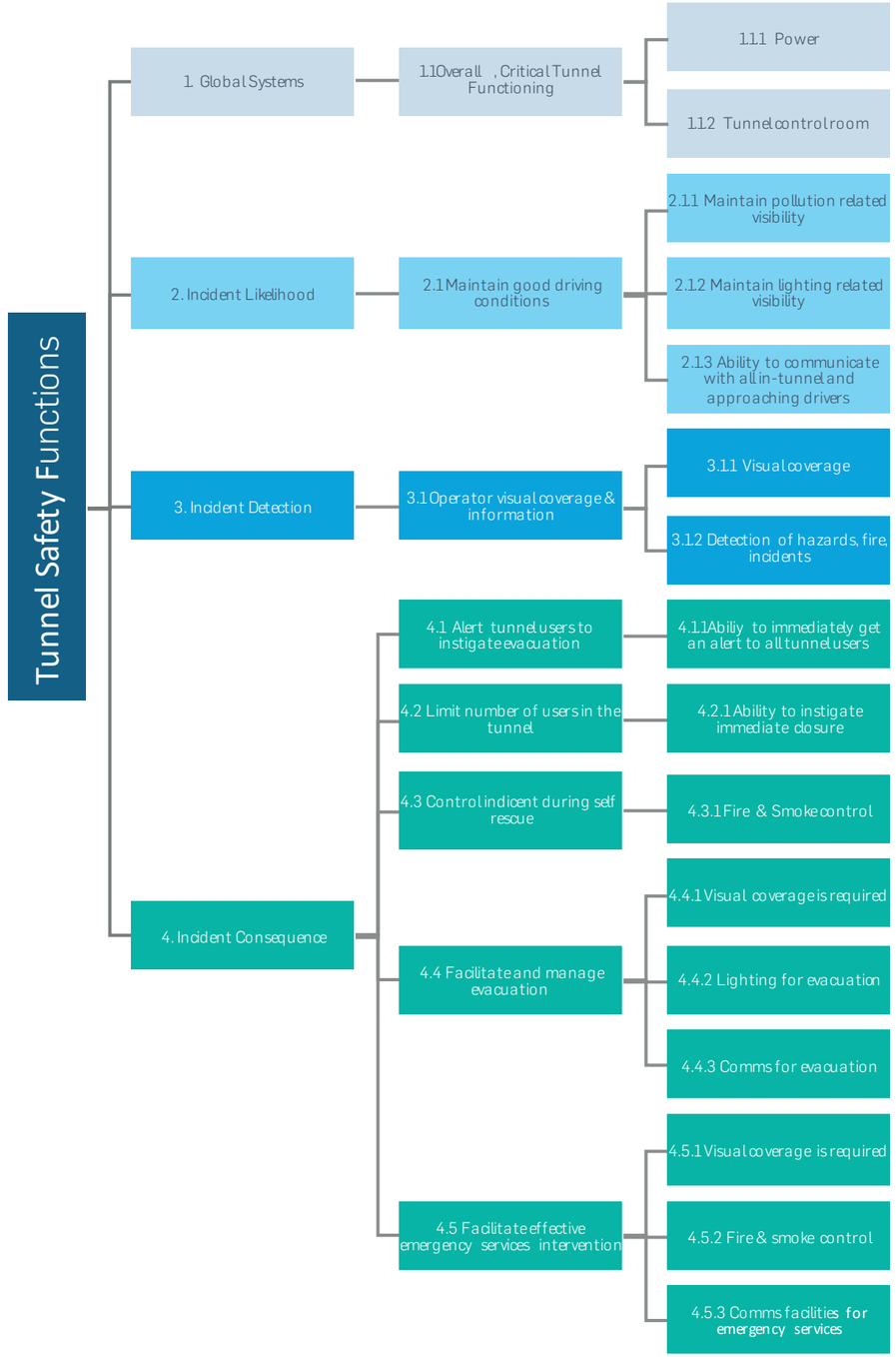

Figure 4: Illustration of safety functions and sub-safety functions

The equivalence of compensatory or mitigation systems should be established and demonstrated through common sense, qualitative risk assessment or more detailed quantitative risk analysis where appropriate. Compensating and/or mitigating systems should be available and implemented immediately in order that MOR is not breached and the tunnel can remain open.

Figure 5 illustrates some of these principles. As time (x-axis) elapses in this illustration, the tunnel moves from a 'normal' operating mode with an achieved safety level above the MOR (pink dotted line), to a period of degrading systems that reduce the safety level to a point at which service cannot be maintained (solid pink line). In this example the tunnel is closed until sufficient mitigation can be applied to meet the MOR and the tunnel is re-opened. Then it follows a 'restore' phase, where the tunnel operation is restored at a lower level of service (e.g. with mitigation in place that restricts traffic), but at an acceptable safety level, above MOR; and then a recovery phase as the degraded systems are repaired/replaced and the service level returns to normal, with mitigation measures no longer required.

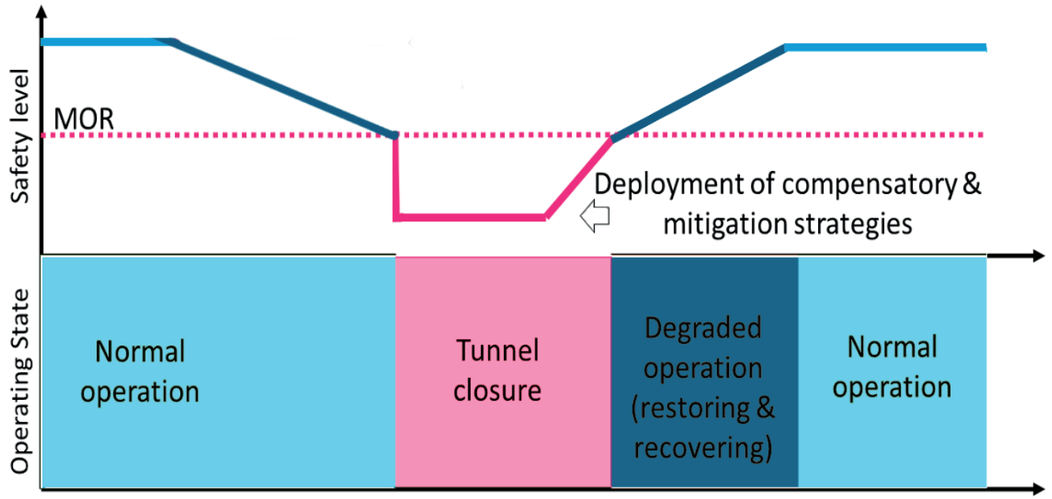

Figure 5: Illustration of MOR principles

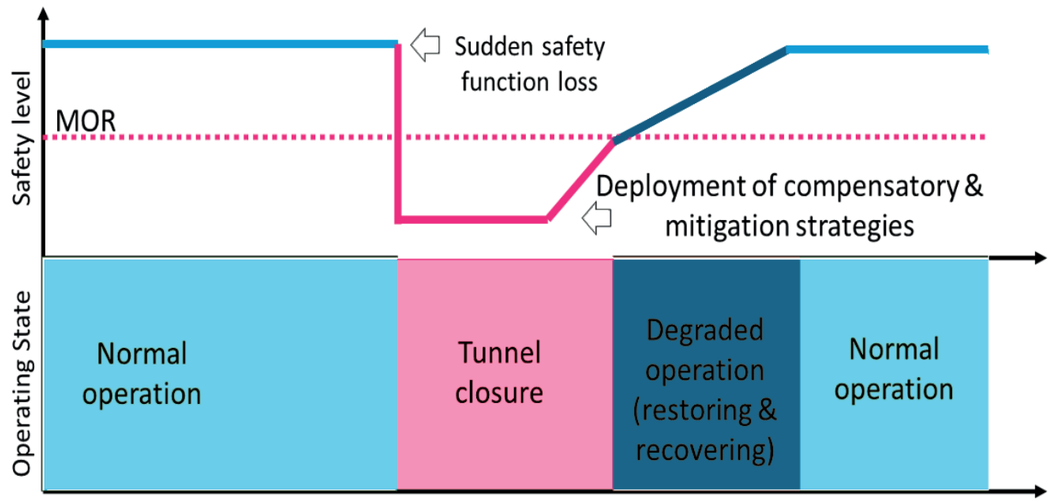

Figure 6: Illustration of MOR principles for sudden system failure

Figure 6 depicts the case of a sudden failure of a safety function with no readily available mitigation options (e.g. sudden power loss); forcing tunnel closure until the failure is rectified.

3.3 Compensation and Mitigation Measures

In the event of a degradation in tunnel operation such that the normal operating state no longer applies, the MOR process needs to be invoked so that any risks associated with the degradation or failure are compensated or mitigated such that tunnel safety levels can be maintained, and the tunnel can be kept open in some capacity.

Compensatory measures may be defined as a measure or a combination of measures that in the event of a degradation, provide adequate coverage to maintain user safety levels. Additional 'mitigation measures' may be applied if the compensation measures alone do not provide for equivalent levels of safety. Mitigation measures may be, for example:

1. Speed limit reduction (reduce likelihood and consequences of incidents)

2. Tunnel lane(s) closure (reduce traffic volumes and therefore risk)

3. Traffic restrictions (reduce vehicle size and fire size potential)

4. Example MOR Implementation

In the section, the following MOR scenarios for a hypothetical reference tunnel are presented:

a. Scenario 1 when the failure of a system does not compromise the safe operation of the tunnel (no safety impact),

b. Scenario 2 when the failure of a system requires implementation of additional operation strategies to keep the tunnel above MOR, and

c. Scenario 3 when the failure of a system results in a tunnel closure.

Note that this section is not focused on how to develop the MOR, or to score the safety functions or how to identify compensation and mitigation strategies. It is to illustrate how to use the MOR approach to assess the level of safety and support actions that may be required to manage tunnel safety.

4.1 Hypothetical Reference Tunnel

4.1.1 Tunnel Configuration

A hypothetical 3-lane road tunnel of 550 m length with unidirectional traffic is considered with the following assumptions:

- Speed limit is 30 mph;
- No-traffic restrictions;
- Fully operational control buildings located at the north and the south portals;
- Longitudinal ventilation system;
- Mechanical, Electrical and Public Health (MEP) systems compliant and fully operational.

A schematic of the tunnel indicating the considered MEP systems is shown in Figure 7.

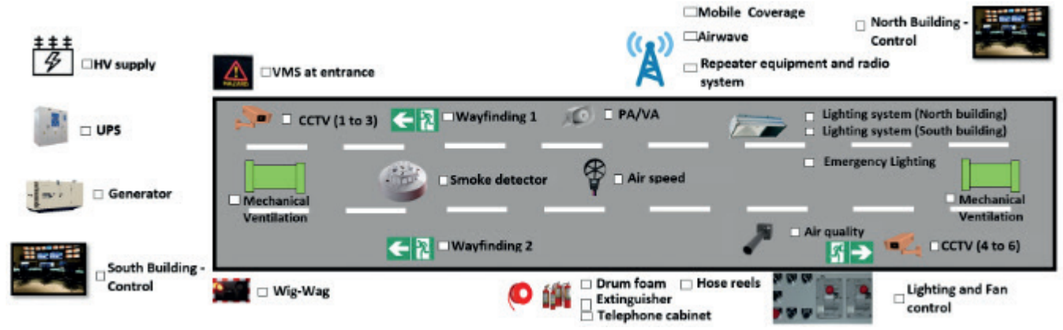

Figure 7: Schematic of the hypothetical tunnel

4.1.2 Baseline Level of Safety of Tunnel (in optimal condition)

It is considered in this example that all safety functions of the tunnel (without any degraded systems) are above the MOR - defined in this example as 100 safety points. Figure 8 illustrates the assumed safety level of each function as well as the MOR threshold (pink line). Note that for simplification, the horizontal axis shows the reference numbers of the safety functions given in Figure 4.

4.2 Scenario 1: Failure of Northern Control Building

In this example scenario, the operation of the tunnel via the northern control building is unavailable due to a component failure. This system has a potential impact on a critical tunnel function (see Figure 4 - Function 1.1.2).

Because of this failure, the safety contribution of this system (1.1.2 Tunnel Control - initially scored at 100 points) is dropped to 0 points (as it is assumed to be unavailable). This reduces the overall level of safety from 210 to 110 points. The tunnel remains above the MOR and its normal operation is therefore not affected.

Table 1 shows the MOR for this safety function (1.1.2) showing the combination of contributing tunnel systems and equipment as well as the impact of the failure. The intent of this table (as well as tables 2 and 3) is to illustrate how MORs could be derived; either at design stage or following a major revision to existing tunnel MORs and operational procedures. This ultimately will be following an implementation stage for easier operator reference (i.e. MOR alarms built within the SCADA system).

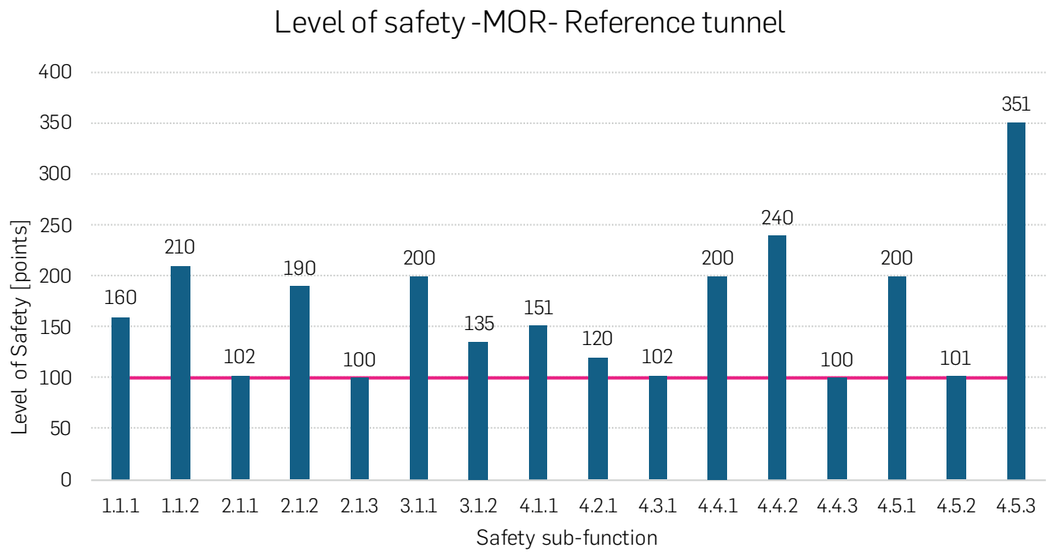

Figure 8: Level of safety in relation to each safety functions vs MOR threshold at 100 points.

Table 1: Overall, Critical Tunnel Functioning Safety Level of Degraded Tunnel Due to Northern Control Building Failure

M.O.R Matrix for Decision				Contribution of Elements to Safety Function		"Total level of safety score"	Risk Mitigations			Mitigated Level of Safety
Safety Functions & performance			Contributing Elements	MAXIMUM Level of Safety Score if Safety Requirement is met	ACTUAL Level of Safety Score		Mitigation Measure	MAXIMUM % point contribution	ACTUAL % point contribution	
Global Systmes	Overall, critical tunnel functioning	1.1.2 Tunnel Control Room	North Control Building	100	×	110	None			110
			South Control Building	100	100					
			Local control panels for smoke and lighting control	10	10					
		Compensatory strategies	N/A	0	0					

Figure 9 shows the MOR for all the safety functions of the tunnel for both the reference tunnel and the degraded tunnel. The dark blue bar represents the safety level of the reference tunnel and the light blue bar represents the safety level for the degraded tunnel.

4.3 Scenario 2: Failure of Variable Message Sign (VMS) at Portal

In this example scenario, a failure in the VMS is detected. This event impacts on the ability to alert tunnel users of any hazards as well as on preventing users entering the tunnel (see Safety Functions 4.1.1- Ability to alert tunnel users; and 4.2.1- Ability to instigate immediate closure).

Because of this failure, the overall level of safety associated with these functions is reduced. Special attention is paid to 4.2.1 for which the MOR is breached (safety points reduced from 120 to 70). Under these circumstances, the tunnel should be closed to traffic.

However, the tunnel operator is able to deploy mitigation strategies (in this case, lane control and speed limit reduction), resulting in an increase of the level of safety from 70 to 125 points (above the MOR). Note that in this case, the mitigation measure, whilst not directly offsetting the reduced functionality of systems to alert tunnel users to an incident, provides a risk reduction measure by reducing the likelihood of an incident occurring.

This scenario is illustrated in Table 2 and Figure 10. Note that the turquoise bar in Figure 10 represents the final level of safety once the mitigation strategies are applied.

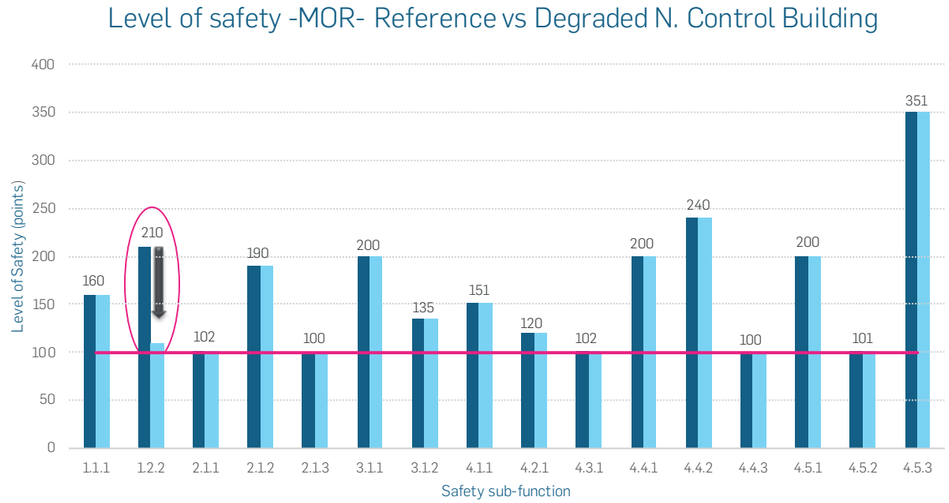

Figure 9: Comparison between the reference vs the degraded tunnel due to northern control building failure

Table 2: Safety Level of Degraded Tunnel Due to VMS Failure

M.O.R Matrix for Decision			Contribution of Elements to Safety Function		"Total level of safety score"	Risk Mitigations			Mitigated Level of Safety
Safety Functions & performance		Contributing Elements	MAXIMUM Level of Safety Score if Safety Requirement is met	ACTUAL Level of Safety Score		Mitigation Measure	MAXIMUM % point contribution	ACTUAL % point contribution	
4.1 Alert tunnel users to instigate evacuation	4.1.1 Ability to immediately get an alert to all tunnel users	Wayfindings	60	60	61	Speed limit reduction	**25 → 25**		116
		VMS	1	1		Lane closure	**30 → 30**		
		PA / VA System	90	×					
	Compensatory Strategies	N/A	0	0					
4.2 Limit number of users in the tunnel	4.2.1 Ability to instigate immediate closure	Entry Ganty (1 and 9)	50	50	70	Speed limit reduction	**25 → 25**		125
		VMS at entrance	50	x					
		Wig-wags	20	20		Lane closure	**30 → 30**		
	Compensatory Strategies	N/A	0	0					

Level of safety -MOR- Reference vs Degraded VMS

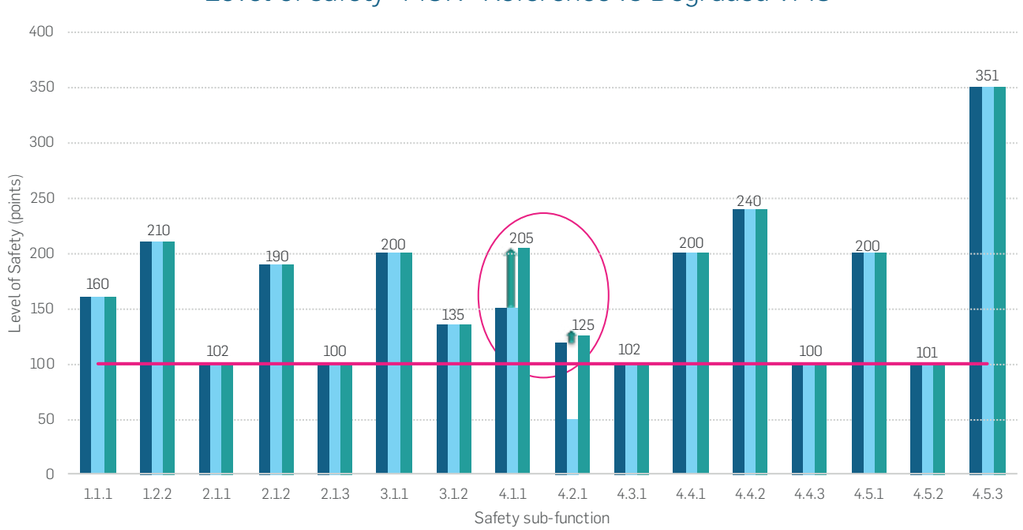

Figure 10: Comparison between the optimal condition (navy) tunnel vs the degraded tunnel due to VMS failure (light blue) and the residual condition after mitigation (turquoise)

Table 3: Safety Level of Degraded Tunnel Due to PA/VA Failure

M.O.R Matrix for Decision			Contribution of Elements to Safety Function		"Total level of safety score"	Risk Mitigations			Mitigated Level of Safety
Safety Functions & performance		Contributing Elements	MAXIMUM Level of Safety Score if Safety Requirement is met	ACTUAL Level of Safety Score		Mitigation Measure	MAXIMUM % point contribution	ACTUAL % point contribution	
4.1 Alert tunnel users to instigate evacuation	4.1.1 Ability to immediately get an alert to all tunnel users	Wayfindings	60	60	61	Speed limit reduction	**25 → 25**		116
		VMS	1	1		Lane closure	**30 → 30**		
		PA / VA System	90	×					
	Compensatory Strategies	N/A	0	0					
4.4 Facilitate and manage evacuation	4.4.3 Comms for evacuation from potential design fire	PA VA system	100	×	30	None			30
	Compensatory strategies		30	30					

Level of safety -MOR- Reference vs Degraded PA / VA

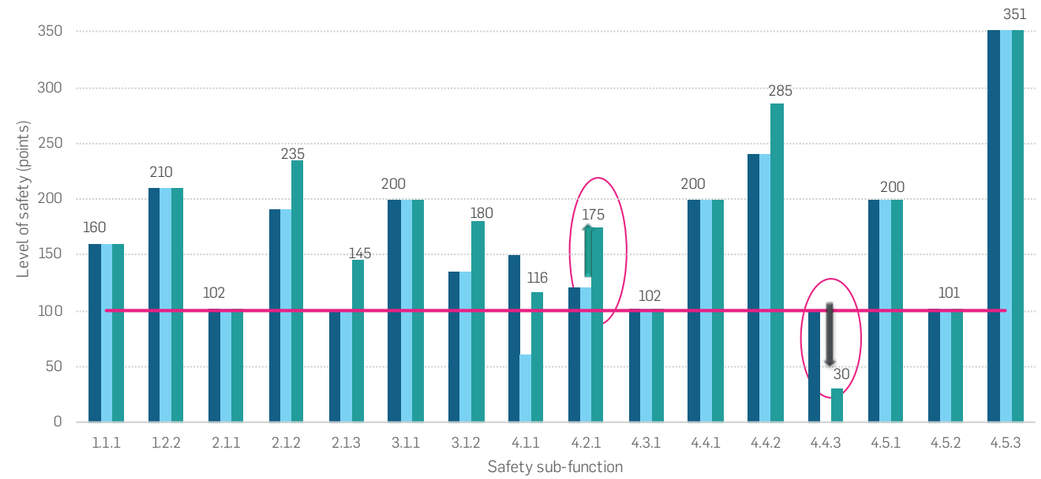

Figure 11: Comparison between the optimal condition (navy) tunnel vs the degraded tunnel due to PA/VA failure (light blue) and the residual condition after mitigation (turquoise)

4.4 Scenario 3: Failure of the PA/VA System

In this example scenario, a failure in the public address / voice alarm (PA/VA) is detected. This event has an important impact on the operator's ability to alert tunnel users of hazards as well as instigating evacuation (Safety Function 4.1.1 Ability to alert tunnel users and 4.4.3- Communications for a potential fire).

Because of this failure, the overall level of safety of these functions is reduced and the MOR is breached (from 151 to 61 in case of function 4.1.1 and from 130 to 0 in case of function 4.4.3). In this case, the deployment of compensatory and mitigation strategies are unable to demonstrate equivalent safety to that when the PA/VA is operational, and the tunnel should be closed to traffic.

Note that 'failure' of the PA/VA system should be pre-defined and may be described as a failure of [x] or more speakers, or zones. Note also that action to close the tunnel should be preceded by appropriate prior consideration of the potential transfer of risk from the tunnel route to an alternative route. This scenario is illustrated in Table 3 and Figure 11.

Conclusions

1. At the design stage, it is incumbent on those responsible for tunnel safety to scrutinise the potential for major vehicle fires. This requires an understanding of the mechanisms of failures, which should include the technical aspects (the chain of events that might occur as a result of a system or component failure, for example) and the non-technical aspects (the causal factors that allow events to occur, and systemic factors in the industry).

2. Tunnel operational experience with regards to safety may not reflect the design intent, because of changes with time, or differences between design and as-built. Where the two-way communication of safety and risk information between design and operations at commissioning and handover, as well as throughout the operational phase of the tunnel, is inadequate, the management of change is unlikely to be effective.

3. Appropriately designed MORs provide a means of achieving clarity in the design level of safety (the design intent), the safety impacts of system degradation (and options/requirements for maintaining safety levels), and the impacts of change.

Recommendations

1. Effective design and implementation of tunnel safety throughout the lifecycle of a tunnel project should be recognised as requiring scrutiny of the non-technical causal and systemic factors, as well as the technical aspects.

2. Disconnect between design and operation should be mitigated through the early stage development of MORs and their maintenance as a working system that evolves through the design, construction and operational phases.

3. Early MOR development should 'drive' the design for resilience and redundancy in tunnel systems.

4. The MOR documentation should be developed at an early stage in design (at feasibility / conceptual design stage) and then refined and maintained throughout the lifecycle of a tunnel project.

Acknowledgements

Originally Published and presented as Road Tunnel Safety Levels and Minimum Operating Requirements; BHR Group's 18th International Symposium on Aerodynamics, Ventilation & Fire in Tunnels, Athens, Greece, 25th – 27th September 2019.

References

(1) UK Vehicle Fire Statistics: https://data.gov.uk dataset vehicle-fires. Accesses November 2018.

(2) Johnson, William G. 1980. MORT Safety Assurance System. New York: Marcel Decker.

(3) Leveson, Nancy G. 2011. Engineering a Safer World – Systems Thinking Applied to Safety. MIT Press, Cambridge Massachusetts.

(4) PIARC Technical Committee C.4 Road Tunnel Operation 2013. Risk evaluation, current practice for risk evaluation for road tunnels.

(5) Durable and Reliable Tunnel Structures (DARTS) May 2004. Report R4.4 Identification and quantification of hazards - Part fire and smoke.

(6) UK Highways Agency, 1999. Design Manual for Roads and Bridges Volume 2 Section 2 Part 9. BD 78/99 Design of Road Tunnels.

(7) Highways England June 2018. Design Manual for Roads and Bridges GG 104 Requirements for safety risk assessment (formerly GD04/12 and IAN 191/16).

(8) National Fire Protection Association NFPA 502. Standard for Road tunnels, Bridges, and Other Limited Access Highways. 2017.

(9) United Nations. General Assembly. A/RES/61/106. Sixty-fifth session Agenda item 67 (b). Resolution adopted by the General Assembly on 13 December 2006. [online] Available at:

https://www.un.org/en/development/desa/population/migration/generalassembly/docs/globalcompact/A_RES_61_106.pdf.

(10) Legislation.gov.uk. (2010). Equality Act 2010. [online] Available at: http://www.legislation.gov.uk/ukpga/2010/15/contents.

(11) Directive No. 2004/54/EC of the European Parliament and of the Council on the minimum safety requirements for tunnels in the Trans-European Road Network.

(12) CETU Information Memo No 23 – Definition of safety functions. Application to degraded operating modes and minimum operating requirements. July 2014.

Traction Power Innovations for a More Sustainable Melbourne Tram Network

David Edward Anderson

BE (Hons)
Project Manager
Department of Transport Victoria
Melbourne, Australia

Alain Croset

HND
Principal Consultant
Engineering, Design and Project Management
Melbourne, Australia

Abstract

The Melbourne Tram Network is the largest in the world with 250 kilometres of track and 490 trams. The city's fast-growing population has triggered a new approach to improve sustainability. The New Rolling Stock Program managed by Department of Transport Victoria included an out-of-the-box option analysis for traction power supply. It was undertaken to address forecast patronage growth and retirement of the high-floor tram fleet while increasing the energy efficiency drawn from the Traction Power Supply. The effort included simulation of many combinations of standard and new technologies both on-board and wayside to assess their outcomes at both location and network levels. To avoid drastically increasing energy consumption, introducing new vehicles with on-board energy storage and optimising sectioning of the electrical distribution was found essential for a substantial improvement in energy management. The proposed upgrades enable better recovery of braking energy, minimising losses through local on-board re-use preference over transferring it to other trams. It means capital minimisation upgrades to key power network assets. To complete the improvement, an innovative energy management of the on-board energy systems will be required from tram suppliers to optimise both the on-board energy saving and the overall Traction Power Supply efficiency. Optimising upgrades necessary to supply the additional and higher passenger capacity vehicles included some additional substations. However, in some specific areas, side feeders and wayside energy storage systems were a cost-efficient part of the solution to avoid substation land acquisition. Simulations showed that even with the increase in passengers carried, the network energy consumption would be no greater than the present-day level. These systemic and holistic upgrades will reduce investments needed to adapt the network to the population growth in the future.

Keywords

TRAM Network; Low-Floor Trams; Sustainability; Energy Management; Cost-Effectiveness

1. Introduction

The Melbourne Tram Network (MTN) (Figure 1) is the largest in the world with 250 kilometres of double track and 490 trams. Due to strong population growth in recent years, the network is now reaching capacity. Projections estimate that by 2051, Melbourne's current population of 5 million people will increase to 7.9 million. To support this level of growth, the public transport system must be upgraded to provide increased capacity and additional routes provided to align with population growth areas.

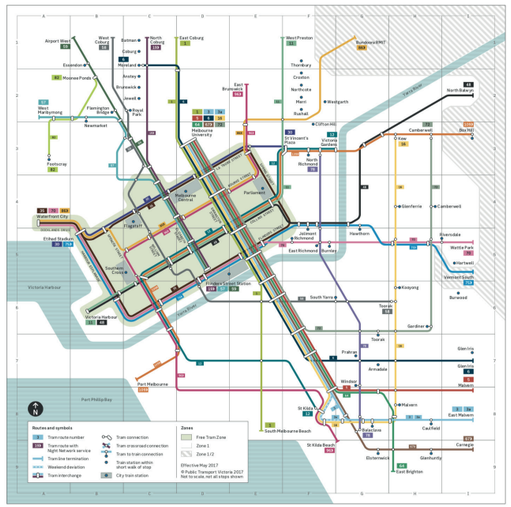

Figure 1: TRAM map

To improve network capacity, the New Rolling Stock Program, managed by the Department of Transport Victoria, will introduce approximately 250 Next Generation Trams (NGT) to the network. These new higher capacity, low-floor trams will replace the existing high-floor fleet which are approaching their end of life.

Trams on the MTN are 75 per cent operated in multiple-use road environments, including cars and cyclists. 25 per cent comprises segregated tram-only operation sections. Powered by the Traction Power Supplies through overhead lines, trams require energy for:

- Traction/vehicle propulsion; and
- Auxiliary equipment like passenger information and heating and air-conditioning.

Technological improvements available have resulted in key on-board systems (such as traction and braking systems) being more energy efficient than those fitted to previous generations of rolling stock. Combined with the use of lighter materials for vehicle construction, this results in the traction/vehicle propulsion component consuming less than previous generations of vehicles, per unit length.

Modern on-board equipment and features provide an improved passenger experience, including air-conditioning, higher acceleration performance, passenger information systems, and many other sub-systems that did not exist 20 or 30 years ago. These improvements partially offset the reduction in the traction/propulsion system energy consumption.

In addition to the introduction of new trams, to further increase network capacity service frequency will increase on high-demand routes thereby increasing energy consumption on these routes.

2. Problem Statement

The introduction into service of new modern trams with increased service frequency will require a significant additional amount of energy to be delivered to the network. The main goal of the project was to identify the right solutions to achieve this in a sustainable and cost-effective way.

2.1 Auxiliary Power Consumption

The high-floor trams to be retired are fitted with minimal on-board equipment. Maximum auxiliary power draw varies between 4 kW and 32 kW dependent on vehicle length and HVAC provision.

In comparison, new modern trams are fully air-conditioned and fitted with modern on-board equipment. They are expected to have a maximum auxiliary power draw of 50 kW, which represents an increase of 52% from the longer high-floor trams to be retired and 11 times more than the shorter variant.

2.2 Traction Power Consumption

High-floor trams have a maximum traction power of 420 kW for the short variant and 486 kW for the longer variant.

In comparison, new modern trams with higher passenger capacity fitted with standard traction-braking technology would have a maximum power of 550 kW which represents an increase of 30% from the shorter high-floor trams and 15% from longer high-floor trams as shown in the vehicle power curves for each group of like trams as shown in Figure 2.

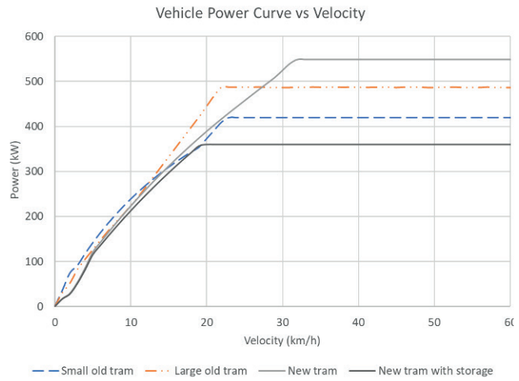

Figure 2: Vehicle power curve

3. Baseline Energy Consumption

To ensure rolling stock can operate at full performance, the traction power supply network must be able to provide the required maximum power and energy. While this characteristic is available from tram supplier datasheets, the energy consumed by the rolling stock over the time is not readily available. As such, the team had to establish these figures for the overall consumption of the network. The Department of Transport Victoria owns a full TrainOps® model of the Melbourne Tram Network. This model has been jointly developed by the Department of Transport Victoria and LTK using LTK's operation and electrical network simulation software TrainOps®. Using the results of network simulation, the energy consumption of the existing network has been evaluated and compared with the energy bill.

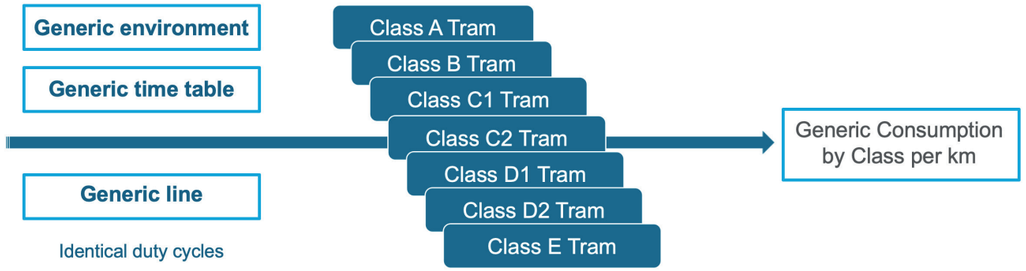

Figure 3: Baseline energy consumption

To determine the current energy consumption of the overall Melbourne Tram Network, a model was developed to characterise the energy consumption of all tram types used on the Melbourne Tram Network. This model was adapted from the methodology developed by the Optimal Strategy to Innovate and Reduce Energy Consumption in Urban Rail Systems (OSIRIS) rail research project (Iordache, 2013). Completed in December 2014, OSIRIS consisted of 17 project partners including major stakeholders such as railway manufacturers, public transport operators, and universities. Its goal was to enable a reduction in the overall energy consumption within Europe's urban rail systems by 10% from 2012 levels by 2020.

Workshop 1 of the OSIRIS project identified a method for standardising the duty of rolling stock and building energy consumption figures. Adapting this methodology, the energy consumption of all tram types used on the MTN was established. Single-vehicle runs were simulated on the same chosen route, with traction and auxiliary consumption integrated and linearised per kilometre, which enabled the maximum energy consumption for every tram class to be determined (Figure 3).

The whole network was then simulated using the existing rolling stock to establish the energy consumption of the then-present 2018 services. The network was then simulated using new trams operating at a higher service frequency to establish the baseline energy consumption for complete low-floor fleet in the year 2031. The total MTN energy consumption would rise from 2018 operations with existing ageing fleet of 153 GWh to 200 GWh for 2031 all low-floor fleet without OESS at the increased service frequency planned. This is an increase of 30 per cent, assuming there are no wayside or on-board energy storage systems (Figure 4).

4. Engineering Approach

In order to run new modern vehicles on the network at increased service frequency, the maximum power and energy consumption will increase, requiring costly upgrades to the network. In order to determine the preferred upgrade approach, an options analysis was conducted to analyse the benefits of new proven technologies and standard techniques to ensure upgrades were undertaken in a sustainable manner and cost effectively.

4.1 Engineering Process

Rather than addressing the increase in power and the energy consumption by adding only substations, an innovative solution mitigating standard techniques (substations (Figure 6); feeders; re-sectioning (Figure 7)) has been produced. This includes more recent proven technologies like on-board and wayside energy storage (Figure 8).

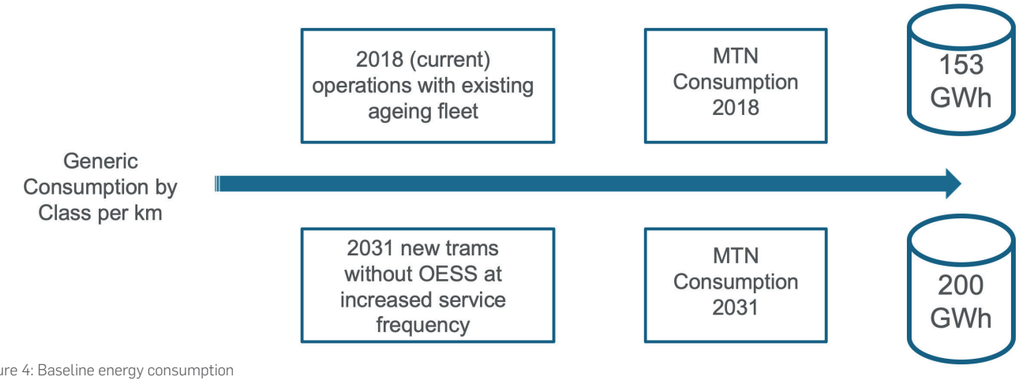

Figure 4: Baseline energy consumption

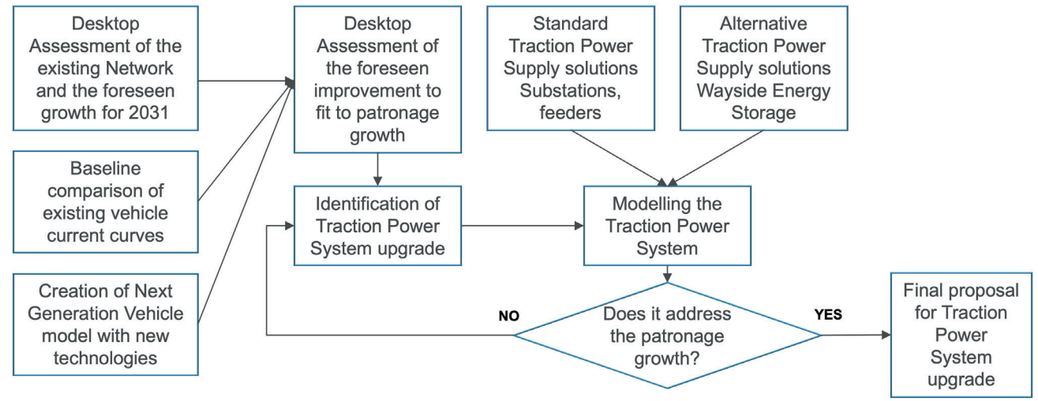

Figure 5: Engineering process

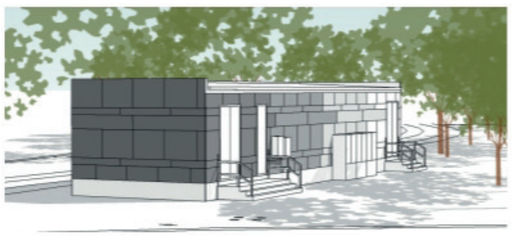

Figure 6: Substation

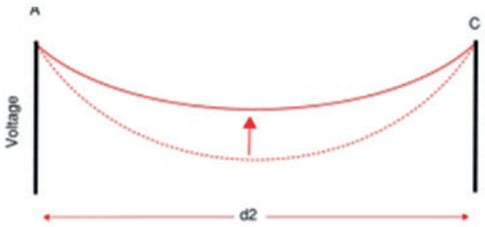

Figure 7: Voltage drop

Figure 8: Wayside energy storage system (WESS)

An overview of the process is shown on Figure 5. At first, the team conducted a desktop analysis of the Traction Power network starting with the existing network and then incorporating the route upgrades and the new tram acquisitions. Based on the existing TrainOps® model of the MTN, scenarios combining standard and new technologies have been modelled and then compared under normal system operation and degraded operation (N-1 rectifier outage conditions). Numerous simulations were necessary to achieve the optimal outcome.

A mix of the best options for each area of the network have been combined to simulate the optimum network, all offering the same coverage as the standard approach along with additional improvements. These will enable less energy consumption, reduced impact on land acquisition, and sustainability for future operational growth.

4.2 TrainOps® Modelling

The TrainOps® model has been upgraded with the network improvements necessary to address the increase in power and the energy consumption. Standard traction power upgrades were then simulated with the model. As the TrainOps® software did not support energy storage models at the time of the project, wayside and on-board tools were built separately to design the new tram traction-braking characteristics emulating energy storage functionality. This new tram with OESS then replaced the new tram without storage in the TrainOps® model.

Figure 9 is a TrainOps® model output that shows the pantograph voltage of trams running on an existing route, modified to fit the patronage growth as seen for 2031 before traction power supply upgrades. As can be seen, the voltage doesn't meet the standard voltage criteria of the network. Figure 10 shows a simulation with Traction Power Supply Upgrades that allow the line voltage to meet the criteria and to safely operate the route.

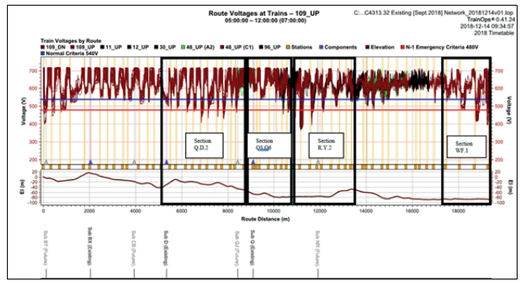

Figure 9: 2031 simulation without traction upgrade

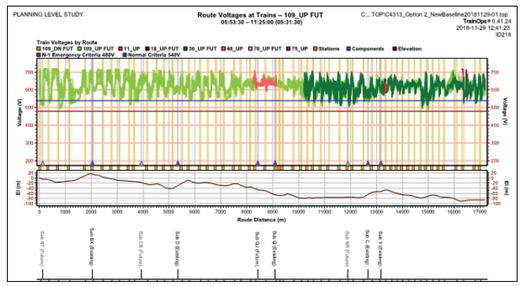

Figure 10: 2031 simulation with traction upgrade

5. Technical Solution

5.1 Option 1: Standard Traction Power Supply Solutions

The standard base approach to increase power supply to a rail network is to install additional traction power substations. Installing substations in a dense city is a very difficult and costly task as it requires land acquisition and has long lead time to deliver the solution.

Therefore, to minimise the number of new substations required to meet the increase in power demand, other standard traction power technologies have been evaluated. The two primary technologies that were assessed were sectioning optimisation and side feeders.

- Sectioning Optimisation: on a large legacy network such as Melbourne, the power is distributed from the substations to different routes by sections for fault management. One route is made of several sections and some sections are connected to other route's sections. To allow a better energy exchange from braking trams to accelerating ones, the sectioning needs to be reviewed. This is essential with more powerful trams. Optimising sectioning of the electrical distribution means that the highest current paths between trams must be assessed and their resistance minimised to reduce losses. This process included the study of connections between two separate routes when a current path can be improved. Connecting routes that were not connected before requires the re-design of the fault detection to suit the new connected routes and the trams operated on these routes.
- Side Feeders: Reducing the line resistance by adding side feeders (parallel cables) can be specifically efficient when running a higher power consumption service. The addition of side feeders reduces the line voltage drop between substations. This can be thought of as tightening a hanging wire with each additional feeder thus providing a diminishing return. Figure 7 shows how an additional side feeder, or a reduction in the effective resistance between the substations, flattens the voltage profile.

5.2 Option 2: Alternative On-Board Storage Solutions

Many tram manufacturers can now supply their trams with On-board Energy Storage Systems (OESS). Several new tram or Light Rail Train lines, mainly in Europe and China, use OESS to run without being powered by overhead wires. This is known as wire-free operation.

Unlike European networks which are new modern single lines with limited need to reduce peak power, the MTN is relatively complex with many routes, most of them shared with road traffic. While wire-free operation is the typical reason for implementing OESS, in the Melbourne context the primary purpose would be to reduce both energy consumption and peak power demand. Several trials were undertaken from 15 years ago to evaluate the outcomes of supercapacitor based OESS for energy saving and voltage stabilisation as described by Moskowitz & Cohuau (2010). Since then, OESS have been adopted by the market when the need was revealed and OESS characteristics have continued to be updated over the past 10 years as energy storage component technology has continued to evolve.

The energy saving figures and peak power reduction comparisons presented by (Frohlich & Klohr, 2008) served as a basis for building the characteristics of a NGT with an OESS. The OESS of the NGT has been characterised to limit the tram maximum power to 360 kW under the network voltage of 600 V as shown on Figure 11, 25 per cent lower than the longest length old high-floor tram.

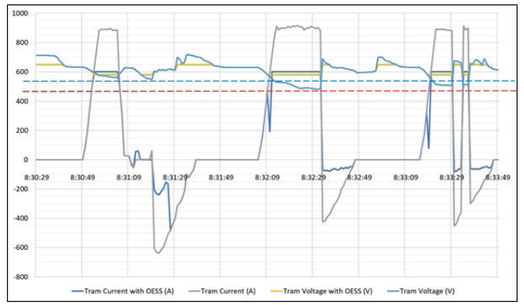

Figure 11: OESS voltages and currents

The NGT with an OESS was simulated on the same route used to characterise all the other trams and compared with a new tram without OESS. Figure 2 shows how the OESS limits the maximum power therefore reducing the current drawn from the overhead wire from 900 A to 600 A. Additionally, the OESS reduces voltage sags, keeping the line voltage higher than the network voltage limit of 540 V, shown as a blue dash line on Figure 11.

In addition to the network stability improvement provided by an OESS installed on new trams, OESS will also provide the opportunity to remove short wire sections with the new trams powered solely by the OESS rather than the overhead line. This is beneficial in sensitive areas like crossings and under low bridges. While not competing with wire-free trams operating longer wire-free distances, approaches with suppliers must show what length of wire-free section their latest energy storage technology will allow operation through.

To further enhance the benefits of OESS, it is proposed that manufacturers implement an innovative energy management system to manage in real time the best outcome between the on-board energy saving, traction power supply efficiency and short wire-free operation.

The installation of OESS can also bring a side effect to passenger comfort and safety. When a tram loses power from the overhead wire during acceleration, passengers experience a discomforting change of acceleration also called "jerk." It is the derivative of the acceleration. The situation can cause passengers to lose their balance as described by Powell & Palacin (2015). Standard traction-braking equipment can't deal with this situation as the energy that would be needed to allow a more moderate variation in acceleration cannot be provided by a simple

capacitor filter. However, this energy can easily be provided by the OESS as it represents only two to three per cent of its capacity.

Lastly, it should be noted that increases in the energy density and specific power for the latest Lithium-Ion chemistry and hybrid Electric Double Layer Capacitors (EDLC), also known as supercapacitors, is advancing rapidly. It is expected that within four years these advancements will enable wire-free operation over longer sections without even requiring power supply distribution along the route except for both ends of the lines (Croset, 2018).

5.3 Option 3: Alternative Traction Power Supply Solutions

For routes that will not be operated with NGT but will see an increase of service frequency and tram size (due to the cascading of existing trams), voltage sags and peak power are issues that need to be solved by other means. The guidelines for braking energy recovery systems in urban rail networks are issued by Devaux, F.O., Tackoen (2014), as well as the results of trials summarised by Croset (2016). in Optimizing Urban DC Supply Networks, were used to define the routes where an optimum outcome would be delivered by a Wayside Energy Storage System (WESS). A WESS is a device installed at an optimal position alongside the track capable of recovering braking energy from multiple nearby trams, delivering back the energy when needed. The needs are defined by the local set up defined to power tram accelerations nearby and/or stabilising the line voltage. The maximum distance that can be covered by this WESS depends on the sectioning, the power of the substations, the power of the trams, and the resistance of the line. Built from line simulations, a tool was set up to define the size and the main characteristics of the system. Several routes have been identified where a standard substation could be replaced by a WESS. To assess the suitability of a WESS, identified routes were simulated with a standard substation then with a WESS. The results demonstrated that two routes would benefit from the installation of a WESS instead of a substation. Figure 12 represents an electrical single wire diagram for studying the use of a WESS at Port Melbourne (PM) to enable the introduction of larger trams on this route. Figure 13 shows the effect of a WESS keeping the line voltage within the standard values, higher than 540 V shown as a blue dash line.

6. Conclusion

The operation of new modern trams at an increased service frequency requires a significant additional amount of energy to be delivered to the network. Rather than solely achieving this through the addition of new substations, three primary options were assessed to determine how this could be achieved cost effectively across the network.

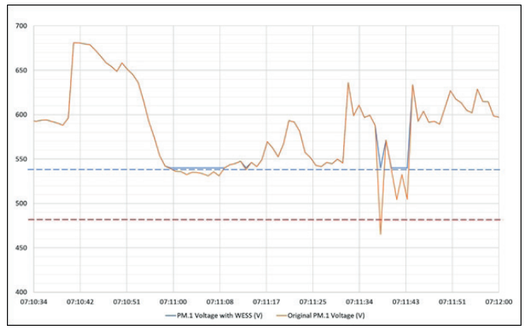

Figure 12: WESS voltages and currents

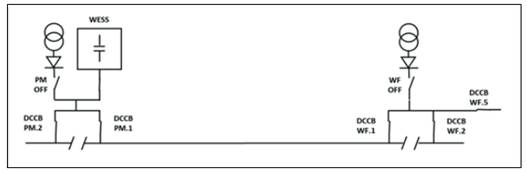

Figure 13: WESS studied area

The core means of addressing the increased energy demand on the MTN has been the introduction of an NGT with an OESS and dedicated with a dedicated on-board energy management system. While some additional substations would still be required even with the implementation of new trams with OESS, the number of substations required could be minimised further through the addition of side feeders and WESS at selected locations.

By considering the entire network, a blended use of technological solutions has been adopted to meet an increase in energy demand cost effectively and reducing land acquisitions required for new substations.

Following the validation through a TrainOps® simulation of the optimum blend of solutions, the new network consumption has been calculated and compared with today's consumption and 2031's consumption without OESS. The consumption as calculated for the optimum blend of solutions shows only a mere one per cent increase as shown on the below table, compared with today's baseline consumption. In comparison, a 30 per cent increase above today's baseline energy consumption could be expected for new trams without OESS.

By assessing both conventional and innovative technologies (Figure 14), the optimum blend of solutions has been established that will transform the journey in a NGT into a vibrant journey attracting more passengers to the world-famous MTN. The proposed solutions will improve the energy consumption and limit the investments needed to adapt the network to the population growth anticipated in the future.

Table 1: Total Network Optimum Consumption

Estimate of Total Network Energy Consumption	GWh
2018 (current) operations with existing ageing fleet	153
2031 New trams **without** OESS at increased service frequency	200
2031 New trams **with** OESS at increased service frequency	156

The Department of Transport Victoria has started an interactive design process with several manufacturers to leverage the maximum benefit to Victoria's manufacturing industry and create more jobs for a flexible and diverse workforce.

The design process will provide the Government with several well-informed proposals to choose the best new trams for Victoria's needs.

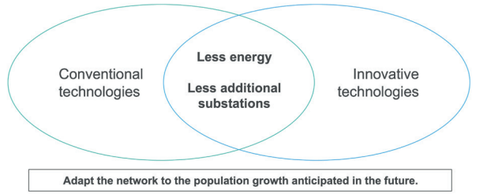

Figure 14: Conclusion

References

Croset, A. "Optimizing Urban DC Supply Networks", Tetsudo Sharyo to Gijutsu – Rolling Stock & Technology, no.233, Japan, February 2016.

Croset, A. "The future of Light Rail will be substation-free", Light Rail Conference, Sydney, March 2018.

Devaux, F.O., Tackoen, X. "WP2B Energy recovery, guidelines for braking energy recovery systems in urban rail networks" Ticket to Kyoto final report, September 2014.

Moskowitz, J.P., Cohuau, J.L. "STEEM: Alstom and RATP experience of supercapacitors in tramway operation", 2010 IEEE Vehicle Power and Propulsion Conference, VPPC, 2010.

Frohlich, M., Klohr, M., "Energy Storage System with UltraCaps on Board of Railway Vehicles", American Public Transportation Association Rail Conference, 2008.

Iordache, M., "Smart grid system definition, system studies and modeling, technologies evatuation", OSIRIS Deliverable D4.1. 2013.

Powell, J. P., Palacin, R. "Passenger Stability Within Moving Railway Vehicles: Limits on maximum Longitudinal Acceleration", Urban Rail Transit 1(2):95–103, 2015.

Muskrat Falls Hydroelectric Facility Construction Overview

Greg Snyder

FEC, P. Eng,
Engineering Manager,
Muskrat Falls Generation Project
Power, Grid and Industrial Solutions
St. John's, NL, Canada

Scott O'Brien

P.Eng,
Project Manager, Muskrat Falls Generation Project
Lower Churchill Management Co.
St. John's, NL, Canada

Ron Power

P.Eng. Deputy
Project Director - Generation, Muskrat Falls Generation Project
Lower Churchill Management Co.
St. John's, NL, Canada

Abstract

Major construction of the Muskrat Falls generating facility commenced in early 2013 with the Bulk Excavation contract. Construction of the Powerhouse commenced in 2014. The Spillway was completed and the river diverted in 2016. As of summer 2019, all major civil contracts were complete and work is now focused on installation of the turbine-generator units and completion of the balance of plant work. The project will achieve first power in 2020 .

This paper provides an overview of the facility and an update on the construction of the Muskrat Falls project. It highlights some of the key milestones achieved and successes in accomplishing the progress to date. A brief overview will also be provided for the two transmission lines, so that a full picture of the progress on this major construction project can be understood.

Keywords

Hydroelectricity; Dams; Energy; Clean Power; Churchill River

1. Overview

The Lower Churchill Development includes two potential hydroelectric sites on the Churchill River and their associated transmission systems: Gull Island Hydroelectric Development, located 225 km downstream of the existing Churchill Falls Generating Station, and Muskrat Falls Hydroelectric Development, located 60 km further downstream.

Phase one of the Lower Churchill Development, the Muskrat Falls Project, includes an 824 MW hydroelectric generating facility at Muskrat Falls, over 1,600 km of transmission lines across the province (including a subsea transmission link connecting Labrador to the island), HVDC installations including converter stations, and the Maritime Link transmission line connecting Newfoundland and Nova Scotia, being developed by Emera Inc. Figure 1 provides an overview of the generating facility location and the related transmission infrastructure.

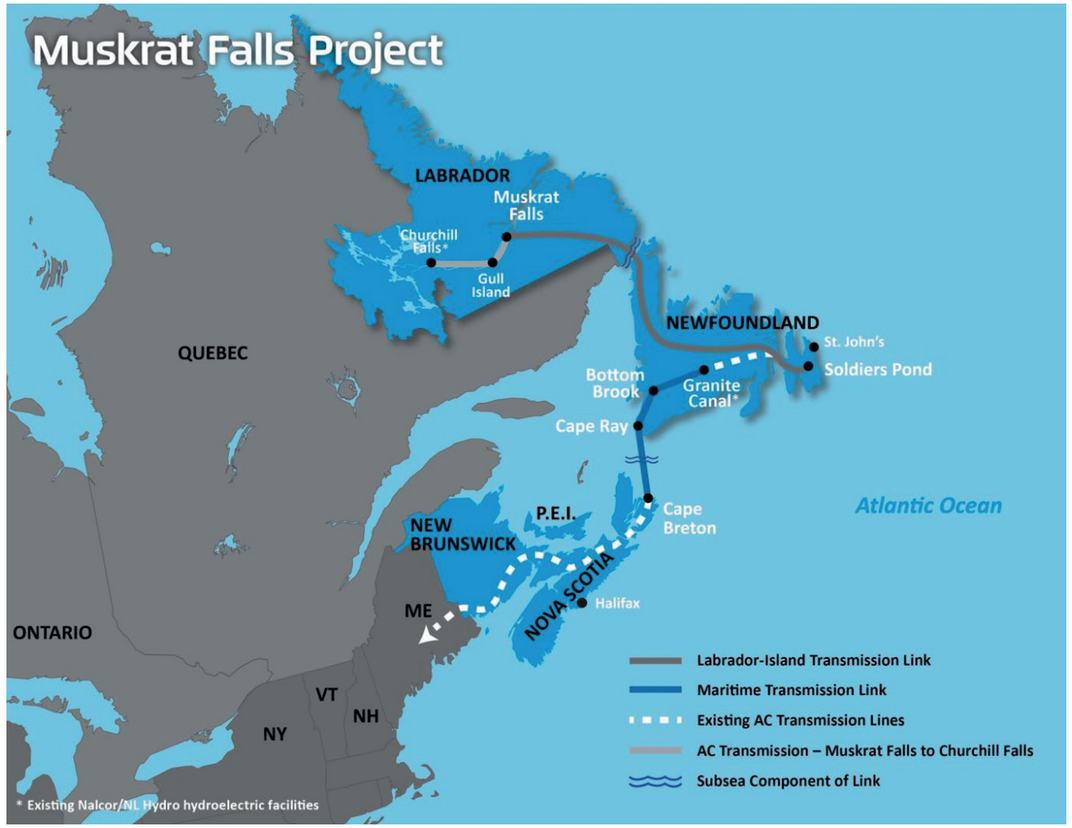

Figure 1: Project locations

Figure 2 shows a general overview of the Muskrat Falls site on the Churchill River.

Major construction of the Muskrat Falls generating facility commenced in early 2013 with the Bulk Excavation contract. Construction of the powerhouse commenced in 2014. The Spillway was completed and the river diverted in 2016. By Summer 2019, all major civil contracts were complete and work is now focused on installation of the turbine-generator units and completion of the balance of plant work. The project will achieve first power in 2020.

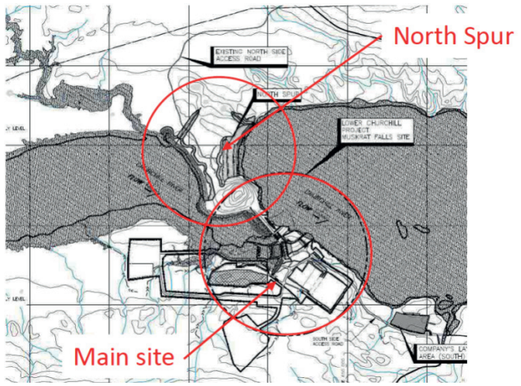

Figure 2: Muskrat Falls overview

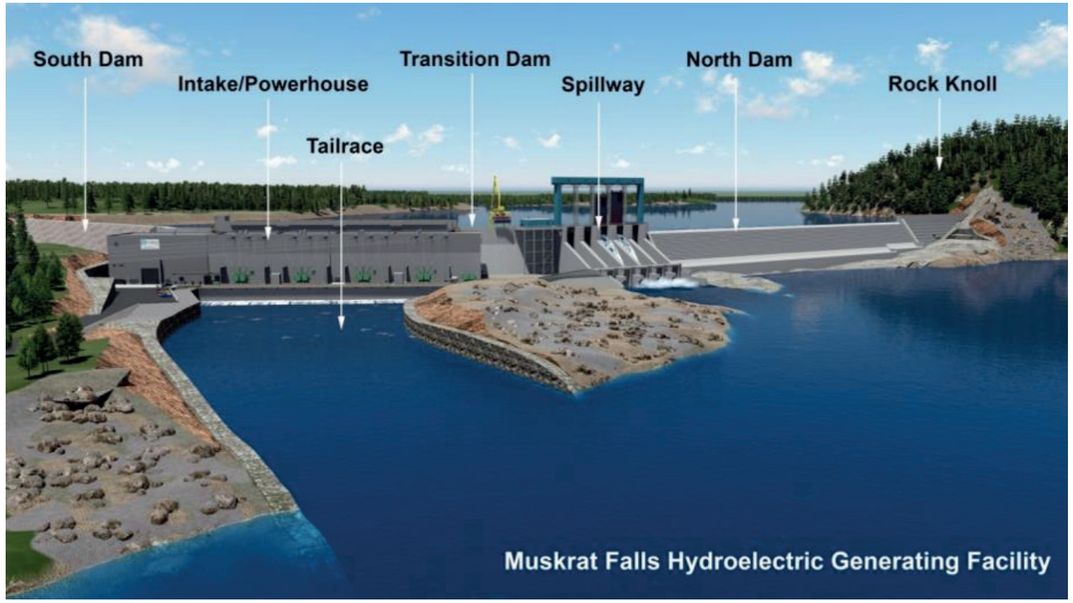

Figure 3: Overview of Muskrat Falls components

2. Components of the Muskrat Falls Facility

The water retaining structures of the Muskrat Falls facility are shown in Figure 3. They comprise of the North Spur, a natural feature of the Churchill River valley which has been stabilised and is now treated as a dam; a 450 m long by 39 m high overflow roller compacted concrete (RCC) North Dam; the gated Spillway control structure (5 x 10.5 m bays); the close-coupled four unit Intake-Powerhouse structure; and a 243 m long by 20 m high central till core rock fill South Dam. The North Dam, the Spillway, Intake and the South Dam structures are connected by concrete gravity Transition Dams.

The Muskrat Falls hydroelectric development site has a nominal 35 m of hydraulic head which is developed by water retaining structures across the Churchill River at Muskrat Falls to create a headpond for power production. The full supply level for the project is el 39 m (above mean sea level). The site is configured as a run-of-the-river style facility with limited increase in land inundation (Figure 4).

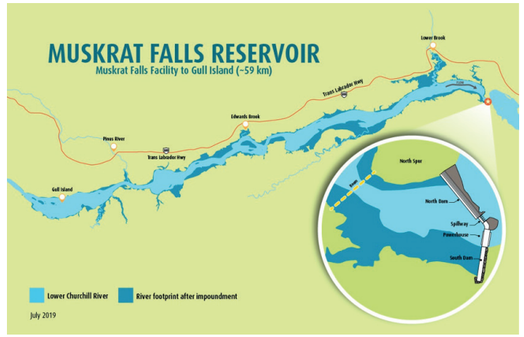

Figure 4: Muskrat Falls reservoir

2.1 Powerhouse

The Powerhouse is 84 m tall and 78 m wide and is shown in Figures 5 and 6. It will have a generating capacity of 824 MW, with 4 close-coupled Kaplan units of 206 MW each. The units will be some of the largest and most efficient in the world. The concrete structure was substantially complete in November 2017, and work continues on installation of the mechanical and electrical components.

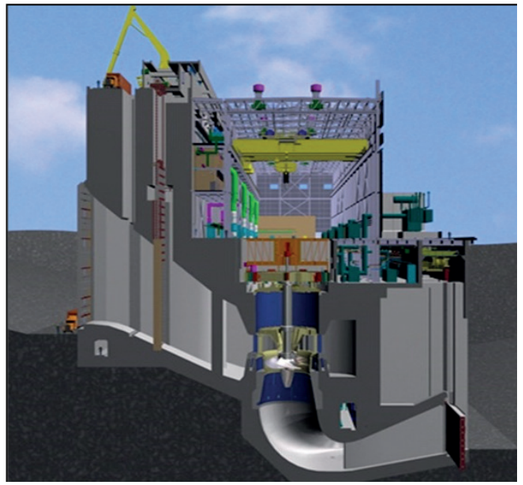

Figure 5: Cross-section of Powerhouse

Figure 6: Powerhouse Interior looking south (March 2019)

2.2 Intake and Tailrace

The Intake is made up of 4 intakes which have 3 bays each. It is 143 m wide and 56 m tall, with the intake deck at el 45.1 m. The structure was substantially complete in November 2017 and work on installation of the Intake gates was completed in April 2019. Figure 7 shows an aerial view of the Intake.

The Tailrace is made up of 4 outlets with 2 bays each. It was substantially complete in November 2017, and watered-up in November 2018. Figure 8 shows the tailrace viewed from downstream.

Figure 7: Intake prior to reservoir impoundment (May 2019)

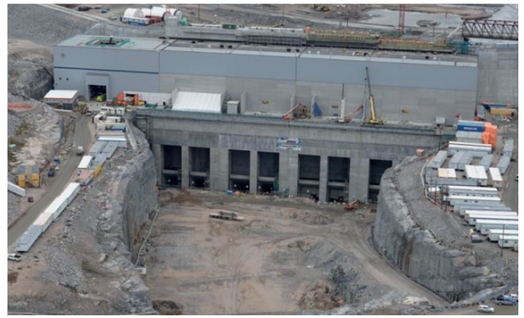

Figure 8: Tailrace prior to watering up (September 2018).

2.3 South Dam

The South Dam is a 243 m long conventional rock filled dam with a central till core, and a crest at el 47 m. It was completed in Autumn 2017. Figure 9 shows a typical cross-section of the South Dam and Figure 10 is a photograph of the South Dam, taken from the south end of the structure. The South Dam connects to the South Transition Dam.

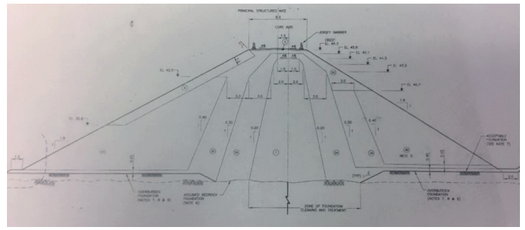

Figure 9: South Dam typical cross-section

Figure 10: South Dam, construction complete (Fall 2018)

Figure 12: North Dam construction complete (August 2019)

2.4 North Dam

The North Dam is 450 m long, with a 330 m long overflow crest at el 39.3 m. It is the final major civil component that was required for the creation of the Muskrat Falls reservoir. It is a roller compacted concrete (RCC) structure with a volume of 250,000 m3 of concrete. The RCC placement was completed in August 2018, and the conventional concrete ogee and flip bucket were completed in October 2018 (Protulipac et al. 2018). Figure 11 shows a typical cross-section of the North Dam. Figure 12 shows the completed North Dam in Summer 2019, during impoundment of the reservoir.

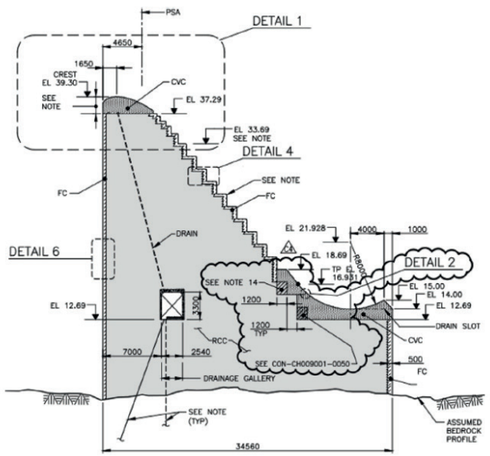

Figure 11: Typical cross-section of North Dam

2.5 North Spur

A critical feature of the development is the North Spur, a natural earth embankment that constricts the river at the project location. The North Spur is approximately 1,000 m long, 500 m wide and 45 to 60 m high, and consists of unconsolidated mixed sand and marine silt and clay. Stabilisation of this land mass was a key part of construction of Muskrat Falls and was completed in August 2017 (Ceballos et al. 2015). Figure 13 shows the design for the North Spur works, and Figures 14 and 15 provide an aerial view of the complete construction work (Bouchard et al. 2019).

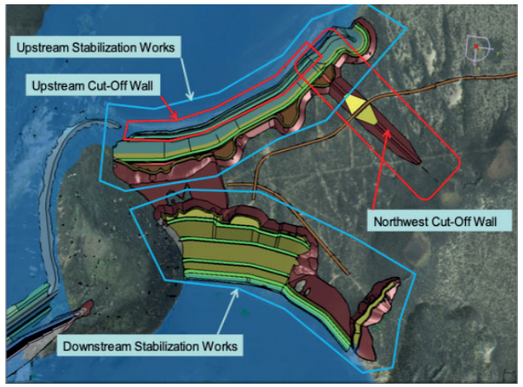

Figure 13: North Spur design

Figure 14: Upstream view of complete North Spur (2018)

Figure 15: Downstream view of complete works (2018)

3. Transmission Assets

The transmission project components are used to carry power from Muskrat Falls and from the existing Churchill Falls generating facility in Labrador. This consists of the Labrador Transmission Assets, which are high voltage AC transmission (HVAC) and the Labrador-Island Transmission Link, which is a high voltage DC transmission (HVDC) system. The construction of these assets was completed in 2017 with the majority of these assets energised in 2018. Initial power from Churchill Falls was delivered to the island in June 2018; commissioning and testing of the transmission infrastructure is ongoing.

The Labrador Transmission Assets (HVAC) consists of the following:

- Two 250 km, 315 kV transmission lines between Muskrat Falls and Churchill Falls, and HVAC sites at Churchill Falls and Muskrat Falls.
- The Labrador-Island Transmission Link (HVDC) consists of the following:
- 1,100 km, 900 MW line between Muskrat Falls and Soldiers Pond (Figure 16),
- Converter station at Muskrat Falls and Soldiers Pond; switchyard and synchronous condenser at Soldiers Pond,
- Strait of Belle Isle Marine Crossing,
- Transition compounds at Forteau Point and Shoal Cove, and
- Grounding stations at L'Anse au Diable and Dowden's Point.

Figure 16: HVDC transmission tower

4. Construction Milestones and Challenges

The major challenge of working in a northern environment is the extreme temperatures and the short construction season (Snyder and Barnes 2013). At Muskrat Falls, temperatures may reach over 30ºC in summer and lower than -30ºC in winter; the construction season is very short as a consequence (Figure 17), this necessitates careful planning to optimise the work done in the summer season, and require heating and hoarding to allow construction to continue through the winter period (Figure 18).

At Muskrat Falls, there was the additional challenge from the Churchill River. A major ice dam occurred there every year, which caused very high water levels, and backwater into the construction area (Snyder and Turpin 2014). This dictated the heights of the cofferdams and required development of methods to handle the ice buildup and mitigate its effect to allow construction to proceed (Figure 19) (Damov et al. 2018).

By the summer of 2019, all of these challenges were met and the major civil construction milestones completed. This includes the following:

- All dams complete – North, South, North Spur and Transition Dams
- Spillway complete and river diverted
- Intake channel and tailrace channel watered up
- All concrete poured in the Powerhouse
- All gates and guides installed in the Intake
- Impoundment of the reservoir underway

Work continues inside the powerhouse with the installation of the turbine-generator units and work on completion of the balance of plant work for power from the first unit was completed in early 2020 with power from the four units anticipated by the end of 2020.

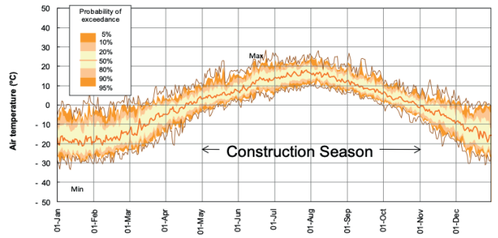

Figure 17: Construction season at Muskrat Falls

Figure 18: Intake construction - Winter 2015 - 2016

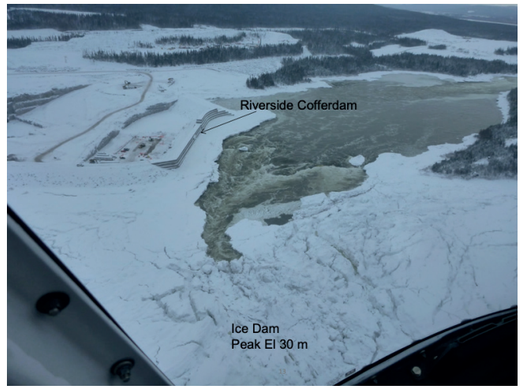

Figure 19: Hanging ice dam at Muskrat Falls (January 2016)

5. Conclusions

Major construction of the Muskrat Falls generating facility commenced in early 2013 with the Bulk Excavation contract. As of Spring 2020, the balance of plant work was nearing completion and commissioning of Unit 1 was well underway with first power anticipated mid-2020. This paper has provided an overview of the facility and an update on the construction of the Muskrat Falls project which is underway in the harsh northern environment of Labrador.

Acknowledgements

This paper was originally presented at the Canadian Dam Association (CDA) Conference & Exhibition, October 6-10, 2019, Calgary, Alberta.

References

Protulipac, D., T. Smith and G. Snyder, “Muskrat Falls Dams – Cold Climate Considerations in Design and Construction.”, Canadian Dam Association Annual Conference, Quebec City, QC. October 15-17, 2018.

Ceballos, A., G. Snyder and R. Bouchard, “Stabilization of the North Spur at Muskrat Falls: An Overview”. Canadian Dam Association Annual Conference, Mississauga, ON., October 5-8, 2015.

Bouchard, R., A. Rattue, J. Reid and G. Snyder, “The North Spur Story: Two Years Later.”, Proceedings of 2019 International Commission on Large Dams (ICOLD-CIGB) Symposium, Ottawa, ON.

Snyder, G. and B. Barnes, “The Muskrat Falls Hydroelectric Development: Challenges in a Northern Climate”, Canadian Dam Association Annual Conference, Montreal, QC., October 5-10, 2013.

Snyder, G. and M. Turpin, “Selection, Design and Construction of the Muskrat Falls Riverside Cofferdam.”, Canadian Dam Association Annual Conference. Banff, AB. October 4-9, 2014.

Damov, D., J. Groeneveld, G. Saunders, C. McLean and G. Snyder, “Muskrat Falls River Ice Management During Construction: From Design to Implementation”, Canadian Dam Association Annual Conference, Quebec City, QC. October 15-17, 2018.

Modelling Fleet Performance Over Complex Operating Scenarios

Iain Davison MSc, BSc, MMath, MIMA, MSaRS

Chartered Mathematician
Principal Consultant,
Aerospace, Defence, Security & Technology Engineering, Design and Project Management
Aldershot, UK.

Abstract

The Systems Availability Model (SAM) is a program designed to assess the Availability, Reliability and Maintainability (AR&M) characteristics of multiple systems used over operating scenarios that place varying demands upon those systems, such as that encountered in complex military, commercial shipping, industrial installations and deployed systems of systems.

The unique ability of SAM to overlay system dependencies onto complex mission profiles makes it a uniquely powerful and flexible AR&M modelling tool. Mission profiles are built up from a variety of activities, each demanding use of different combinations of equipment, rather than a fixed time at risk approach adopted by many simpler modelling tools.

This paper discusses:

- The unique capabilities of SAM and, at a high level, how a SAM model is developed and its cross-industry applications;
- The use of SAM to set system/equipment requirements, and understand the impact of equipment reliability on a fleet of ships undergoing complex operating scenarios;
- Reflecting changes to mission requirements, and the knock-on effect of predicted performance;
- How SAM can be used to understand the significance of individual systems during safety critical activities (e.g. replenishment at sea, close water navigation).

Keywords

Availability; Reliability; Maintainability; Modelling; Asset Management

1. Introduction

The purpose of this paper is to discuss the role of Availability, Reliability and Maintainability (AR&M) modelling through the life cycle of complex systems or fleets of equipment. Specifically the paper considers the good practice of modelling of multiple systems used over operating scenarios that place varying demands upon those systems, such as that encountered in complex military, commercial shipping, industrial installations and deployed systems of systems.

The paper discusses the role of modelling in setting of equipment end-user/system/equipment requirements, and understanding the impact of equipment reliability on a complex system or fleet undergoing complex operating scenarios and how the features of the Systems Availability Model (SAM) lend it to support such activities. The role of modelling in the subsequent management of project risk is then discussed with emphasis on two key areas:

- The importance of reflecting changes to mission requirements, and the knock-on effect of predicted performance; and
- The importance of understanding the significance of individual functions or sub-systems (e.g. during safety critical activities such as replenishment at sea, close water navigation).

A final section to the paper is provided that summarises the unique capabilities of SAM that allow it to support the above and, at a high level, how a SAM model is developed and its cross-industry applications.

Although this paper refers to methodology specifically provided by SAM, it should be noted that other commercially available tools can be employed to provide similar methodology and benefits.

2. What Is SAM?

The SAM is a program designed to assess the AR&M characteristics of multiple systems used over operating scenarios that place varying demands upon those systems, such as that encountered in complex military, industrial installations and deployed systems of systems.

The unique ability of SAM to overlay system dependencies onto complex mission profiles makes it a powerful and flexible AR&M modelling tool. Mission profiles are built up from a variety of activities, each demanding use of different combinations of equipment, rather than a fixed time at risk approach adopted by many simpler modelling tools.

SAM is a UK Ministry of Defence (MOD) owned tool, managed and supported by Atkins, issued without charge to UK MOD Projects, and is commercially available to anyone else.

SAM is designed to provide AR&M predictions for single systems or groups of interdependent systems operating over a mission.

SAM was initially developed for the MOD to depict the interactions between a ship's systems (weapons, power distribution, sensors, propulsion, etc.) in the various roles a ship may be required to undertake. For example, Figure 1 presents a representation of how multiple power requirements for a ship can be modelled in SAM. However, successful developments have extended the capabilities of SAM and it is now capable of modelling any system, process plant or engineering installation.

SAM is designed to be a flexible program capable of assessing a variety of systems (including interdependent systems) of mixed repairable and non-repairable equipment, including those with active or standby redundancy. It includes the capability to model first line (local) and second line logistic delays and maintainer availability.

3. Setting of Requirements

3.1. Introduction

As described in the Part B Chapter 2 of the Applied R&M Manual for Defence Systems (referred to as GR-77) [1], the achievement of AR&M in service stems from either luck or a clear, appropriate and realistic specification of the requirements together with a contract that enforces adherence.

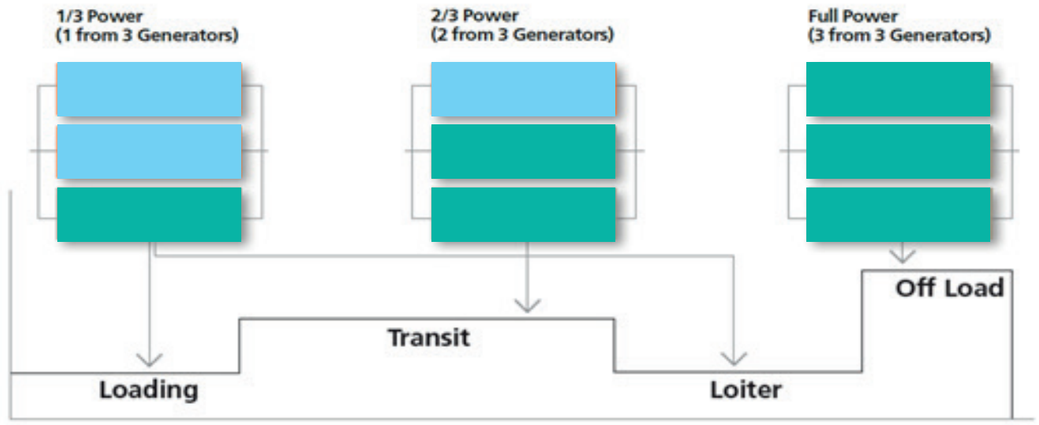

Figure 1: Modelling multiple power requirements

The Safety and Reliability Society (SaRS) aims to provide an evolving body of knowledge for professionals. GR77 is a web-based resource in the body of knowledge that provides technical AR&M guidance on a wide range of topics under the headings of “General Guidance”, “R&M Related Activities”, “R&M Related Techniques”, “Supporting Theory”, etc.

AR&M requirements and their traceability to definitions, assumptions and lower level requirements or constraints can be problematic, particularly where there is significant change in the technical requirements or frequent changes in project personnel. This lack of traceability can result in shortcomings in the AR&M requirements and contractual requirements, which in turn may compromise capability and escalate through life costs.

Part B Chapter 2 of GR-77 [1], provides guidance on the methods available to setting AR&M requirements and maintaining their traceability. In particular, where equipment end-user requirements are satisfied by a number of system level requirements, it is not always clear to the equipment end-user which of the many AR&M related attributes are required at the concept stage of a project. GR-77 [1] advocates the use of scenario analysis supported by AR&M modelling or analysis to help identify AR&M attributes critical to mission success. The subsequent sections describe how AR&M modelling tools and techniques may be used to aid the development of equipment end-user requirements, apportionment to system level requirements, and demonstrating the linkage between them.

3.2. Equipment End-User Requirements

3.2.1. Initial Model Creation

As described in Appendix A, a SAM model is built from the bottom up (i.e. beginning with defining equipment/components, then moving on major functions and a mission profile). However, since equipment end-user requirements are defined at a high level (e.g. availability of a fleet of assets), when developing a model to define or validate the requirements it can be useful to initially apply a more top-down approach.

Through engagement with equipment end-users and other key stakeholders, the mission profile for a fleet of assets should be developed. Initially, this may simply be expressed as general periods of “Activity” and “Non-activity”, for each asset. Through continued engagement, the profile should be developed to include more specific activities (typically categorised as mission essential, critical and non-critical events), which can eventually be linked to the major functions performed by each asset.

A useful way of visually representing this linkage between activity and major function is through a criticality matrix. It is recommended that the classification descriptors used in a criticality matrix should be developed on a project-by-project basis to allow specific project nuances to be considered. Figure 2 shows an example criticality matrix employing the following descriptors:

- Desirable (D), i.e. the function is desired for the mission, but is not required for mission success;
- Mission (M), i.e. the function is required for mission success;
- Critical (C), i.e. the function is critical to both mission success and the wider asset performance (potentially safety related).

	Activity 1	*Activity 2*	*Activity 3*	*...*	*Activity Z*
Major Function 1	-	D	M		-
Major Function 2	C	D	M		C
Major Function 3	M	D	M		M
...					
Major Function Y	D	C	-		-

Figure 2: Example criticality matrix (Major Function vs Activity)

This criticality matrix is intended to show the direct link between the major functions and activities. In reality, further subtleties may exist in relation to reversionary modes of operation and the assessment of criticality (D, M or C). For example, “Major Function 1” may be achieved by three different modes of operation, represented by the reliability block diagrams shown in Figure 3. As such, the criticality matrix may be further developed to articulate how critical each mode of operation is for each activity, as shown in Figure 4.

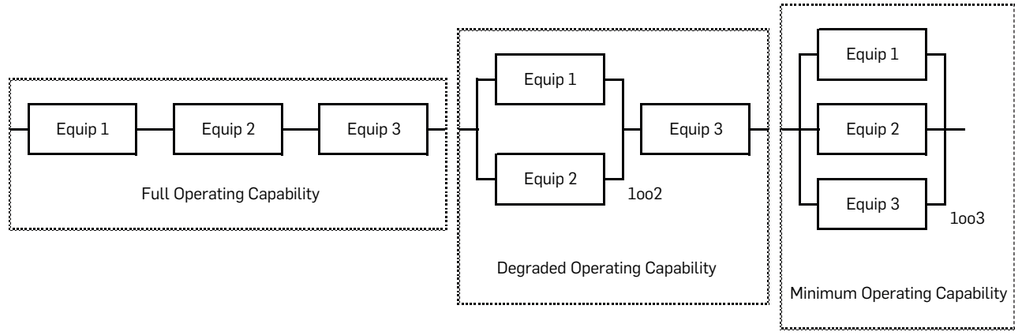

Figure 3: Example modes of operation

	Activity 1	*Activity 2*	*Activity 3*	*...*	*Activity Z*
Major Function 1:					
Full Operating Capability	-	*D*	*D*		-
Degraded Operating Capability	-	*D*	*M*		-
Minimum Operating Capability	-	*M*	-		-
Major Function 2	C	D	M		C
Major Function 3	M	D	M		M
...					
Major Function Y	D	C	-		-

Figure 4: Example criticality matrix (Modes of Operation vs Activity)

The key systems and sub-systems required to perform each major function can then be determined and defined at a level appropriate to the stage of the project. For example, during concept phase, details of an asset may only be described at a high level, such as “Propulsion”, “Communications”, etc.

Once these attributes have been determined, a SAM model can be created and populated in the traditional sense, from the bottom up (also see Appendix A) for details of how to construct a SAM model):

- Key systems and sub-systems populated into a SAM Model Equipment List (MEL); initially with dummy reliability and maintainability data, to be populated later;
- Functions built up of the key systems and sub-systems into a SAM Availability Dependency Chart (ADC);
- Activities built up from functions and formed into mission profile(s) into a SAM Mission Profile Chart (MPC).

3.2.2. Development of Reliability and Maintainability Model Data

The generation and sourcing of reliability and maintainability data of suitable provenance is generally one of the more challenging activities in the creation of an AR&M model. Since details of the asset are likely to be limited at the early stages of a project, the best source of reliability and maintainability data is expected to be from the in-service experience of existing similar assets. Furthermore, a common equipment end-user request is that a new asset is no less reliable than an existing asset; understanding the performance of the existing asset is therefore key to defining equipment end-user requirements.

In an ideal world, this in-service performance would be based on fully traceable data including details of usage, environment and from a statistically significant sample size over a number of years, which can be fully interrogated. However in reality, this data may be patchy at best, and as such the experience of the equipment end-users should be used to validate any reliability and maintainability data gleaned. It is important for the validation exercise that data is presented in a form that equipment end-users can relate to and can understand. For example, rather than presenting the reliability of an asset function as a Mean Time Between Failure (MTBF) or failure rate per million hours, the equipment end-user may relate better to an expected number of failures per annum or failures per mission.

Once reliability and maintainability data for each key system or sub-system is developed, it can be populated into the SAM model. In order to articulate an equipment end-user requirement, it may also be necessary to reflect the expected support structure into the AR&M metrics. In the concept phase, this may be represented more simply as a probability of spare being available, and a logistic delay time.

As shown in Figure 6, SAM is capable of providing a number of outputs and metrics including availability, which is considered the most appropriate for defining equipment end-user requirements.

3.2.3. Model Sensitivity Analysis

Arguably, the main benefit in employing a modelling tool, such as SAM, to define requirements is the ability to perform sensitivity and "what if" analysis. This allows the equipment end-user to gain an understanding of the impact of decisions on the overall AR&M performance of an asset and hence where areas of risk reside. In particular, during the early project phases it may be common to assess the impact of changes in (where applicable) fleet size, asset functionality and mission profile, on modelling results.

Before undertaking sensitivity analysis, it may be beneficial to present the initial modelling results to the equipment end-users and all stakeholders. This allows a level of validation and managing of expectations against "gut-feel". At this point it is also advisable to highlight any particular areas of uncertainty and the modelling features (e.g. system reliability, asset architecture, mission profile, etc.) driving the initial results. The various outputs of SAM, as discussed in Appendix A, can be used by the modeller to investigate the drivers of unreliability/unavailability.

The particular areas to be assessed in sensitivity and "what if" analysis should be discussed and agreed with the equipment end-user and stakeholders, based on the areas of risk and uncertainty. It is useful to document this in the form of a plan, particularly where multiple parameters are requested to be investigated, to ensure a logical and structured approach is maintained. Results from each sensitivity case can be presented together with the baseline initial results and discussed with the equipment end-user, such that they get an appreciation of how various decisions can influence the AR&M metrics.

3.2.4. Setting Equipment End-User Requirements

Results from the SAM modelling activity can be used to set or validate equipment end-user AR&M requirements for a project.

If the equipment end-user requirements have already been defined (for example derived from an existing asset), comparing these requirements with results from the SAM model gives a measure of confidence that the metrics are realistic and achievable, based on the model inputs provided. Differences[1] between the SAM model results and defined equipment end-user requirements should be investigated to understand the reasons and their significance. If the difference is relatively small and can be reduced by slight adjustments to the model input data (e.g. system/sub-system reliability and maintainability data, or mission profile), little or no change to the equipment end-user requirements is probably necessary. However, the nature of the difference should be discussed and agreed with the equipment end-user and stakeholders.

If there is a more significant difference between the SAM modelling results and equipment end-user requirements, the basis of equipment end-user requirements should be compared with the basis of the SAM model to understand if there are any fundamental reasons why the results should differ. If the two are based on similar foundations, further interrogation of the model will be required to gain an understanding of the source of the difference. Once established, the reason(s) for the significant difference should be discussed with the equipment end-user and stakeholders to agree whether changes to the SAM model are required, and whether the SAM modelling results should be used to update the equipment end-user AR&M requirements. Of course, it may be the case that the equipment end-user requirements remain unchanged due to a higher-level operational requirement. If this is the case, then the SAM model can be used to derive system requirements necessary to achieve the equipment end-user requirements, as discussed in Section 3.3.

Where the equipment end-user requirements have yet to be defined, the results from the SAM model can be employed to do so, providing confidence that, based on the given input, the metrics are realistic and achievable.

In both cases (setting or validating equipment end-user requirements), sensitivity analysis is an important activity, providing the equipment end-user with an appreciation of the limitations of the equipment end-user requirements and how changes to the model inputs can affect the AR&M metrics. This should be taken into consideration when defining the equipment end-user requirements, particularly in areas where there remains significant uncertainty (e.g. asset functions, or mission profile).

3.3. System Requirements

Once a SAM model has been created to either set or validate the equipment end-user AR&M requirements it can be used directly to derive system requirements. As the SAM model has been built up from key functions, systems and sub-systems, the AR&M metrics for each can be extracted directly from the SAM model results and used to form the system requirements.

The advantage of this approach is that it provides a clear linkage between equipment end-user and system requirements; meeting system requirements ensures that the equipment end-user requirements are also achieved.

The level at which the system requirements are presented is likely to depend on contractual arrangements. For example, if it is expected that a single supplier is responsible for the complete asset, the system requirements may be presented at a relatively high level, leaving the supplier responsible for further apportioning these to lower-level sub-system suppliers. If, however, it is expected that the project will be contracted to multiple suppliers, the level at which the system requirements are articulated should reflect this.

Linked with the development of system requirements is the opportunity to set up the contracted method for monitoring in-service AR&M performance and, in particular, Key Performance Indicators (KPI) and metrics specific to the project, which can be developed from and assessed against the SAM model. GR-77 Part B Chapter 2 [1] discusses various types of AR&M metrics, which may be employed when setting system requirements and KPIs. The pros and cons of the various metrics should be discussed with the equipment end-user and stakeholders to determine the most appropriate AR&M metrics to be used. Once decided upon, SAM's flexibility allows the model results to be presented in the required form, for use in setting system requirements. Metrics that can be derived from a SAM model include (but are not limited to):

- Availability – Operational or intrinsic availability (of a fleet, individual assets, systems, sub-systems, etc.).
- Probability of failure over a given period – Reliability; Basic/logistic reliability; Non-repairable at sea reliability; Mission reliability.
- Rate of failures of period between failures – Mean variate (Footnote 2) between failures; Mean variate between mission failures; Characteristic life.
- Maintenance performance – Active Repair Time (ART); ART per operating hour; Mean Time To Repair (MTTR); False alarm rate; Total corrective maintenance time.
- Cost of ownership (Footnote 3) – Labour; Spares and materials costs associated with failures.
- Others – Failure free operating period.

3.4. Supporting the Initial R&M Case

Def Stan 00-42 Part 3 [2] and BS EN 62741 [3] provide a description of the principles of progressive assurance, with the former reflecting specifically the current policy within UK defence acquisition. Both standards provide guidance on the content and the ownership of the R&M (Footnote 4) case through the life of a system, and advocate the creation of an "Initial R&M Case Report" in order to capture fully the AR&M requirements and areas of AR&M related risks.

The SAM modelling activities discussed above support the development of such an Initial R&M Case Report during the concept and assessment phases, by:

- Providing full traceability of requirements, through documentation of the SAM model input data (e.g. Mission profiles, major functions, equipment AR&M data and sources), assumptions and stakeholder decisions;
- Demonstrating the link between equipment end-user and System Requirements, by documenting the modelling approach undertaken to generate the requirements; and
- Aiding in the identification of areas of risk, through sensitivity analysis as described in the sections above.

4. Managing Risk With SAM

4.1. Progressive Assurance

As quoted in Part B of GR-77 [2]:

"AR&M is built into a system at the design stage. No amount of analysis or testing can improve a design without a costly revisit to the design stage. The use of good design practice for high reliability and good field maintainability (in software and hardware) is an essential component of reducing project risk and achieving good products."

It is therefore essential to initiate the AR&M programme early in a project design/development phase.

Assurance that a developed solution satisfies the defined AR&M requirements is generally the responsibility of the contractor, where any modelling activities may be performed using commercially available or bespoke

1 Due to inherent uncertainty in reliability data, and the Monte Carlo simulation techniques employed by SAM, it is considered highly unlikely that the SAM model results will match the derived equipment end-user requirements exactly – unless, of course, the SAM model results have been used to derive the requirements.

2. Typically, the variate is expressed as time (i.e. MTBF) or miles.
3. Cost of ownership can be determined by analysing outputs from SAM, rather than directly from a SAM model.
4. Note, BS EN 62741 [2] refers to dependability case, rather than R&M case, but is in essence the same for the purposes of this paper.

modelling tools (for example, RAM4, which is also free to use for MOD projects, or SAM).

These assurance activities should be initiated as early as possible in order to influence design activities, and identify areas of risk and opportunities for improvement. Progressive assurance is intended to provide the contracting project/delivery team with regular updates of predicted performance, areas of risk and potential for trade-off.

By maintaining and updating the SAM model developed to set the requirements, the project/delivery team can use the information provided by the contractor to:

- Investigate the impact of predicted performance and risk areas on fleet level metrics and the equipment end-user requirements;
- Assess design options and perform trade off studies against the fleet level requirements.
- Throughout the project design/development phase, the way in which the equipment or fleet is to be used may be subject to changes driven by the equipment end-user, the project/delivery team, and/or the contractor's engineered solution, such as:
- Changes in how and where the equipment or fleet is to be operated may affect the mission profile, usage and environment.
- Changes in how the equipment or fleet is supported may affect spares holdings, logistic delay times and as such equipment repair times. This may also ultimately affect the mission profile of a fleet, if it cannot be supported appropriately.

Reflecting these changes in the SAM model, as they arise, allows the project/delivery team to assess the impact on the fleet performance and AR&M requirements. It also enables them to understand the drivers of fleet unavailability/unreliability, for example specific mission activities, equipment and/or their functions. Therefore, through regular review of the AR&M development progress, the project/delivery team can better understand and manage the risks associated with achieving the system and equipment end-user requirements throughout the project design/development phase. This is key to the successful delivery of a project.

4.2. Assessing System or Function Significance

The development of a criticality matrix to create a SAM model, as described in Section 3.2.1, allows the significance of individual functions or sub-systems to be analysed and therefore used in the management of project risk.

Varying of the model input parameters (reliability and maintainability data, or details of the mission profiles), through sensitivity analysis, can be used to identify those functions and hence sub-systems or equipment which have the greatest impact on overall fleet performance or the performance of critical functions (e.g. safety critical activities such as replenishment at sea or close water navigation). As such, those model input parameters, which have the greatest impact on performance, can then be the focus of assurance activities (as described above) as part of a risk-based approach.

4.3. Validating Spares Recommendations

Many projects require the contractor to provide a list of recommended spares to support their equipment during a pre-defined mission duration. These lists typically comprise three elements:

- The list of consumable items, which can be estimated from contractor and equipment end-user experience of attrition rates in service;
- The list of spares required to support scheduled maintenance activities, which can be developed from the details of each maintenance activity.
- The list of spares required to support corrective maintenance activities when components fail. Deciding which spares to take on a mission, to cover component failures, should be based on an understanding of the risk to mission success. Spares modelling tools, used to provide these recommendations, typically take account of system architecture, equipment reliability, and cost of spares to calculate the most cost effective solution to meet a target metric (e.g. operational availability of a system) over the mission duration. However, these tools may not be able to reflect a complex mission profile for a fleet of assets, where different equipment functions are required for different phases of the mission, and in particular, where the system architecture (required for mission success) may change over time; this is where SAM can be used to validate any spares recommendation.

It is important to note that SAM is not designed to provide a spares recommendation; instead, as discussed in Appendix A, the MEL includes the quantity of spares supporting each item modelled. By including the list of recommended spares into the developed SAM model, undertaking sensitivity analysis, and interrogating the SAM outputs, it is possible to validate the spares recommendation against achieving the mission profile. This can include identifying any shortfalls in sparing, or where the number of spares has a lesser impact on mission success (for example, because a system function is only required for short period of the mission).

The results from the SAM model can then be used to influence the decision on type, quantity and location of spares required to support a mission. Moreover, as mission requirements change, the SAM model can be adapted accordingly to allow the project/delivery team to understand the impact on sparing requirements.

Finally, feeding experience from in-service back into the models (spares model and SAM) is key to validating the approach and providing better estimations in the future.

4.4. Supporting System Acceptance

The concept of a digital twin can be defined as a digital replica of physical assets, which can be used to optimise the operation and maintenance of physical assets or systems. In this way, the modelling approach described in this paper can act as a digital twin to a fleet of assets in relation to their AR&M performance. Clearly, the effectiveness of a digital twin is reliant on it reflecting reality; for an AR&M model, this includes incorporating in-service reliability and maintainability performance, and reflecting the system design, usage and mission profile.

At the end of a project design/development phase, the SAM model should reflect the detailed design, incorporate results from any reliability trials/tests, and importantly the AR&M-related risks should be well understood. Throughout the manufacturing/installation phase, the SAM model should be updated to reflect the final as-built designs, incorporating any design changes occurring during manufacture/installation. Furthermore, any defects or issues identified during manufacturing, which counter the claims presented in the R&M case report should be documented and reflected, as appropriate, into the SAM model.

The purpose of this is to provide input into the system acceptance activities to demonstrate that the system satisfies all AR&M requirements documented within the SRD and URD. As discussed in Section 3, the SAM model can be used to develop the project requirements; as such, the same "as-built" SAM model can be used to verify and validate the requirements, and support formal acceptance of the R&M Case.

Part of the verification and validation activity may include the collection of in-service performance data. In this case, the use of the SAM model allied to a rigorous approach to recording and sentencing data, (e.g. through a formal Data Reporting, Analysis and Corrective Action System (DRACAS)) should be planned for the early in service phase. This will allow the programme to focus upon reliability growth and the availability requirements rather than an artificial "demonstration" which places certain constraints, such as fixed build standard, upon the equipment supplier and the customer. The approach should employ suitable modelling tools, such as SAM, in order to ensure that a route to acceptance of the system, will actively involve both the project/delivery team and the equipment supplier at an early stage. The approach minimises the potential for dispute and ambiguity when dealing with the often-contentious issue of proving AR&M characteristics. Critically the method allows for a changing build standard, minimises the duration of the proving period and promotes a partnering approach to acceptance of the system AR&M characteristics.

The SAM model, reflecting the manufactured solution, can then be used to provide continued assurance, act as a digital twin, and support decision making during the in-service phase.

4.5. Reflecting Actual In-Service Performance

The primary reason for updating and maintaining the "as-built" SAM model during the in-service phase, is to incorporate in-service reliability and maintainability data, and reflect actual usage, to provide continued assurance against the equipment end-user requirements and specified project KPIs.

In addition to this, the SAM model can be used to:

- Assess the impact of proposed changes to system design, usage, and support structure, on the AR&M performance.
- Influence the development of AR&M requirements for new projects, by reporting on equipment, system and fleet level metrics.
- Aid in decision making to drive down cost of ownership. Although cost information is not directly included in the SAM model, the cost of ownership of a fleet of assets is dependent on a number of the factors represented within the SAM model, such as equipment/asset reliability, maintenance times, and usage and mission parameters. Through interrogation of the in-service SAM model, and combining these factors with actual costs it is possible for project/delivery teams to identify how the factors are influencing the total cost. This information can then be used to support options studies seeking to drive down the cost of ownership, and understanding the impact on fleet and asset AR&M performance: a key parameter to be considered in all options studies.

The R&M case is employed to provide progressive assurance of compliance against the AR&M requirements, and where not, a reasoned auditable argument is presented as to why not. The R&M case is developed through a risk-based approach.

Actual AR&M performance of a system is unknown (i.e. the risk that the system will not achieve its AR&M requirements is greatest) during the early phases of a project (concept/assessment and development phases). Modelling activities are used to predict the future performance of the system in order to reduce the risk to the project.

When the project enters the in-service phase, AR&M data should be collected and the actual in-service performance of the system incorporated into the "as-built" SAM model to assess performance against the AR&M requirements. However, the reliance on this data during the early in-services stages of the project, to provide assurance of the AR&M performance, should be limited due to the following reasons:

- The sample size of data from which to draw conclusions is initially small therefore there is uncertainty in the early data.
- The systems may be subject to early life failures as defective products are identified and discarded, and early sources of potential failure are surmounted.
- Operating and maintenance procedures may still be being established and honed (which may affect the AR&M performance of the system).

Initial in-service data should be used to identify areas for improvement within the design, and the predicted performance (from modelling activities) should be used to provide assurance. The statistical significance of the in-service data increases with the amount of time in service and the quantity of data collected, and the reliance on the predicted performance to provide assurance therefore decreases. This is illustrated in Figure 5.

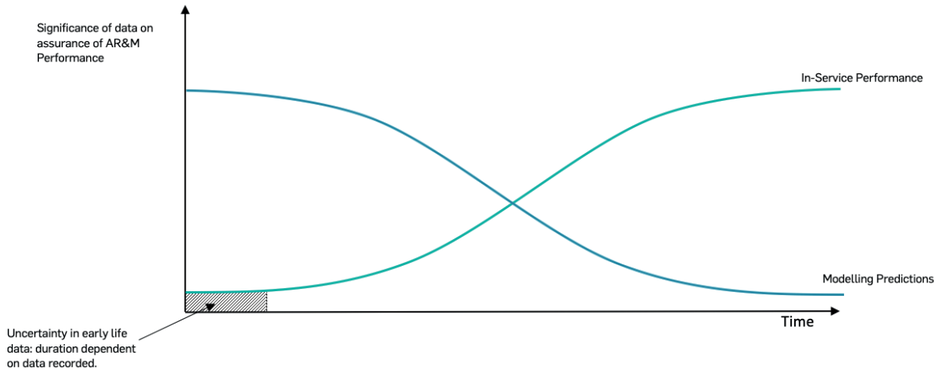

Figure 5: Significance of in-service performance and modelling predictions over time

5. Concluding Remarks

The British statistician, George E. P. Box famously wrote, in various books and papers, "All models are wrong, but some are useful". This has been borne out from my experience of over 12 years' modelling complex systems and managing AR&M software tools. As such, I felt it important to highlight guidance and tools that exists to provide valuable and insightful modelling, that helps set realistic requirements, and can be used to understand the risks of operating complex fleets of assets in service.

The modelling approach discussed within this paper can be employed as a manually updated digital twin to a fleet of assets, reflecting in-service performance. While it is unlikely that complex availability models can be automatically updated with reliability data in the short term, these models can (and should) be periodically reviewed and updated from in-service experience. This allows the models to be used to analyse the effect of changes in design and usage upon fleet level AR&M metrics and KPIs, before they are implemented – hence saving time and money.

Glossary of Terms

Acronym	Definition
ADC	Availability Dependency Chart
AR&M	Availability, Reliability and Maintainability
ART	Active Repair Time
Def Stan	Defence Standard
DRACAS	Data Reporting, Analysis and Corrective Action System
KPI	Key Performance Indicators
MART	Mean Active Repair Time
MEL	Model Equipment List
MOD	Ministry Of Defence
MPC	Mission Profile Chart
MTBF	Mean Time Between Failure
MTTR	Mean Time To Repair
R&M	Reliability and Maintainability
SAM	Systems Availability Model
SaRS	Safety and Reliability Society
SRD	System Requirements Document
URD	User Requirements Document

Acknowledgements

This paper was originally published in the Proceedings of Marine Electrical and Control Systems Safety Conference (MECSS 2019) as Davison, I. (2019). Modelling Fleet Performance over Complex Operating Scenarios. http://doi.org/10.24868/issn.2515-8198.2019.004.

References

1. Applied R&M Manual for Defence Systems, Part B - R&M Related Activities, Chapter 2 - R&M Performance Specification, Version 1.

2. Applied R&M Manual for Defence Systems, Part B - R&M Related Activities, Version 1.

3. BSI Standards Publication, BS EN 62741, Demonstration of dependability requirements - The dependability case, 2015.

4. Ministry of Defence, Defence Standard 00-42, Reliability and Maintainability Assurance Case, Part 3: R&M Case, Issue 5, May 2016.

Appendix A – SAM Details

General

As previously stated, SAM is a program designed to assess the AR&M characteristics of multiple systems used over operating scenarios that place varying demands upon those systems, such as that encountered in complex military, industrial installations and deployed systems or systems.

The flexibility of the program results from the assessment method utilised, which employs Monte Carlo simulation techniques. The system to be modelled is defined using three input screens known as “Charts”:

1. Model Equipment List (MEL)

The MEL breaks down equipments into component data (also, see note below). Component characteristics are defined by how often they fail (e.g. MTBF), and Equipment characteristics include repair and sparing requirements (e.g. Mean Active Repair Time (MART), and the probability that the component can be repaired during the mission).

2. Availability Dependency Chart (ADC)

The ADC assembles equipments (defined in terms of failure and repair data, which has been either transferred from the MEL or entered directly into the ADC) into major functions using dependency logic to allow for redundancy, where appropriate. An example a major function may be to “Provide Maximum Power”, which utilises 3 from 3 diesel generators.

3. Mission Profile Chart (MPC)

The MPC overlays the system dependency (in terms of major functions defined in the ADC) onto a set of activity types (e.g. ship transit) using a criticality matrix. This allows the combination of major functions to be defined for each activity type (e.g. the activity type “Ship Transit” requires the major function “Maximum Power”). Missions are then developed as a sequence of activities (made up from defined activity types) each lasting for a specific period. Failure of an activity results in the model entering a “Fallback Activity”, which is also defined in the MPC.

Note, although described in terms of “equipment” and “components”, the SAM model may be defined in terms of “system” and “sub-systems”, or any other combination of higher and lower level items deemed appropriate for the project stage and modelling purpose.

SAM performs rigorous data checks following the completion of each chart, and provides the SAM user with details of any errors that have been identified. Six types of output option are provided from the SAM simulation:

1. Input Data

Allows the chart data used to build the model to be examined.

2. Mission Definition

Allows the input parameters to the simulation to be examined.

3. Development Data

Allows data for each individual mission in the simulation to be examined.

4. Logistics

Used for investigating the allocation and effects of spares and repairs on the availability of a system, such as the number of failures, and spares required for particular equipments.

5. Reliability

Used for investigating the reliability of the system, major functions and activities. Also used to examine the end states for equipment and major functions.

6. Availability (Only Used for Availability Models - See Note Below)

Used for investigating the availability of the system and to determine the major function unavailability drivers. This output also examines the end states for equipment and major functions and outputs the instantaneous availability levels at mission end for selected functionality in the ADC.

Note: There are two types of SAM models:

a. Reliability models in which missions are terminated upon failure

b. Availability models in which fallback activities are used to monitor downtime in order to measure uptime and downtime over a mission period.

The process for creating and running a SAM model, as discussed above, is presented in Figure 6

Model Equipment List (MEL)

Equip 1 [Repair Data] built from:	**Equip 2 [Repair Data] built from:**	**Equip X [Repair Data] built from:**
Comp 1_1 [Failure, Sparing Data]	Comp 2_1 [Failure, Sparing Data]	Comp X_1 [Failure, Sparing Data]
Comp 1_2 [Failure, Sparing Data]	Comp 2_2 [Failure, Sparing Data]	Comp X_2 [Failure, Sparing Data]
-	-	-
-	-	-
Comp 1_n [Failure, Sparing Data]	Comp 2_n [Failure, Sparing Data]	Comp X_n [Failure, Sparing Data]

Notes: X = total number of Equipments / Comp X_n = n^{th} Component of Equipment X

MEL DATA CHECK

Availability Dependency Chart (ADC)

Major Func 1 [Logic] comprised of:	**Major Func 2 [Logic] comprised of:**	**Major Func Y [Logic] comprised of:**
Equip 1	Equip 1	Equip 1
Equip 2	Equip 2	Equip 2
-	-	-
-	-	-
Equip X	Equip X	Equip X

Notes: Y = total number of Major Functions / Each Equipment can be used in multiple Functions or only a single Function

ADC DATA CHECK

Mission Profile Chart (MPC)

Activity 1 [Duration] comprised of:	**Activity 2 [Duration] comprised of:**	**Activity Z [Duration] comprised of:**
Major Func 1	Major Func 1	Major Func 1
Major Func 2	Major Func 2	Major Func 2
-	-	-
-	-	-
Major Func X	Major Func X	Major Func X

Notes: Z = total number of Activities in a Mission / Each Major Function can be used in multiple Activities or only a single Activity

MPC DATA CHECK AND SIMULATION

Model Outputs (Report Generator)

Input Data	**Availability Outputs**	**Development Data**	**Mission Definition**	**Logistics Outputs**	**Reliability Outputs**

Figure 6: SAM Model Construction

Vitrification of Sellafield Wastes with High Metallic Magnesium Alloy Content

Keith S. Matlack
Wing K. Kot
Hao Gan
Ian L. Pegg

Vitreous State Laboratory,
The Catholic University of America
Washington, DC, USA

Bradley W. Bowan

Senior Vice President and Atkins Fellow
Nuclear
Columbia, MD, USA

Eric C. Smith

Senior Project Manager
Nuclear
Columbia, MD, USA

Innocent Joseph

Technical Director
Nuclear
Columbia, MD, USA

Sean P. Morgan

Robert Nichol
Sellafield Ltd, Sellafield,
Seascale, Cumbria, UK

Abstract

The Sellafield nuclear complex, located in northwest England, is the largest such site in the United Kingdom. Sellafield Limited, which is the operating contractor for the Nuclear Decommissioning Authority, is evaluating thermal treatment technologies for a potential future facility to process a variety of Intermediate-Level Waste sludges and slurries accumulated from historical site operations. In support of that effort, Atkins and the Vitreous State Laboratory (VSL) of The Catholic University of America conducted studies to evaluate the feasibility and implications of installing a joule-heated ceramic melter (JHCM) vitrification system to process a variety of sludge and slurry radioactive wastes at the Sellafield site. These sludges have the potential to contain a significant proportion of reactive metals in localized regions. The metallic fraction derives from unreacted Magnox spent fuel cladding. Thus, an important objective of this work was to investigate the performance of JHCM technology for the treatment of streams with localized regions of highly reactive metal contents.

Keywords

Waste Vitrification; Intermediate Level Radioactive Waste; Reactive Metal Waste; Waste Immobilisation

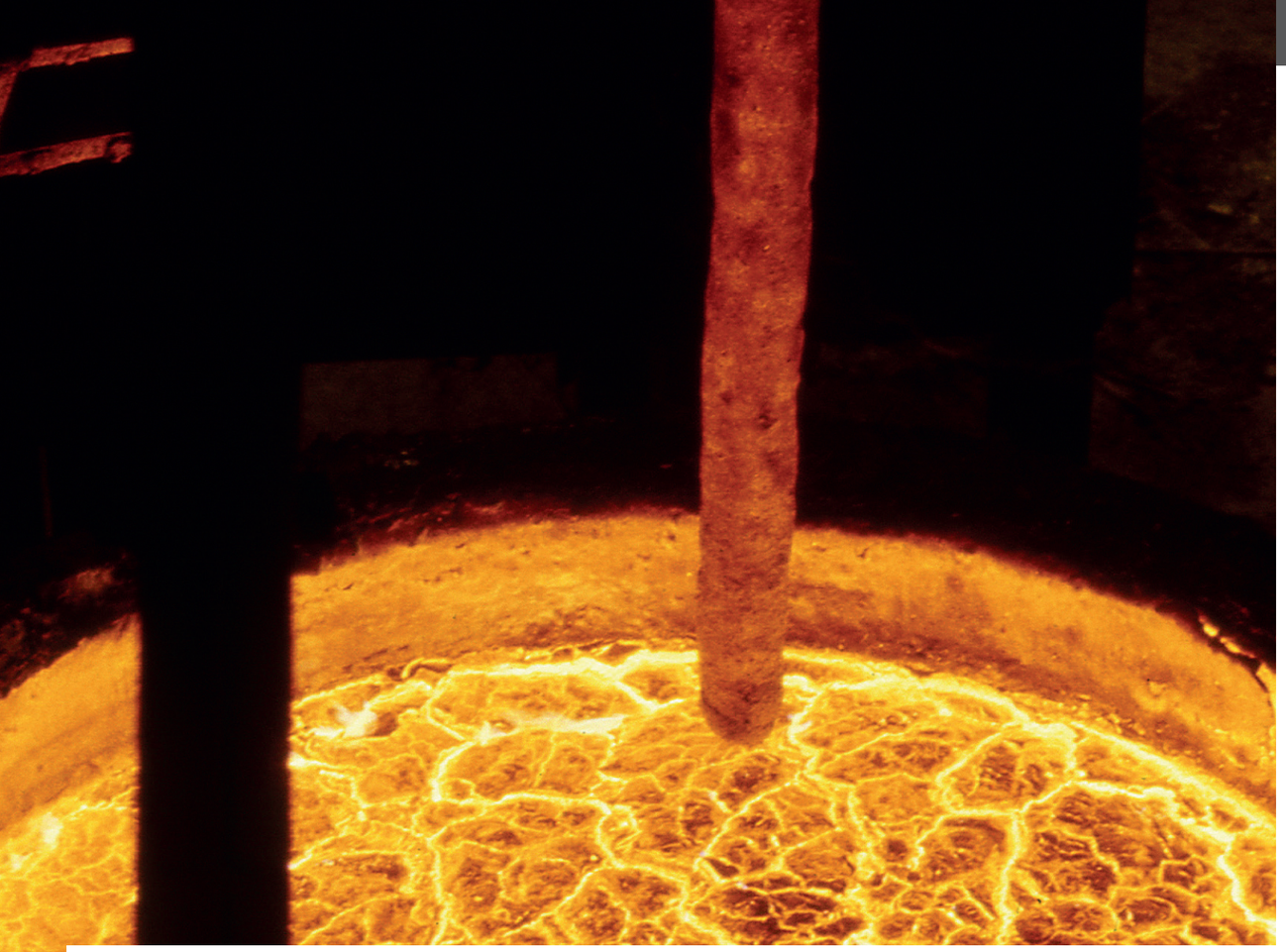

1. Introduction

The Sellafield nuclear complex, located in northwest England, is the largest such site in the United Kingdom. Sellafield Limited, which is the operating contractor for the Nuclear Decommissioning Authority, is evaluating thermal treatment technologies for a potential future facility to process a variety of Intermediate-Level Waste (ILW) sludges and slurries accumulated from historical site operations. Sellafield Limited sought bids for proof-of-concept trials in order to understand the plant and equipment required to thermally process a variety of Sellafield ILW feeds into Radioactive Waste Management Directorate (RWMD) compliant waste package forms [1]. Thermal treatment processes offer a potential alternative approach to the baseline techniques, such as grout encapsulation. The purpose of the trials was to gain confidence in the potential of the technology to treat a range of wastes. These wastes can be categorized radiologically as primarily ILW but also Low-Level Waste (LLW). The two physical/ chemical forms of these wastes selected for treatment trials are legacy Magnox sludges and a process waste consisting mostly of zeolite ion exchange media. The trials were intended to provide a scientific evaluation with particular attention to the issues around mass and activity balance and durability of the waste form. Atkins and the Vitreous State Laboratory (VSL) at The Catholic University of America (VSL) in Washington, DC performed thermal treatment trials on the two waste streams, SIXEP Magnox sludge and SIXEP sand/ clino, using the Joule Heated Ceramic Melter (JHCM) technology [2, 3].

In previous work for Sellafield Limited, Atkins and VSL developed and tested glass formulations for SIXEP Magnox sludges [2, 3]. These sludges have the potential to contain a significant proportion of reactive metals in localized regions arising from unreacted Magnox spent fuel cladding. Thus, the principal objective of the present work was to demonstrate and evaluate the performance of JHCM technology for the treatment of streams with high reactive metal contents. Therefore, the same waste simulant and glass formulations were employed but with partial replacement of the magnesium hydroxide with a metallic magnesium alloy. A commercially available Mg-Al alloy, Elecktron AZ31B, which has a nominal Mg content of 95.7% (3% Al, 1% Zn, 0.3 Mn), was used for this purpose. The testing was performed on a DuraMelter 10 (DM10) JHCM system to demonstrate processing of a simulated Sellafield waste stream containing a Mg alloy, characterize the melter exhaust, and determine the effects of Mg alloy particle size. This test platform has been extensively used to evaluate glass formulations and processing characteristics for a variety of HLW and LAW simulated waste streams for the U.S. Department of Energy [4-15].

Batches of the waste simulant were prepared with a metal loading equivalent to 15 wt% of the waste solids and combined with the glass forming chemicals required to produce the target product glass composition. The feed was delivered continuously to a DM10 JHCM system, which has a glass production rate of about 40 kg per day depending on the feed and operating conditions. Data on processing rate and any processing difficulties, off-gas composition, and system operating parameters, including flows, temperatures, pressures, etc., were collected. Product glass samples were inspected for the presence of any secondary phases, including metals. Results from tests using the Mg alloy as the primary magnesium source were compared to previous tests conducted with the same glass composition using magnesium hydroxide as the primary magnesium source to investigate the effect of the metallic alloy on the vitrification process.

2. Waste Composition, Glass Formulation, and Melter Feed

The composition of the Magnox sludge waste is given in the specification for the Sellafield thermal treatment development programme [1] and shown in Table 1. The most abundant waste components are uranium and magnesium with the other component oxides present at less than 5 wt%. Although uranium could be used in small-scale tests for glass formulation development, it needs to be substituted in waste simulants for larger-scale testing in order to reduce costs. Non-radioactive neodymium and zirconium are commonly used as surrogates for uranium. In the present case, since uranium is found at relatively high concentration and in order to simulate the behavior of trivalent and tetravalent oxidation states of uranium, both neodymium and zirconium were used as surrogates in the waste simulant. The substitution was made on a weight basis, with half of the uranium replaced by neodymium (by weight), and the other half by zirconium.

Table 1: Compositions of the Sellafield Magnox Sludge and Surrogates Identified for the Radioactive Components.

Waste Component	Concentration[1] (mg/ml or Bq/ml)	Oxide	Oxide wt%	Component/ Surrogate in Simulant
U	1.00E+02	U_3O_8	35.81%	Nd and Zr
Mg	9.70E+01	MgO	48.84%	Mg
Cl	8.20E+00	Cl	2.49%	Cl
Ca	8.00E+00	CaO	3.40%	Ca
K	6.00E+00	K2O	2.19%	K
Na	5.60E+00	Na_2O	2.29%	Na
Fe	3.10E+00	Fe_2O_3	1.35%	Fe
Al	2.90E+00	Al_2O_3	1.66%	Al

S	9.40E-01	SO_3	0.71%	S
Pb	6.20E-01	PbO	0.20%	Pb
Zn	5.20E-01	ZnO	0.20%	Zn
Cu	3.50E-01	CuO	0.13%	Cu
P	3.40E-01	P_2O_5	0.24%	P
Ba	3.20E-01	BaO	0.11%	Ba
Pu	2.90E-01	PuO_2	0.10%	See Below
Cr	2.50E-01	Cr_2O_3	0.11%	Cr
Ti	2.00E-01	TiO_2	0.10%	Ti
Ni	1.40E-01	NiO	0.05%	Ni
^{60}Co	1.60E+04	^{60}CoO	Negligible	Stable Co
^{90}Sr	3.00E+07	^{90}SrO	Negligible	Stable Sr
$^{95}Zr/^{95}Nb$	3.20E+04	$^{95}ZrO_2/^{95}Nb_2O_5$	Negligible	Stable Nb
^{99}Tc	6.30E+03	$^{99}Tc_2O_7$	Negligible	Stable Re
^{106}Ru	2.10E+05	$^{106}RuO_2$	Negligible	Not used
^{125}Sb	8.60E+04	$^{125}Sb_2O_3$	Negligible	Stable Sb
^{129}I	1.90E+01	$^{12}9I$	Negligible	Stable I
^{134}Cs	1.20E+05	$^{134}Cs_2O$	Negligible	Stable Cs
^{137}Cs	7.10E+06	$^{137}Cs_2O$	Negligible	Stable Cs
^{144}Ce	1.50E+05	$^{144}Ce_2O_3$	Negligible	Stable Ce
^{241}Pu	2.70E+07	$^{241}PuO_2$	Negligible	Stable Hf
^{241}Am	1.20E+06	$^{241}Am_2O_3$	Negligible	Stable Eu

[1] Concentration unit for major components = mg/ml wet sludge, for negligible (by weight) radionuclides = Bq/ml wet sludge.

Other radionuclides are present typically at sub-microgram levels (per ml of wet sludge) and are consequently negligible on a weight basis. However, in order to demonstrate the effectiveness of vitrification in immobilizing these elements, they need to be included in the simulant to be used in melter tests. For elements that do not have stable isotopes, the following surrogates were used: rhenium for technetium; hafnium for plutonium (cerium is a commonly used surrogate for plutonium but is used presently to replace ^{144}Ce); and europium for americium. Ruthenium was not included for cost reasons. Further, the concentrations of the surrogates are increased in the simulated waste for analysis purpose. Specifically, they are spiked at levels such that they are present in the final glass product at 0.1 wt%, with the assumption that they are completely retained in glass at a waste loading of 50%. The spike levels were adjusted subsequently according to the actual waste loadings. In formulating waste simulants for the melter tests, minor components are omitted to maintain a manageable number of analytes. Components that are present at < 0.5 wt% (oxide basis) in the waste were excluded from the present testing, with the exception of lead, chromium, and nickel — these metals are included so that their immobilization in glass can be evaluated. These three metals are each spiked at a concentration of 1.0 wt% (oxide basis).

A glass was formulated for the Magnox waste stream, UK-Mg-7 [2, 3], with a waste loading of 35 wt%, moderate leach resistance, acceptable processing properties, and acceptable crystallinity. Glass formulation for Sellafield Magnox sludge is limited by crystallization of forsterite (Mg_2SiO_4) and glass durability, as measured by PCT for the present purposes. Glass forming additives that would suppress crystallization from a glass melt tend to degrade the leach resistance of the glass under PCT condition, hence the 35 wt% waste loading. TCLP releases of UK-Mg-7 are acceptable by U.S. EPA regulatory standards (the U.S. TCLP and PCT requirements were used in lieu of RWMD requirements, which have not yet been defined). The viscosity and electrical conductivity at glass melt temperatures are within ranges for JHCM operation. The glass composition was further validated by the production of about 70 kg of this glass through the DM10 with the product being fully characterized and determined to be within acceptable performance parameters [2, 3].

Feed for melter testing was generated by blending the Magnox simulated waste and a magnesium alloy powder as a source for magnesium at a concentration equivalent to 15 wt% of waste solids with glass forming additives targeting the UK-Mg-7 glass composition. The alloy with the highest magnesium content available for testing was Elektron AZ213B with a nominal magnesium content of 95.7 wt%, 3 wt% aluminum, 1 wt% zinc, and 0.3 wt% manganese. This material was available in three size ranges. However, sufficient amounts for sustained melter testing were available only in the 80 to 18 mesh size range (0.18 – 1 mm). Given this availability, a large batch sufficient for producing 20 kg of glass was blended with the 80 to 18 mesh size magnesium alloy for a longer test of at least 8 hours and smaller batches were prepared with the other mesh sizes to evaluate the effect of particle size. The glass-forming chemicals used were borax, sodium carbonate, silica, and aluminum hydroxide. Changes made to the feed previously used [2, 3] were: Elecktron Mg alloy used for Mg source in place of $Mg(OH)_2$ at an amount equivalent to 15 wt% of waste solids, all Nd in feed as Nd2O3 with no $Nd(NO_3)_{3.5}H_2O$ in feed, Al_2O_3 omitted from waste, aluminum in Mg metal alloy accounted for, omission of $Eu(NO_3)3.6H_2O$ from feed, and addition of concentrated nitric acid and water to achieve a pH of 7 prior to the addition of the Mg metal alloy.

Prior to blending the feed batches used for melter testing, several small feed batches of a few hundred grams each were blended to evaluate the potential for hydrogen generation and gross rheological properties. Feed that was not neutralized with nitric acid prior to the addition of the magnesium metal alloy evolved sufficient hydrogen to exceed the flammability limit in the container head space immediately after the addition of the magnesium metal alloy. The feed continued to bubble and evolve hydrogen over the next day until the feed became very viscous. The viscous slurry was similar to that formed from the Magnox sludge with magnesium hydroxide as the primary magnesium source. This indicates that the metal alloy fully converted to magnesium hydroxide shortly after the addition of the magnesium metal alloy. In subsequent small feed batches, the pH was lowered to 7 with the addition of nitric acid prior to the addition of the magnesium alloy. Hydrogen was still generated from these batches but at a much slower rate. Furthermore, the residual reactions did not result in the formation of a viscous slurry after several days. Based on these observations, all feeds prepared for melter tests were neutralized to pH 7 prior to the addition of the magnesium metal alloy, which was added to the batch immediately prior to the start of each test. The addition of nitric acid to the feed has the added benefit of introducing oxidants to the feed to balance the reducing effects of the magnesium metal alloy.

3. Melter Operations

Melter testing was conducted with the DM10 unit, which is a ceramic refractory-lined melter fitted with two Inconel 690 plate electrodes that are used for joule-heating of the glass pool and a bubbler for stirring the melt. The glass product was removed from the melter by means of an air-lift discharge system. The DM10 unit has a melt surface area of 0.021 m2 and a glass inventory of about 8 kg. The melter feed was introduced in batches into a feed container that is mounted on a load cell for weight monitoring. The feed was constantly recirculated providing continuous mixing and introduced into the melter by means of a peristaltic pump through a Teflon-lined feed line and water-cooled, vertical feed tube. In each test, the melter was fed to cold-cap-limited conditions while data were collected on feed and glass processing including extensive visual and video observations of the cold cap. Over 41 kg of melter feed containing more than 1 kg of magnesium metal alloy was processed through the melter generating 15.5 kg of glass in these tests.

All tests were conducted targeting the same glass composition at waste loading of 35 wt% on an oxide basis. The tests also employed the same glass former additives, magnesium metal alloy content targeting 15 wt% of waste solids, 1150°C glass temperature, and near-complete cold cap coverage. During each test, the amounts of feed processed and glass discharged were quantified, enabling the calculation of waste processing and glass production rate for each test. A summary of the melter tests that were conducted is provided in Table 2. The tests are distinguished below as follows:

- Test 1: 8.8 hours interval processing a simulated SIXEP Magnox waste composition with 18/80 mesh size magnesium alloy. Achieved an average glass production rate of 1374 kg/m2/day at average bubbling rate of 2.2 lpm. Over 30 kg of feed was processed, resulting in the discharge of nearly 10 kg of glass. The feed rate of 3.45 kg/hr was used in most of the subsequent tests. Melter exhaust particulate sample taken for the purpose of calculating elemental mass balances for feed components across the melter.
- Test 2: 1.0 hour interval processing a simulated SIXEP Magnox waste composition with 18/80 mesh size magnesium alloy. Residual feed from Test 1, performed one week earlier, was used to demonstrate the effect of feed aging on processing properties. Achieved an average glass production rate of 1376 kg/m2/day at average bubbling rate of 0.7 lpm.
- Test 3: 1.0 hour interval processing a simulated SIXEP Magnox waste composition with 80/325 mesh size magnesium alloy. Test conducted to demonstrate the effect of fine-grained magnesium metal alloy on processing properties. Achieved an average glass production rate of 1090 kg/m2/day at average bubbling rate of 0.8 lpm.
- Test 4: 1.0 hour interval processing a simulated SIXEP Magnox waste composition with 18/80 mesh size magnesium alloy. Test conducted for comparison to Tests 2, 3, 5. Achieved an average glass production rate of 1090 kg/m2/day at average bubbling rate of 0.8 lpm.
- Test 5: 0.9 hour interval processing a simulated SIXEP Magnox waste composition with > 18 mesh size magnesium alloy. Test conducted to demonstrate the effect of coarse-grained magnesium metal alloy on processing properties. Achieved an average glass production rate of 1236 kg/m2/day at average bubbling rate of 0.6 lpm.

An objective of these tests was to demonstrate and evaluate the performance of JHCM technology for the treatment of streams with high metal contents and determine the rate at which a simulated Magnox sludge containing the magnesium metal alloy waste streams can be processed and vitrified. To this end, attempts were made to replicate the melter configuration and operating conditions used for previous tests [4-14]. These conditions include a near-complete cold cap, which is between 80-95% melt surface coverage for the DM10 since a 100% cold cap tends to lead to "bridging" in smaller melters. The bubbling rate was optimized to achieve the maximum production rate. The feed and glass compositions were processed without significant difficulties during these tests. The most notable observation during processing was the oxidation of the magnesium metal alloy on the glass surface, apparent as flashes of light. This was readily observed in all of the present tests and was not observed in previous tests with same composition with magnesium hydroxide in place of the metal alloy [2, 3]. Another observation during processing was the extensive fuming in the plenum space resulting from water, nitrogen oxides, and particulate release from the cold cap. No obvious differences were observed during tests with various magnesium metal alloy grain size or with the aging of the melter feed.

Table 2: Summary of DM10 Tests With Melter Feed Prepared With Simulated Magnox Sludge Containing Magnesium Metal Alloy

Test		1	2	3	4	**5**
Slurry Feeding Interval (hr)		8.8	1.0	1.0	1.0	0.9
Feed	Mg Alloy (Elektron) mesh size	18/80	18/80	80/325	18/80	> 18
	Feed Used (kg)	30.5	3.46	2.74	3.44	2.86
	Overall Feed Rate (kg/hr)	3.45	3.46	2.74	3.44	3.1
	Average Glass Production Rate (kg/m^2/day)*	1374	1376	1090	1368	1236
Average Bubbling Rate (lpm)		2.2	0.7	0.8	0.7	0.6
Average Temp. (°C)	Glass, 2" from floor	1136	1143	1154	1149	1124
	Glass, 4" from floor	1146	1146	1164	1157	1134
	East Electrode	1106	1088	1114	1124	1118
	West Electrode	1133	1105	1140	1151	1136
	Plenum, thermowell	585	757	724	719	699
	Plenum, exposed	595	755	722	714	695
	Film Cooler Outlet	261	260	258	260	260
Average Electrical	Voltage (V)	29.2	33.0	31.8	33.0	33.4
	Current (amps)	172	154	177	183	180
	Power (kW)	5.2	5.1	5.6	6.1	6.0
	Resistance (ohms)	0.173	0.215	0.180	0.180	0.185
Melter Exhaust Conc.	H_2O (%)	6.1	6.1	5.9	6.0	5.9
	CO (ppmv)	4.9	1.4	2.5	4.4	11.3
	CO_2 (ppmv)	767	714	757	762	803
	HF (ppmv)	5.0	8.9	9.6	11.6	13.7
	NO (ppmv)	1103	1574	1027	822	600
	NO_2 (ppmv)	625	707	740	692	826
	HNO_2 (ppmv)	9.3	19.8	12.9	10.1	6.0
	N_2O (ppmv)	4.2	5.0	2.6	1.9	2.5
	H_2 (ppmv)	68.4	< 1	< 1	< 1	< 1

* – Glass production rates calculated from feed data and target glass conversion ratio

The average feed and glass production rates for the tests are summarized in Table 2. The glass production rate obtained for the steady state test was about 1375 kg/m^2/day, which is considerably less than the 2200 kg/m^2/day that was previously achieved with the same Magnox waste feed containing magnesium hydroxide in place of the magnesium metal alloy [2, 3]. The decreased processing rate is attributable to several factors, including the decrease in feed solids content (443 g glass per liter feed vs. 800 g glass per liter feed) and the higher nitrate content of the feed in addition to the form of magnesium. The feed rate during the earlier test was only marginally higher (3.9 vs. 3.5 kg/hr), suggesting that the increased feed water content was a major factor in the decreased glass production rate. Despite glass production rates being lower than that in previous tests with the same Magnox waste feed containing magnesium hydroxide in place of the magnesium metal alloy, glass production rates obtained in the present tests were comparable to those for most Hanford HLW waste feeds [8, 11, 13, 14]. Glass production rates determined from short one-hour tests do not represent steady state. However, all but one of the rates obtained were very close to the rate from the longer steady state test.

Target processing conditions, including bubbling rate adjusted to maximize the production rate, a melt pool temperature near 1150°C, and a complete cold cap were achieved throughout the majority of the melter tests. Glass temperatures were within 20°C of the 1150°C throughout the majority of the testing. Contrary to most previously conducted tests on the DM10, glass temperatures closer to the melt pool surface typically average 10°C higher than those lower in the melt pool due perhaps to exothermic reactions occurring on the surface of the melt pool. In keeping with previous DM10 tests, the electrode temperatures were mostly lower than glass pool temperatures by as much as 70°C, depending on which electrode and the time during the test. No temperature increases in the electrodes indicative of heating from reaction associated with the decomposition of the magnesium metal alloy were observed. The plenum temperatures were about 800°C at the start of each melter run series and decreased to 500 - 600°C as the cold cap became established. During the first day of testing, this occurred after about 3 hours of feeding, while this steady state condition was not achieved during the 4.5 hours of the second testing period due to the interruptions in feeding between the tests. The average power usage for the present and previous tests processing the simulated Magnox sludge was about the same (5.2 vs. 5.4 kW); thus, the power required to evaporate the additional water in the present tests was comparable to the amount of power required for the higher rate of glass production.

The glass produced in these tests was discharged from the melter periodically using an airlift system, visually inspected for secondary phases, and sampled for total inorganic analysis. The compositions of glass samples were measured by x-ray fluorescence spectroscopy (XRF). The glass pool composition approached the target concentrations for most oxides by the end of the tests while antimony, cesium, halogens, sulfur, and rhenium were found below target for almost all glasses due to volatilization from the glass pool and cold cap. No secondary phases were observed in any of the glass samples.

4. Off-Gas Emissions

Melter emissions were monitored during each melter test for a variety of gaseous components, most notably CO, HF, and NO_x, by Fourier Transform Infra-Red Spectroscopy (FTIR) and H2 by gas chromatography. Hydrogen was detected in the melter exhaust only during the initial test and after 3 hours of feed processing. Measured hydrogen concentrations in the melter exhaust stream and measured plenum temperatures are displayed for Test 1 in Fig. 1. Notice that until the plenum temperature decreases to about 600°C, no hydrogen is detected. Once plenum temperatures reach steady state with the process (between 500 and 600°C), hydrogen concentrations varied over a wide range between 25 and 425 ppmv. Plenum temperatures were mostly greater than 700°C during Tests 2-5 and no hydrogen was detected in the melter exhaust. No hydrogen was detected in previous tests with Magnox sludge but without the magnesium metal alloy even though the plenum temperatures averaged around 550°C, indicating that the magnesium metal alloy is responsible for the hydrogen generation. The most abundant nitrogen species monitored was NO for all but Test 5. In a trend opposite to that for hydrogen, the amount of nitrogen monoxide in the exhaust decreases after three hours run time in Test 1. Nitrogen monoxide concentrations mostly ranged between 100 to 300 ppmv while the plenum temperature was above 600°C, and below 100 ppmv when the plenum temperature was below 600°C. The decrease in nitrogen monoxide concentrations was partially compensated for by increases in the nitrogen dioxide concentration. Concentrations of CO, CO_2, and NO_2, were higher and NO was lower during Test 5 than the other tests. As expected, measured concentrations of nitrogen and carbon oxides are considerably greater than those measured during previous tests with the simulated Magnox waste stream as a result of the addition of nitric acid to the feed [2, 3]. No NH_3, HCN, or HCl was detected in any of the tests.

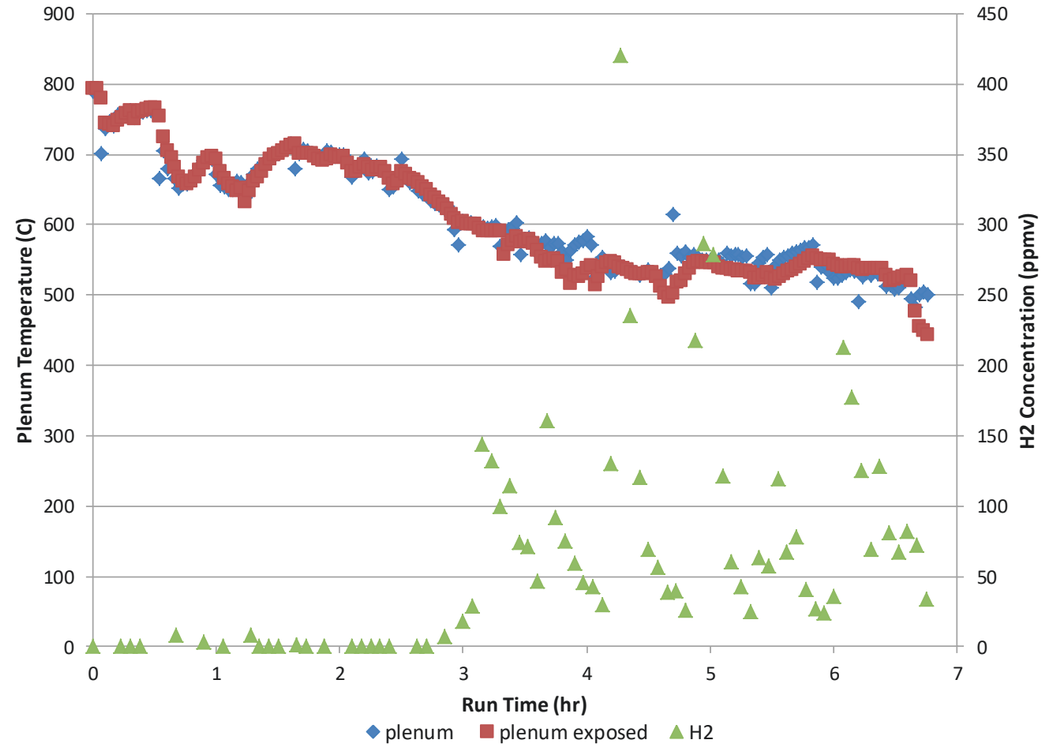

Figure 1: Plenum temperatures and hydrogen concentration measured in melter exhaust during Test 1 while processing simulated Magnox waste containing magnesium metal alloy.

The melter exhaust was sampled for metals/particles according to 40-CFR-60 Methods at steady-state operating conditions near the end of the first test; the results are presented in Table 3. Particulate emissions from the melter while feeding the Magnox sludge containing the magnesium metal alloy constituted two and a half percent of feed solids, which is over three times higher than in previous tests with magnesium hydroxide [2, 3]. Furthermore, carryover of magnesium is over twenty times greater in the present tests with magnesium metal alloy than in earlier tests with magnesium hydroxide. Almost all elements (except for rhenium and iodine, which were essentially totally lost from the glass during tests with both forms of magnesium) were carried over to the melter exhaust at much higher rates while processing the magnesium metal alloy. The higher percentage of carryover in the present tests with the magnesium metal alloy is attributable to several factors including the magnesium metal alloy itself, which is oxidized in the cold cap creating particulate that is more likely to be entrained into the exhaust stream than magnesium hydroxide. The higher feed water content and nitric acid in the feed also contribute to a more reactive environment in the cold cap as water is volatizing, carrying other feed constituents into the exhaust, and nitrate is reduced to volatile nitrogen oxides. Feed elements emitted at the lowest melter decontamination factor (DF) were iodine and rhenium, which were not retained in the glass in measurable amounts, followed by chlorine, cesium, and sulfur. Higher than typically observed carryover of non-volatile elements such as silicon, aluminum, and iron indicate physical entrainment of particulate feed components.

5. Summary and Conclusions

Thermal treatment trials were conducted with simulated Sellafield ILW feeds demonstrating the potential of thermal treatment technology for a range of wastes including Magnox sludges. Building on previous work [2, 3], the present testing demonstrated the feasibility of directly vitrifying a waste stream containing magnesium metal alloy, the generation of hydrogen associated with reaction of the metal with the alkaline waste or melter feed, the reactions of the magnesium metal alloy in the melter, the consistency of the process over a range of magnesium metal alloy grain sizes, and emissions from the melter while processing the magnesium metal alloy. Oxidation of the magnesium metal alloy on the glass surface was visually evident in these tests. However, no temperature increases in the electrodes, indicative of heating from reactions associated with the decomposition of the magnesium metal alloy, were observed. Power consumption during these tests was similar to that in previous tests without the magnesium metal alloy. Hydrogen generation increased as plenum temperatures fell into the normal operating range but remained in the few hundred ppm range. Particulate emissions from the melter while feeding the Magnox sludge containing the magnesium metal alloy were over three times higher than in previous tests with magnesium hydroxide, which is attributed to increased entrainment resulting from the more vigorous reactions in the cold cap.

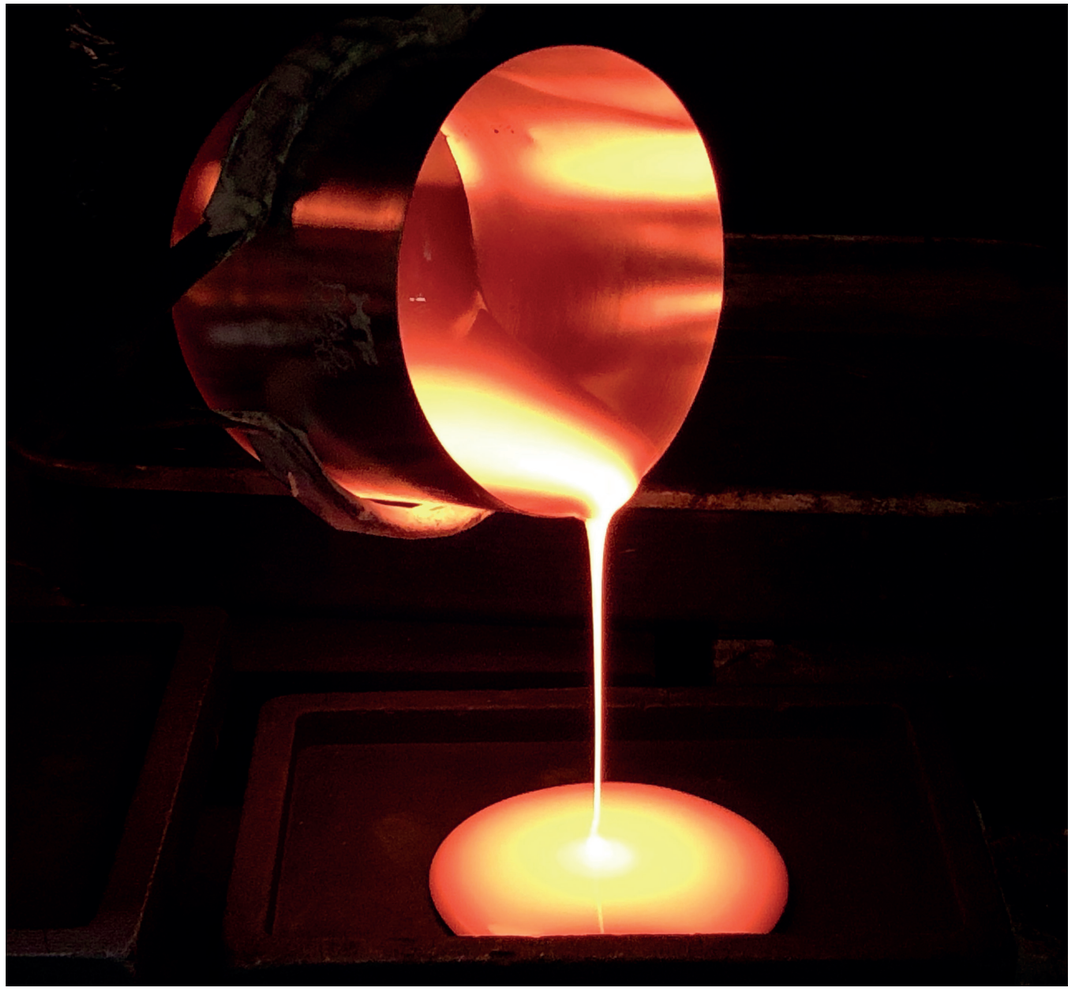

Table 3: Results From Off-Gas Sample Analysis During DM10 Tests With Melter Feed Prepared With Simulated Magnox Sludge Containing Magnesium Metal Alloy

		Mg Alloy (Elektron 18/80 mesh) 9.28% Moisture, 103% Isokinetic				Mg(OH)2 7.3% Moisture, 101% Isokinetic [3]			
		Feed (mg/min)	Output (mg/min)	% Emitted	DF	Feed (mg/min)	Output (mg/min)	% Emitted	DF
Particulate	Total	25024	620	2.48	40.4	37808	294.71	0.78	128.7
	Al	164	1.21	0.74	136	263	0.36	0.13	743.8
	B	995	30.4	3.05	32.8	1594	4.76	0.30	345.2
	Ca	160	1.22	0.76	131	257	0.94	0.37	279.6
	Ce	17.1	< 0.10	< 0.50	> 200	27	0.29	1.08	93.7
	Cl	164	123	74.7	1.34	263	NA	NC	NC
	Co	15.7	< 0.10	< 0.64	> 157	32	< 0.10	< 0.31	> 321
	Cr	68.5	3.36	4.91	20.4	110	2.61	2.38	42.2
	Cs	18.9	10.85	57.5	2	30	10.82	35.73	2.8
	Fe	61.6	0.70	1.14	88.0	99	0.26	0.27	399.4
	Hf	17.0	0.13	0.74	134	27	< 0.10	< 0.37	> 272
	I	20.0	<0.10	< 0.50	> 200	32	< 2.0	< 6.25	> 16
	K	120	14.3	11.9	8.38	192	14.94	7.78	13.0
	Mg	1942	91.4	4.71	21.2	3112	7.53	0.24	425.3
	Na	2043	87.4	4.28	23.4	3276	65.16	1.99	50.3
	Nb	14.0	< 0.10	< 0.50	> 200	22	0.13	0.59	170.1
	Nd	1012	0.23	0.02	4451	1622	3.80	0.23	443.0
	Ni	78.6	0.43	0.54	183	126	0.29	0.23	451.8
	Pb	92.9	4.24	4.56	21.9	149	3.51	2.36	42.5
	Re	15.4	11.9	77.4	1.29	25	20.63	83.57	1.2
	S	18.4	13.2	71.6	1.40	30	12.16	41.09	2.4
	Sb	16.7	0.18	1.08	92.8	27	0.27	1.01	101.3
	Si	3278	8.63	0.26	380	5254	4.98	0.10	1082.0
	Sr	16.9	0.10	0.59	168	27	< 0.10	< 0.37	> 272
	Zr	874	2.43	0.28	360	1400	1.46	0.11	1033.3
Gas	B	995	4.35	0.44	229	1594	7.45	0.46	214.3
	Cl	164	< 0.10	< 0.06	> 1641	263	NA	NC	NC
	I	20.0	15.3	76.7	1.30	32	27.95	87.02	1.2
	S	18.4	< 0.10	< 0.54	> 184	30	3.15	10.65	9.4

Acknowledgements

Many people at the Vitreous State Laboratory contributed to the success of this work and are gratefully acknowledged.

This paper was originally published as Matlack, Keith S., Kot, Wing K., Gan, Hao, Pegg, Ian L., Bowan, Bradley W. III, Smith, Eric C., Joseph, Innocent, Morgan, Sean P., & Nichol, Robert (2017). Vitrification of Sellafield Wastes with High Metallic Magnesium Alloy Content - 17495. WM2017: 43 Annual Waste Management Symposium, United States.

References

1. "Specification for the Sellafield Thermal Treatment Development Programme - Proof of Concept Phase," SP/ND-MPG/PROJ/00002, Rev C (2008).

2. K.S. MATLACK, W.K. KOT, H. GAN, I L. PEGG, G. A. DIENER and B. W. BOWAN II, "Sellafield Thermal Treatment Trials Using Advanced Joule Heated Ceramic Melter Technology" WM2010 Conference, March 7-11 2010, Phoenix, AZ

3. K.S. MATLACK, W.K. KOT, N.D. ANGELO and I.L. PEGG, "Sellafield Thermal Treatment Trials Using Advanced Joule Heated Ceramic Melter Technology," Final Report, VSL-09R1640-1, Rev. 0, Vitreous State Laboratory, The Catholic University of America, Washington, DC (2009).

4. K.S. MATLACK, M. CHAUDHURI, H. GAN, I. S. MULLER, W. GONG, and I.L. PEGG, "Glass Formulation Testing to Increase Sulfate Incorporation," Final Report, VSL-04R4960-1, Rev. 0, Vitreous State Laboratory, The Catholic University of America, Washington, DC (2005). 5. K.S. MATLACK, W. GONG, and I.L. PEGG, "Small Scale Melter Testing with LAW Simulants to Assess the Impact of Higher Temperature Melter Operations," Final Report, VSL-04R4980-1, Rev. 0, Vitreous State Laboratory, The Catholic University of America, Washington, DC (2004).

6. K.S. MATLACK, W. GONG, and I.L. PEGG, "Glass Formulation Testing to Increase Sulfate Volatilization from Melter," Final Report, VSL-04R4970-1, Rev. 0, Vitreous State Laboratory, The Catholic University of America, Washington, DC (2005).

7. K.S. MATLACK, W. GONG, I.S. MULLER, I. JOSEPH, and I.L. PEGG, "LAW Envelope C Glass Formulation Testing to Increase Waste Loading," Final Report, VSL-05R5900-1, Rev. 0, Vitreous State Laboratory, The Catholic University of America, Washington, DC (2006).

8. K.S. MATLACK, W.K. KOT, W. GONG and I.L. PEGG, "Small Scale Melter Testing of HLW Algorithm Glasses: Matrix 2 Tests," Final Report, VSL-08R1220-1, Rev. 0, Vitreous State Laboratory, The Catholic University of America, Washington, DC (2008).

9. K.S. MATLACK, S.P. MORGAN, and I.L. PEGG, "Melter Tests with LAW Envelope B Simulants to Support Enhanced Sulfate Incorporation," Final Report, VSL-00R3501-1, Rev. 0, Vitreous State Laboratory, The Catholic University of America, Washington, DC (2000).

10. K.S. MATLACK, S.P. MORGAN, and I.L. PEGG, "Melter Tests with LAW Envelope A and C Simulants to Support Enhanced Sulfate Incorporation," Final Report, VSL-01R3501-2, Rev. 0, Vitreous State Laboratory, The Catholic University of America, Washington, DC (2001).

11. K.S. MATLACK, W.K. KOT, H. GAN, and I.L. PEGG, "HLW Enhancement Tests on the DuraMelter™ 10 with Hanford AZ-102 Tank Waste Simulants," VSL-05R5260-1, Rev. 0, Vitreous State Laboratory, The Catholic University of America, Washington, DC (2005).

12. K.S. MATLACK, H. GAN, and I.L. PEGG, "Glass Formulation and DuraMelter™ 10 Testing with Simulated Idaho HLW Calcine," VSL-08S1540-1, Rev. 0, Vitreous State Laboratory, The Catholic University of America, Washington, DC (2008).

13. K.S. MATLACK, and I.L. PEGG, "Screening Tests on DuraMelter 10 with C-106/AY-102 Simulant in Support of DuraMelter 1000 Throughput Tests," VSL-00R2501-2, Rev. 0, Vitreous State Laboratory, The Catholic University of America, Washington, DC (2000).

14. K.S. MATLACK, W.K. KOT, F.P. CARDENENAS, and I.L. PEGG, "Screening Tests on DuraMelter 10 with AZ-101 Simulant in Support of DuraMelter 1000 Throughput Tests," VSL-00R2501-1, Rev. 0, Vitreous State Laboratory, The Catholic University of America, Washington, DC (2000).

15. K.S. MATLACK, and I.L. PEGG, "Advances in JHCM HLW Vitrification Technology at VSL through Scaled Melter Testing," Advances in Materials Science for Environmental and Energy Technologies II: Ceramic Transactions, Vol. 241 (eds J. Matyáš, T. Ohji, X. Liu, M. P. Paranthaman, R. Devanathan, K. Fox, M. Singh and W. Wong-Ng), (2013).

Robotics in Nuclear Gloveboxes: Reducing Operator Risks Through Deployment of Collaborative Robots

Samuel T. Stephens

MEng, CEng, MICE
Chief Engineer
Nuclear
Warrington, UK

Matt Harrison

MEng, CEng, MIStructE
Digital Developer
Engineering, Design and Project Management
London, UK

James O'Brien

MEng, CEng, MIMechE
Principal Engineer
Nuclear
Whitehaven, UK

Abstract

Around the world in chemical and nuclear industries, handling of hazardous substances by operatives are routinely completed in sealed environments referred to as "gloveboxes." Despite stringent safety measures in place, these operations present some residual risk of exposure to manual workers completing the hazardous work. A recent incident at Sellafield in February 2017 highlights this risk, which remains present until Post Operational Clean Out of the gloveboxes is complete and they are ready for dismantling.

With advances in commercial robotics, equipment has become cheaper and more functional; opportunities now exist to start to substitute non-value-adding activities currently completed by human hands with a robotic arm. In 2019, Atkins' engineers were the first to demonstrate that a commercially available collaborative robot arm could be safely deployed into an inactive glovebox and complete a range of activities to support decommissioning. To support these activities, it has been identified that a digital twin of the robotic arm will provide a useful operator aid and form the basis of a system to complete remote operations in the future.

Keywords

Digital twin; Robotics; Collaborative Robots; Nuclear; Gloveboxes

1. Introduction

1.1. Background

In nuclear, chemical, and pharmaceutical industries around the world, hazardous substances are routinely handled by site operatives, technicians, and scientists in sealed containers referred to as “gloveboxes.” Access to the sealed environment is undertaken using human arms inserted through a circular port and protected by a latex (Hypalon) glove. Configurations can vary from a simple two-port glovebox for one person to use, to a train configuration where sequences of operations along a line are completed by one or more operatives (Figure 1).

At their end of life in the nuclear industry, the gloveboxes are subjected to a process of Post-Operational Clean Out (POCO). This requires all large loose items to be removed and safely bagged for disposal as radioactive waste; small loose items are vacuumed up and fixative is applied to any residual contamination. Surveys are conducted using specialist monitors (such as an Americium Camera) and, when the insides of the glovebox are deemed safe, they are sent for dismantling.

Currently, all operations in nuclear gloveboxes are undertaken by manual workers and there remains significant radiological risks associated with manual working in gloveboxes, particularly where Alpha radiation emitters are present. An example of the risks posed occurred at the Sellafield site in February 2017, where a glove was pierced by an unidentified sharp object present and the worker was contaminated with Plutonium. This led to legal action which took place in February 2019 (ONR, 2019). A key outcome of this case is an aim by Sellafield Ltd to remove hands from gloveboxes by 2022.

Figure 1: Typical glovebox train / wall configuration (FIS360, 2018)

1.2. Deployment of Commercial Collaborative Robots

With reference to the hierarchy of hazard controls (Figure 2) advocated by the UK Health and Safety Executive (HSE, 2011), currently human hands are protected from the hazards presented by glovebox working through the use of engineering controls. Atkins’ aim is to substitute the human arm with a collaborative robot arm to elevate the risk mitigation level and increase safety to personnel.

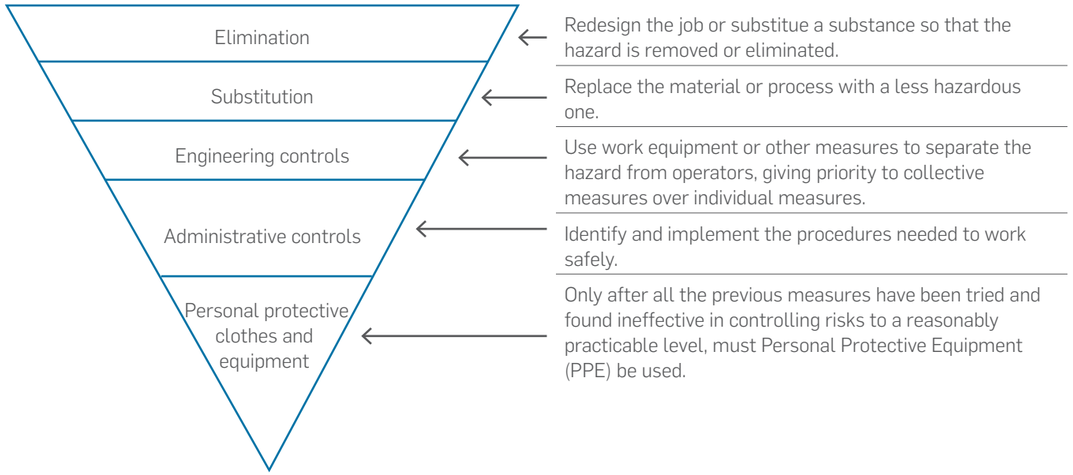

Figure 2: Hierarchy of hazard controls (adapted from HSE, 2011)

Collaborative robots (Cobots) are an emerging trend in robotics where activities currently completed by humans can be increasingly replaced and/or complemented by integration of a robotic arm solution. Cobots are designed to be safe to work alongside humans, and so incorporate safety features that allow the equipment to be used without protective guards. Typically, Cobots are designed and manufactured in accordance with ISO 13482 (ISO, 2014) that limits the maximum force and speed of operation to reduce risks to people. Most Cobots have a maximum payload of between 1kg and 10kg and may have a range of safety measures to protect people, such as torque sensors on joints, touch sensitive casings or inherently safe designs where payloads are limited to less than 1kg (Robotiq, 2020). Examples of three typical Cobot arms are shown in Figure 3.

Atkins is accelerating the risk reduction of glovebox operations in the UK nuclear industry through the development of a remote system that safely deploys a commercially available Cobot into existing gloveboxes. The aim is to substitute the physical human interaction in the glovebox with a robotic twin of the operator. By substituting hands with a remotely controlled Cobot, the ultimate aim is to enable site operators to reduce risk to manual workers and provide enhanced capabilities to increase productivity on site.

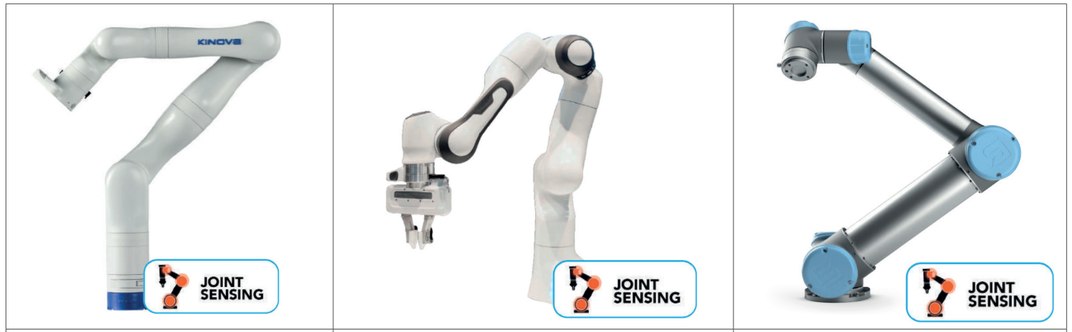

Kinova Gen 3	Franka Emika	Universal Robots UR10

Figure 3: Three typical Cobot arms (Robotiq, 2020)

2. Physical Methodology

2.1. Configuration

Operations in gloveboxes (Figure 4) are typically carried out via 6" (152mm) glove ports that have a Hypalon glove providing containment. There are two types of glove ports: the first being the "Harwell" type which has a spigot to host a double O-ring arrangement, and the second being a "CRL Push Through" glove port. Also located on gloveboxes are 8" (202mm) and 10" (254mm) ports that are commonly used for "posting" items out of the glovebox to be safely bagged for disposal.

Atkins' team identified that a solution for deployment of a Cobot into a glovebox to support POCO should not require any modification to the existing glovebox and, therefore, would need to obtain access through the existing ports. This placed an immediate physical constraint on the design by limiting the maximum joint diameter and end effector size of the Cobot. Following a review of commercially available Cobots, the Kinova Gen3 arm was selected as a candidate for experimentation. In March 2019, in collaboration with the manufacturer, Atkins conducted office demonstrations in a mocked-up glovebox of how the system may be deployed and may function.

The Kinova Gen 3 is available with six degrees (three rotational, three translation) or seven degrees of freedom (Kinova, 2019). The additional degree of freedom allows it to reach any position in an almost infinite number of ways. While initially this provided some benefit, it was later identified during testing that the redundancy afforded by the additional degree of freedom sometimes made physical manipulation more cumbersome and computationally challenging when developing a digital twin.

Figure 4: Typical glovebox configuration (FIS360, 2018)

2.2. Mobile Deployment System

Following this trial deployment, Atkins engineers developed a range of options for deployment of the Cobot into gloveboxes. Primary requirements were that the system should maintain existing containment arrangements at all times, should not impart additional load on the glovebox, and should allow an operator to control the Cobot.

Atkins has developed an integrated solution (Figure 5) with the following features:

- Three horizontal mounting positions to allow access to left- and right-hand ports at glovebox edges
- Height adjustable using winch mechanism from 600mm above floor level to up to 1875mm above floor level
- Deployable through existing glove ports of minimum inner diameter of 150mm, operable in gloveboxes of minimum depth 350mm with reach up to 1000mm and maximum payload of 3.8kg
- No load transfer between robot arm and glovebox
- Two-digit end effector to conduct a range of basic operations
- Simple and intuitive Microsoft Xbox control system
- Tablet PC mounting for up to 3 tablets

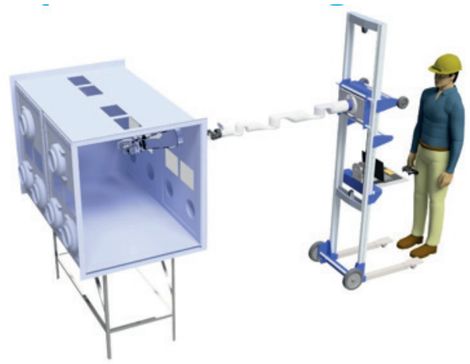

Figure 5: (a) Mobile deployment system outside of the glovebox (b) inserted in glovebox

Figure 5b: Mobile deployment system inserted in glovebox

2.3. Maintaining Containment

The system is required to maintain containment of the glovebox during insertion, operation, and removal. The options study identified a range of solutions to maintain containment. Following a critical appraisal based on a range of key factors, the selected solution adopts a similar solution to the current gloving process. This is expected to provide a level of containment that is equivalent to, or potentially exceeds, current processes.

The glove design has been developed by working with a radioactive waste bag manufacturer using PVC material and welded seams. The design incorporates reinforcement around the end effector to ensure strength at this critical location while not significantly affecting dexterity in the system. It also incorporates a clear panel to integrate with the inbuilt vision system in the Cobot arm. The design was arrived at using an applied research approach with extensive operator engagement and field testing. The glove replacement process is compatible with existing methods and procedures and enables backwards compatibility should conventional hand gloves be used for any specific operations. The approach taken allows a high degree of customisation to suit site requirements and enables rapid iteration to progressively improve the glove geometry to minimise risk of snagging or tearing. It should be noted at this stage that the glove design has not been approved for active deployment. However, the approval process is being progressed.

2.4. Testing and Deployment

The system has been subjected to a rigorous two-month development and inactive testing regime delivered by a "tiger team"' consisting of Atkins and Sellafield Ltd staff. All activities were self-funded by each party in a truly collaborative manner and the testing has proven a range of standard and repeatable POCO activities can be carried out using the Cobot including:

- General remote handling of non-fixed Items for posting out of the glovebox as part of POCO
- Remote vacuuming decontamination
- Remote contamination fixative application with spray gun
- Remote in glovebox Alpha characterisation survey

A key aim of the testing was to demonstrate the Cobot could be safely deployed, operated, and removed; significant learning has been gained from taking a real-world, applied approach (Figure 6a). The deployment process requires careful manipulation of the arm on a joint-by-joint basis during insertion to avoid collision with fixed objects inside the glovebox. The glovebox used for demonstrations was

350mm deep and considered to be the minimum depth to be encountered (Figure 6b). This provided valuable learning as it demonstrated technical feasibility, even with challenging constraints, for insertion of the standard Cobot arm. To deliver operations safely, a number of measures were put in place prior to operation:

- Existing glovebox ventilation systems remained live at all times during deployment of the Cobot
- A full view of robot operations was available to the operator through the glovebox window
- A minimum clear space of 1000mm in front of the glovebox is required to insert and withdraw the Cobot

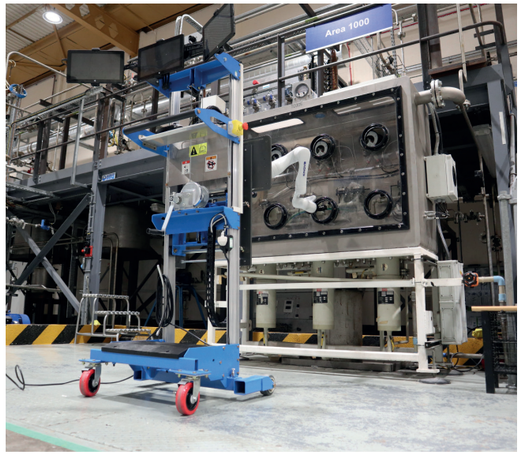

Figure 6a: Deployment system outside the glovebox in the inactive training facility

Figure 6b: Deployment system inside the glovebox in the inactive training facility

To support the design development of the operational safety case, work was completed to assess the potential for the Cobot to cause damage to the contents of the glovebox. Torque sensors at joints in the Cobot arm limit the maximum pushing force the arm can exert to 12kg. Atkins testing demonstrated that, in certain circumstances, the Cobot may lever against existing objects and exert up to 50kg of force. It was concluded that operator training is required prior to deployment of the system as an additional safety measure to prevent damage to the glovebox housing and internal items.

During the deployment of the physical system, the opportunity for further development were identified. The key operational difficulties realised were the need for training, control of the robot arm, and the vision in obscured glovebox situations. The Kinova Gen3 arm is shipped with a basic web application interface, which allows for basic control and monitoring of the arm, but the tiger team clearly identified the benefits that could be realised with a bespoke digital solution.

3. Digital Methodology

Following the completion of the physical deployment system development, Atkins' Building Design Research & Innovation team used the equipment to explore the possibilities of creating this bespoke digital-physical link. The team was tasked with investigating potential digital solutions to some of the challenges and opportunities identified during the site testing, notably the following:

- Visibility inside the glovebox. In many circumstances, viewing inside the glovebox is made challenging due to radiation induced degradation of windows.
- Joint-by-joint insertion process. Operating the arm on a joint-by-joint basis required a certain level of skill and practise and mental knowledge of the mode in which the arm operated. An operator aide to help with this process was identified as desirable.
- Potential for remote operations. Looking forward, there is a desire to conduct more operations remotely, with the Cobot operator away from the glovebox face. This will require a high level of situational awareness and a digital solution to communicate with the arm.
- Alternative means of control. Operations were conducted using the standard Xbox controller supplied with the Cobot by the manufacturer. While this provides an intuitive and easy to learn interface, development of alternative control systems could benefit specific operations.

For each of these challenges, it was identified that a common part of the solution would be the development of a live digital twin of the Cobot that could be displayed to the operator while carrying out operations. This also offered the opportunity for more ambitious development in the future to support remote operations.

3.1. Digital Twin

A digital twin is a digital representation of a physical asset. There are a variety of different levels of digital twins, varying from a simple 3D model of the asset, all the way to an autonomous physical asset being governed by a digital twin (IET, 2019).

In order to create the digital twin for the Cobot, the team used the real-time gaming engine, Unity (Unity Technologies, 2019) This software package was chosen as it facilitated easy real-time control and reaction that is often relied upon in gaming scenarios. This software also has in-built facilities to handle VR situations, something that would be employed later.

3.1.1. Forward Kinematics

The initial challenge for the development of the digital twin was to correctly calculate the position of the arm, referred to as forward kinematics, and correctly determining the position and rotation of every joint of the robot arm while solely using the rotation angles of each of the seven joints. With this information, in combination with a 3D model of the Cobot, it was possible to visualise the arm in any position. Initially, the team attempted this using a simple geometric approach as this is the clearest to understand during the development stage. However, the complexity of the situation soon became unmanageable. The team instead relied upon transformational matrices supplied by Kinova. Each joint can be progressively calculated using the product of the matrices of the lower joints.

3.1.2. Inverse Kinematics

Once the forward kinematics were modelled correctly, it was essential to accurately determine how the Cobot could reach various goals using inverse kinematics. Inverse kinematics are mathematically much more complex than forward kinematics and there are several different methods for calculating the positions. Initially, the Unity in-built kinematics solvers were employed, as they are commonly used to mimic the movement of people in real-time simulations. The methods tested here were the gradient descent and quaternion cyclic-coordinate descent (Figure 7), both of which iterate through the joints and get them to face the goal, starting from the end of the arm. These algorithms are very well suited to mimic human or animal movement where the rotations are more organic but, when applied to a robotic situation, their accuracy was not sufficient and the resulting motion was uncontrolled and jerky, which was not suitable for the precise operations inside gloveboxes.

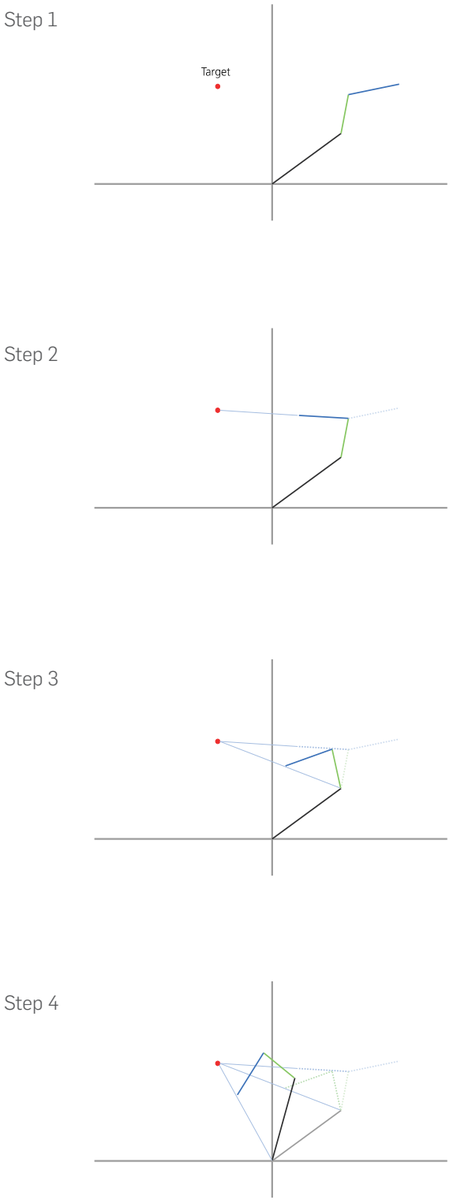

Figure 7: Cyclic coordinate descent in two dimensions

The team then attempted to utilise a mathematical solution called the Broyden-Fletcher-Goldfarb-Shanno (BFGS) algorithm. This algorithm uses a hill-climbing technique similar to the Newton method for solving nonlinear problems. Whilst this solution proves to be the most accurate, it was too slow for a real-time application. This equation took approximately 0.5 seconds to solve the rotations of the joints for a given goal, which was an order of magnitude below the target rate of 30-60 times a second to give smooth motion.

To address this issue, geometric solutions similar to that employed by the Cobot control system (Kinova, 2019) were adopted. These mathematical solutions reduced the Degrees of Freedom (DoF) from seven to six by locking one of the joints (q2' in Figure 8). This still meant the Cobot could reach any position but removed positional redundancy in favour of easy calculation.

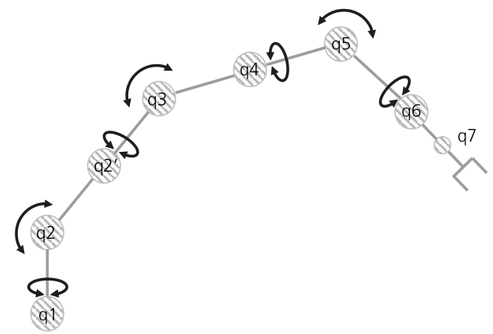

Figure 8: Joint configuration of the Kinova Gen 3 Cobot

With these two methods of determining the position now calculated, Atkins developed a digital model of the arm that can be controlled in either an individual joint control or a goal seeking control. With these two control scenarios setup, a virtual environment was created for the arm to reside in, which resembled the decommissioning facility where the physical arm could be employed (Figure 9).

With a responsive digital twin, a link between the physical and digital Cobot was created to allow for not only simulation and practise, but also live control and monitoring of the arm. This link was facilitated by the Kinova Kortex API, a programming interface for use with the arm.

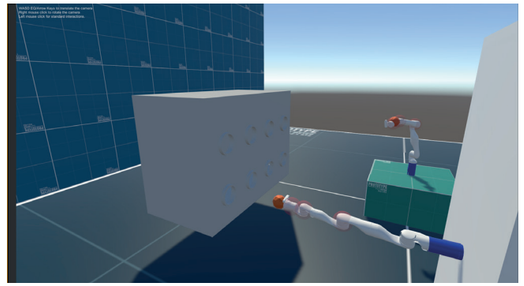

Figure 9: Virtual environment for Cobot digital twin

3.2. Training Simulator

Utilising the digital twin and the proof of concept for live control and monitoring, the team developed a training simulator, which located the digital arm adjacent to a digital glovebox and allowed for full control of the arm with controls replicating the physical arm (Figure 10). During the development of the proof of concept for this tool, three main stages and benefits were identified.

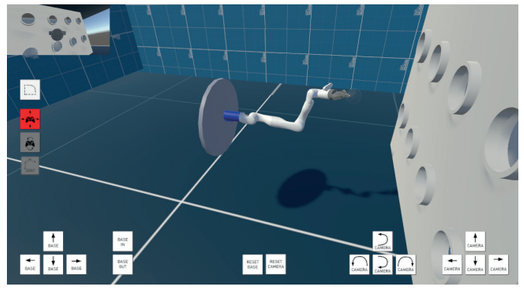

Figure 10: Training simulator developed in Unity

3.2.1. Stage 1: Training Tool for the Arm

The primary goal for the development of the proof of concept was to build a tool that could mimic the control and motion of the arm, to provide a tool that could be used to train the operatives, and attempt various different operations in a virtual environment.

3.2.2. Stage 2: Live Control and Monitoring of the Arm

Beyond the proof of concept, the next stage will be aimed to link this tool with the physical arm. The purpose of this link would be to provide a virtual 3D representation of the physical arm, which could be used to monitor the position of the arm and provide improvements in the ease-of-use of the physical arm. These features would be incredibly valuable for situations where the Cobot was being used with a darkened or misted glovebox.

3.2.3. Stage 3: Remote Control, Simulation and Recording

The third stage of development would be to produce a tool which facilitates remote operation but also recording of motion. This facility could be used to pause the control of the Cobot and attempt a procedure virtually before sending this sequence to the Cobot for execution. This feature could also facilitate a rewind feature, allowing operators to retrace their steps if they are in very confined environments.

3.3 Virtual Reality

During the first stage of development, the training simulator was also replicated in virtual reality to allow for a more immersive experience (Figure 11). This also allowed the operative to grab the arm and move the goal around in a more natural way than using the controller. This facility permitted the use of the tool to learn various operations using the arm and plan how they could be executed.

Figure 11: Virtual reality operation of the digital twin using the HTC Vive

4. Discussion

The application of the physical methodology offers outstanding opportunities to improve health and safety by eliminating the need to place humans inside dangerous environments to complete basic repetitive tasks. When combined with the digital solutions available, these opportunities increase significantly to include possible automation of tasks, improved learning, and ease of use.

There are a number of alternative Cobots available on the market. However, at present, only the Kinova arm is slender enough to fit through the small glove ports in existing gloveboxes. Other similar solutions have previously explored the option for a permanently fixed robotic arm inside a glovebox. This may be a viable solution for new-build gloveboxes, however, it is impractical for existing gloveboxes, particularly those requiring post-operational clean out. In any case, the solution developed is compatible with both new and existing gloveboxes.

The work has identified the following opportunities for further research and development:

- Refine the glove design to increase dexterity of the arm and reduce risks from snagging
- Enable remote operations away from the glovebox window via the digital twin to further improve safety
- Develop cutting tools that are compatible with the Cobot to enable waste size reduction operations inside the glovebox
- Further refine the glove design to enable tool change capability in the glovebox without removing the Cobot
- Adapt the mounting plates and glove design to accommodate the next generation of Cobots
- Integrate capability for a wider range of controls, such as the adoption of a haptic force feedback device (e.g. Haption Virtuose) or virtual reality control
- Integrate live streaming from 360°-degree cameras to enable dark operations to take place, with viewing of the footage using a virtual reality headset
- Machine learning on manually controlled processes to permit task automation for basic low-risk activities

5. Conclusions

Atkins' seeks to integrate proven and reliable solutions from other industries and use skill, expertise, and understanding of nuclear processes and procedures to integrate them in common operations across sites. Hand safety risks on nuclear sites remain a key issue, which can now begin to be addressed by the integrated solution presented.

Atkins' patent-pending solution can be retrofitted into almost any existing glovebox with limited modification and with no breach of the existing containment. Following successful initial inactive demonstrations, Atkins has developed a platform from which to embark on more complex operations and integrate additional functionality. A key part of this will be the development of digital solutions that make operation for manual workers simple and intuitive while reducing safety risks and increasing functionality.

The applied research approach taken yielded unique operator insights to inform digital solution development. Key challenges identified during trial glovebox operations led to the development of a digital twin of the arm to mimic the operation of the physical arm. This will lead to a number of further applications, the first of which being a training simulator that enables operators to practise operations without having access to physical equipment.

Acknowledgements

The authors would like to acknowledge the following individuals and organisations for their contribution to this work:

- Sellafield Ltd, for providing access to training facilities and support from operational staff as part of the "tiger team" collaborative development approach.
- Ben Logan, Chris Sanderson and Ian Pullin from the Atkins physical deployment project team, who supported the development and delivery of the solution throughout 2019.
- David Valent, who supported the development of the Cobot digital twin.
- Dr. Caroline Paradise, who provided valuable advice and sponsored the digital development as the leader of Atkins' Building Design Research and Innovation team.
- Kinova, Inc., for ongoing support throughout the project to ensure the Cobot was configured for the required use case.
- Romar Ltd, for glove manufacture and support of the containment system development.

References

FIS360 (2018) "Techniques and technologies for identifying unknown sharps in gloveboxes". June 2018, NNL & FIS360 on behalf of Sellafield Ltd, accessed 23/01/2020 https://www.gamechangers.technology/wp-content/uploads/2018/06/Glovebox-Identification-Challenge.pdf

HSE (2011) "Leadership and Worker Involvement Toolkit, Step 3, Management of Risk when planning work: the right priorities" first published June 2011, Health and Safety Executive, accessed 23/01/2020 https://www.hse.gov.uk/construction/lwit/assets/downloads/hierarchy-risk-controls.pdf

IET (2019) "Digital Twins for the Built Environment", October 2019, Institution of Engineering Technology, accessed 23/01/2020 https://www.theiet.org/media/4719/digital-twins-for-the-built-environment.pdf

ISO (2014) "ISO 13482:2014 Robots and robotic devices — Safety requirements for personal care robots", February 2014, International Organization for Standardisation, accessed 23/02/2020 https://www.iso.org/standard/53820.html

Kinova (2019) "User Guide Kinova Gen3 Ultra lightweight robot", October 2019, Kinova Inc. Accessed 23/01/2020 https://www.kinovarobotics.com/sites/default/files/UG-014_KINOVA_Gen3_Ultra_lightweight_robot_User_guide_EN_R05.pdf

Robotiq (2020) "Collaborative Robot Buyer's Guide", January 2020, Robotiq, accessed 23/01/2020 https://blog.robotiq.com/hubfs/COBOT%20EBOOK%20FINAL.pdf

ONR (2019) "Sellafield fined in case brought by ONR", 2 April 2019, Office for Nuclear Regulation, accessed 23/01/2020 http://news.onr.org.uk/2019/04/sellafield-ltd-fined-in-case-brought-by-onr/

Unity Technologies (2019) "Unity User Manual (2019.2)" Unity Technologies, accessed 23/01/2020 https://docs.unity3d.com/Manual/index.html

SNC·LAVALIN

snclavalin.com

Contact information
Akshaye Sikand
Manager, Knowledge Management
Akshaye.Sikand@snclavalin.com

5504_SL20